DETERMINATION OF AGGREGATE PHYSICAL PROPERTIES AND ITS EFFECT ON CROSS-ANISOTROPIC BEHAVIOR OF UNBOUND AGGREGATE MATERIALS

A Dissertation

by

SUNG-HEE KIM

Submitted to the Office of Graduate Studies of
Texas A&M University
in partial fulfillment of the requirements for the degree of

DOCTOR OF PHILOSOPHY

August 2004

Major Subject: Civil Engineering

DETERMINATION OF AGGREGATE PHYSICAL PROPERTIES AND ITS EFFECT ON CROSS-ANISOTROPIC BEHAVIOR OF UNBOUND AGGREGATE MATERIALS

A Dissertation

by

SUNG-HEE KIM

Submitted to Texas A&M University
in partial fulfillment of the requirements
for the degree of

DOCTOR OF PHILOSOPHY

Approved as to style and content by:

Dallas N. Little (Chair of Committee)	Robert L. Lytton (Member)
Jose M. Roesset (Member)	Eyad Masad (Member)
Christopher C. Mathewson (Member)	Paul Roschke (Head of Department)

August 2004

Major Subject: Civil Engineering

ABSTRACT

Determination of Aggregate Physical Properties and Its Effect on
Cross-Anisotropic Behavior of Unbound Aggregate Materials. (August 2004)

Sung-Hee Kim, B.S., Inha University, Korea;
M.S., Georgia Institute of Technology
Chair of Advisory Committee: Dr. Dallas N. Little

Work done by several researchers reveals that unbound aggregate materials show nonlinear cross-anisotropic behavior. The incorporation of cross-anisotropic properties significantly improves the predictions of stress distribution by reducing tensile stresses computed within granular layers. Existing pavement analysis and design approaches, however, generally assume the pavement structure to be linear isotropic layered system. This assumption is motivated by the difficulties in determining cross-anisotropic resilient material properties from laboratory experiments and lack of pavement anisotropic analysis programs.

Recently, the International Center for Aggregates Research (ICAR) developed a methodology to characterize unbound aggregate layers by considering stress-sensitivity and nonlinear cross-anisotropy. The ICAR model requires nine coefficients to account for stress-sensitivity and anisotropy of vertical, horizontal, and shear moduli. Unfortunately, ICAR testing protocol is time-consuming and expensive to perform and certainly do not lend themselves to routine testing. Since it is important to be able to consider the stress-sensitive and anisotropic nature of unbound granular materials, a simple procedure was proposed by accounting for the effects of aggregate gradation and shape properties in predicting the cross-anisotropic modular ratio of unbound granular materials. Variable confining pressure type repeated load triaxial tests were performed on six aggregate sources with three different gradations and three different moisture contents. The experimental results were analyzed within the framework of nonlinear cross-anisotropic elastic model in order to determine the model coefficients. Image analysis techniques were utilized to measure aggregate shape properties. The gradation and shape properties were fitted using a cumulative distribution function and nonlinear regression analysis, which is capable of capturing the complete distribution of these properties. The experimental and analytical results indicate that the vertical resilient modulus is greater than the horizontal resilient modulus and that aggregate physical properties significantly affect the anisotropic resilient behavior.

Based on finite element analysis, the anisotropic resilient behavior has substantial effect on the critical pavement responses. Thus, it is extremely valuable to approximate the degree of cross-anisotropy in unbound aggregates and to use it as input in the pavement analysis programs to adequately model unbound aggregate bases for pavement design and analysis.

This work is dedicated to my entire family.

ACKNOWLEDGEMENTS

I would like to express my appreciation to Dr. Dallas N. Little and Robert R. Lytton for their advice and guidance during my graduate studies at Texas A&M University. Sincere thanks and appreciation are also due Dr. Eyad Masad for his sincere advice. I would also like to thank Dr. Jose M. Roesset and Dr. Christopher C. Mathewson for serving on my committee and providing their constructive criticism and advice.

Special thanks are due Dr. Erol Tutumluer of the University of Illinois for their technical advice. This work was supported by the International Center for Aggregates Research (ICAR). This support is sincerely appreciated.

I want to express special gratitude to my parents, sisters and brothers-in-law for their unconditional love and support.

Finally, I take this opportunity to thank my wife, Hyemin Dong for her love, support, understanding and patience during this very demanding period of my life.

TABLE OF CONTENTS

TABLE OF CONTENTS (Cont'd)

TABLE OF CONTENTS (Cont'd)

CHAPTER Page

LIST OF FIGURES

FIGURE Page

LIST OF FIGURES (Cont'd)

LIST OF FIGURES (Cont'd)

FIGURE Page

LIST OF FIGURES (Cont’d)

LIST OF TABLES

TABLE Page

LIST OF TABLES (Cont'd)

TABLE Page

LIST OF TABLES (Cont'd)

TABLE Page

LIST OF TABLES (Cont'd)

TABLE Page

LIST OF TABLES (Cont’d)

LIST OF TABLES (Cont'd)

TABLE Page

LIST OF TABLES (Cont’d)

CHAPTER I

INTRODUCTION

A conventional flexible pavement is composed of a prepared subgrade, subbase, base, and a surface layer according to the American Association of State Highway Transportation Officials (1). The surface layer is usually a hot mix asphalt (HMA) and the base and subbase layers consist of unbound granular materials.

Unbound aggregate base is a primary structural layer of a pavement. The principal functions of unbound aggregate base are to diminish the load-induced stress on the subgrade to a degree that the subgrade can sustain without significant rutting and to provide adequate support for the surfacing. Although these two functions are the chief ones of interest from the structural point of view, unbound aggregate base has other important functions such as drainage and subgrade protection against frost and environmental conditions.

The State-of-the-practice pavement design guides of conventional flexible pavement containing unbound aggregate base rely on empirical approaches developed through the long-term performance observation of specific pavement structures. These structures were constructed at one general location with limited number of types of pavement material and one climatic condition. Therefore, use of empirical models should be limited to the conditions on which they are based and cannot usually account for changes in loading and environmental conditions.

This dissertation follows the journal style and format of *Transportation Research Record*, Transportation Research Board, National Research Council.

To overcome the limitations induced from the use of empirical approaches there has been a movement towards the use of mechanistic-empirical design approaches recently. The state-of-the-art in flexible pavement design approach is manifested in mechanistic-empirical design approaches and there are comprehensive well-established theories to embark on a different approach to pavement design. This is the *mechanistic design* approach that the pavement structure is modeled based on principles of engineering mechanics, mathematical system, and important engineering parameters, such as normal stresses and strains and shear stresses and strains are calculated under simulated traffic loading. These parameters are then related to performance through empirical correlations developed in practice. Thus, this approach is not entirely *mechanistic*, but *mechanistic-empirical*. The main advantage of the *mechanistic-empirical* approach is 1) the ability to predict future performance of new materials and new types of loadings, 2) better characterization of material properties and 3) capability to estimate existing pavement structural response through the experiments, nondestructive testing, and backcalculation methods.

To appropriately model the pavement structure with a mechanistic-empirical approach, an accurate material characterization technique should be developed. In recent years, several researchers began a concerted effort to develop a state-of-the-art characterization of unbound aggregate bases in pavements (1, 2, 3, 4, 5, 6). Their studies have mainly indicated that the unbound aggregate base material should be modeled as nonlinear and cross-anisotropic to account for stress sensitivity and the significant differences between vertical and horizontal moduli and Poisson's ratios. The advantage of the use of cross-anisotropy for the analysis of unbound granular bases is the drastic reduction of bottom tensile strain predicted by linear elastic analysis based on the assumptions of isotropy.

PROBLEM STATEMENT

Existing mechanistic-empirical pavement design approaches generally assume the pavement structure as a linear isotropic layered system, which means that the properties are considered to be same in all directions. Linear elastic analysis can be used with high confidence for the full depth asphalt pavement structures, but it is not proper for unsurfaced or thinly surfaced flexible pavements because the resilient properties of unbound granular materials are nonlinear and stress dependent (7, 8, 9, 10).

The most serious problem of linear isotropic analysis in thinly surfaced flexible pavements is the erroneous prediction of strong tensile stresses at the bottom of the aggregate base layer. The granular materials, however, have little to no tensile strength since the load transfer is achieved through compressive and shear stress between particles. In order to correctly characterize unbound aggregate bases it is necessary to account for the directional properties or cross-anisotropy of these layers. Only when this is done can we accurately calculate the distribution of stresses within unbound aggregate bases and properly design and analyze pavements containing unbound aggregate bases. However, cross-anisotropic models for characterizing aggregate base behaviors are usually ignored due to the difficulties in determining anisotropic material properties using conventional repeated load triaxial tests and lack of pavement anisotropic analysis programs.

Recently, International Center for Aggregates Research (ICAR) developed a methodology to characterize unbound aggregate base layers and to consider the stress-sensitivity and cross-anisotropy of these unbound aggregate layers. The ICAR model requires nine coefficients to account for the stress-sensitivity and anisotropy of vertical, horizontal, and shear moduli. Unfortunately, such repeated load resilient test is time-consuming and expensive to perform. Since it is important to be able to consider the stress-sensitive and anisotropic nature of unbound granular materials, there is a pressing need to be able to approximate these properties from routine tests.

RESEARCH OBECTIVES

The objective of this study is to develop a simplified procedure for determining the anisotropic properties of unbound aggregate layers. A major breakthrough of this research is the ability to approximate the directional properties from aggregate properties and a standard resilient modulus test (AASHTO T307-99) such as that required in the AASHTO 2002 Guide to utilize the anisotropic properties in the flexible pavement design. The predicted anisotropic properties can be used in finite element and layered elastic models to correctly estimate the pavement design life. To meet this requirement, specific objectives were formulated as follows:

(1) Develop a database of anisotropic resilient moduli of wide range of unbound aggregate bases with different moisture and compaction conditions,

(2) Investigate the effect of the aggregate physical properties such as particle shape (form, angularity, texture) and gradation on the directional properties,

(3) Develop a simple methodology to approximate the anisotropic material properties as the input values of Layered Elastic Model (LEM) or a Finite Element Model (FEM) based on aggregate physical properties,

(4) Develop performance models for fatigue cracking and rutting, and

(5) Field validation of the predictions from Finite Element Method (FEM) and Layered Elastic Model (LEM) programs

DISSERTATION ORGANIZATION

This dissertation consists of eight chapters. Chapter I is an introductory chapter. Chapter II presents the review of related background for unbound aggregate characterization. Factors affecting resilient behavior of unbound aggregate base and resilient modeling to characterize nonlinear anisotropic behavior of unbound aggregate base are described in Chapter II. Chapter III presents a simple procedure to determine the level or degree of anisotropy of unbound aggregate granular layer based on aggregate physical properties. Chapter IV includes a comprehensive laboratory test matrix and testing protocol. The laboratory test data results are presented and discussed in Chapter V. The effect of aggregate physical properties on the level of anisotropy are also discussed. Chapter VI presents the effects of aggregate physical properties on pavement performance. The transfer function based on AASHO road test data are also presented. Verifications of simple procedure to determine the level of anisotropy are presented in Chapter VII. Conclusions and recommendations are included in Chapter VIII.

CHAPTER II

BEHAVIOR OF UNBOUND AGGREGATE MATERIALS

RESILIENT BEHAVIOR OF UNBOUND AGGREGATE MATERIALS

Unbound granular layer that is composed of odd-shaped aggregate particles with different size plays a structurally important role, especially for thin asphalt pavement subjected to the medium and low volume traffic loadings by providing load distribution through consolidation, distortion and attrition (11). For a reliable unbound pavement foundation, characterization of load-deformation behavior of unbound granular material is extremely important. In 1993, the American Association of State Highway and Transportation Officials (AASHTO) proposed a new pavement design procedure using the resilient modulus concept to describe the behavior of pavement materials under surface traffic loadings.

The deformation response of granular layers due to the surface traffic loading consists of resilient and permanent deformations. In the repeated triaxial test, considerable permanent deformation is observed at the initial stage of load applications and the increment of permanent deformation becomes smaller compared to the increment of resilient deformation after few load applications as shown in Figure 2.1. Consequently, a properly designed granular layer accumulates very small amount of permanent deformation and most deformation is resilient deformation after repeated load test. For the characterization of this resilient behavior, the concept of resilient modulus (M_R) has been introduced and the resilient modulus is defined as the ratio of applied dynamic deviatoric stress to the resilient strain. The resilient modulus concept gained the recognition as a useful property describing the resilient behavior of granular materials.

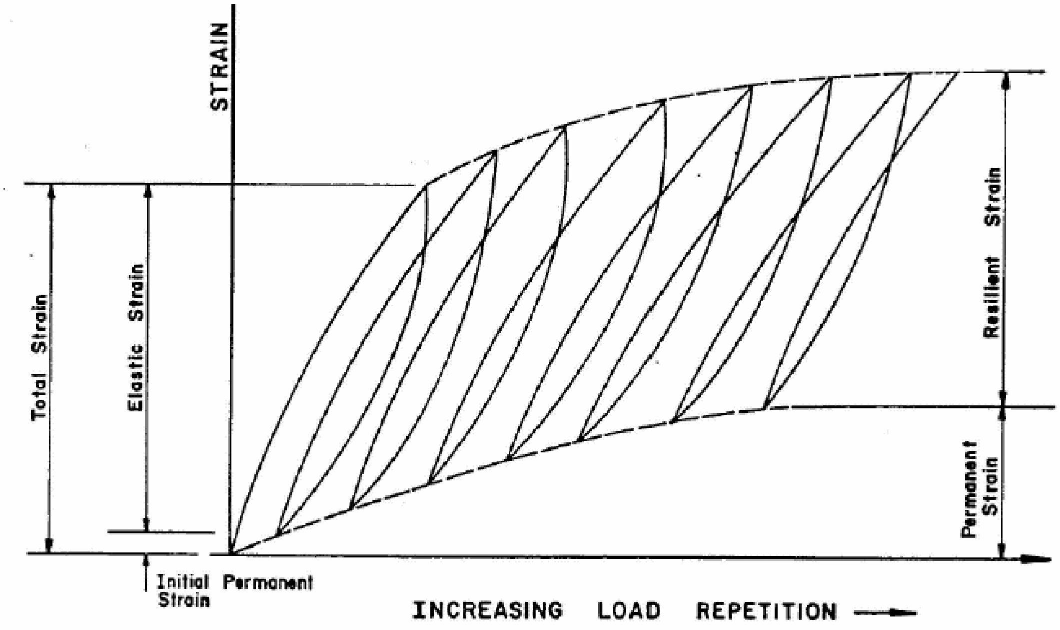

FIGURE 2.1 Strains Under Repeated Loads (12)

Poisson's ratio, which is another resilient response is stress-dependent and tied to the same material constants as the resilient modulus. A Poisson's ratio below 0.5 means that the material changes in shape and the volume decreases when a load is applied. A Poisson's ratio of 0.5 means that the material changes in shape, but not in volume in the loading conditions. A Poisson's ratio above 0.5 means that the material changes in shape and the volume also increases (dilation) when a load is applied. Although elastic isotropic materials cannot have a Poisson's ratio above 0.5, Poisson's ratios above 0.5 in unbound aggregate materials have been commonly observed from the field and laboratory test and this dilation makes the unbound aggregate stiffer and useful. Lytton (13) mentioned that beneath the tire load, an unbound aggregate generates its own lateral confining pressure and becomes very stiff almost as if it were forming a moving vertical column that travels along immediately beneath the load. This volume change (dilation) depends on the aggregate physical properties because a different amount of volume change will occur if the particle shapes are flat or elongated.

Several researchers have conducted the experiments and evaluated the nonlinear stress dependency of resilient modulus and Poisson's ratio. The following section discusses the nonlinear stress dependent model to illustrate the resilient behavior of unbound granular bases.

MODELING OF NONLINEAR RESILIENT BEHAVIOR OF GRANULAR MATERIALS

Unbound granular materials show nonlinear stress-dependent behavior and dilatancy and the efforts to characterize the nonlinear behavior of unbound granular materials in the pavement have been made in recent years. The importance of nonlinear response on critical stress and strain in pavement system is well documented in the literature (2, 12, 14, 15, 16, 17). Several nonlinear resilient models have been proposed over the years considering the significant effects of stress level on the resilient modulus.

K-Θ Model

Nonlinear resilient modulus model which is known as K-θ model as shown in Equation (2.1) was reported by Hicks and Monismith (8) and has been widely used for the pavement design purpose.

$$M_R = k_1 \theta^{k_2} \tag{2.1}$$

where, M_R = resilient modulus

θ = sum of principal stresses or first stress invariant ($\sigma_1 + 2\sigma_3$), and

k_1, k_2 = material parameters.

The resilient modulus is proportional to the first stress invariant on a log-log scale. Albeit K-θ model simply represents the nonlinear behavior of granular materials, the significant effect of shear stress on resilient modulus is ignored and thus, it is applicable only over a small range of stress paths (9).

Contour Model

Brown et al. (18) developed a model by modifying the Boyce model (19) to account for stress path effects as follows:

$$\varepsilon_v = \frac{1}{K_i}\left(\frac{I_1}{P_o}\right)^{k_1-1}\left[1-\beta\left(\frac{\sigma_d}{P_o}\right)^2\right]I_1 \tag{2.2}$$

$$\varepsilon_q = \frac{1}{3G_i}\left(\frac{I_1}{P_o}\right)^{k_2-1}\sigma_d \tag{2.3}$$

$$\Delta\varepsilon_q = \frac{1}{3G_i}\left[\left(\frac{I_{12}}{P_o}\right)^{k_2}\frac{\sigma_{d2}}{I_{12}} - \left(\frac{I_{11}}{P_o}\right)^{k_2}\frac{\sigma_{d1}}{I_{11}}\right] l^{k_3} \tag{2.4}$$

where

K_i and G_i are initial bulk and shear moduli,

$I_1 = \sigma_1 + \sigma_2 + \sigma_3$,

$\sigma_d = \sigma_1 - \sigma_3$,

p_o = reference pressure,

I_{11}, σ_{d1} and I_{12}, σ_{d2} are I_1 and σ_d at stress states 1 and 2 respectively,

$1 = (\Delta I_1^2 + \Delta\sigma_d^{\,2})^{½}$, and

β, k_1, k_2 , and k_3 are statistical material constants. Although Contour model predicts accurate resilient modulus over a wide range of stress paths, the determination of material constants, laboratory, and analytical procedures are too complicated (4).

Uzan Model

Uzan (9, 10) developed a nonlinear resilient modulus model considering the shear stress term as shown in Equation (2.5).

$$M_R = k_1 P_a \left(\frac{\theta}{P_a}\right)^{k_3}\left(\frac{\tau_{oct}}{P_a}\right)^{k_3} \tag{2.5}$$

where, M_R = resilient modulus

θ = first stress invariant (or Bulk Stress),

P_a = atmospheric pressure

τ_{oct} = octahedral shear stress, and

k_1, k_2, k_3 = material constants determined by regression analyses from laboratory test results.

Uzan model effectively explains the hardening effect due to first stress invariant term and the softening effect due to octahedral shear stress term as well as the nonlinear behavior of unbound granular layer. Due to its simplicity and the consideration of dilation effect which occurs when a pavement is subjected to a larger principal stress ratio σ_1/σ_3, Uzan model is widely used as an improved nonlinear model.

In the 2002 Guide, the simplified version of Equation (2.6) with $k_6 = 0$ and $k_7 = 1$ has been adopted to characterize the resilient modulus of unbound bases, subbases, and subgrades:

$$\boldsymbol{M_R} = \boldsymbol{k}_1 \boldsymbol{p_a} \left(\frac{\theta - 3\boldsymbol{k}_6}{\boldsymbol{p_a}} \right)^{\boldsymbol{k}_2} \left(\frac{\boldsymbol{\tau_{oct}}}{\boldsymbol{p_a}} + \boldsymbol{k}_7 \right)^{\boldsymbol{k}_3} \tag{2.6}$$

where, M_R = resilient modulus,

p_a = atmospheric pressure to normalize stresses and modulus,

θ = stress invariant, or the sum of the three principal stresses,

τ_{oct} = octahedral shear stress, and

k_1, k_2, k_3 = material parameters subject t the constraints $k_1 > 0$, $k_2 \geq 0$, $k_3 \leq 0$, $k_6 \leq 0$, and $k_7 \geq 1$

The universal model is applicable to different types of unbound paving materials ranging from very plastic clays to clean granular bases. For purely cohesive clays, the k_2 term will approach a value of 0; while for a cohesionless granular material, k_3 approaches 0. The Lytton Model (20) which determines the effective resilient modulus of unsaturated granular materials is expressed with $k6 \leq 0$ and $k7=0$.

Karasahin and Dawson Model

Karasahin and Dawson performed a repeated load triaxial test for six different aggregate sources and developed a model which accounts for the cross-anisotropic behavior of cohesionless soils as follows:

$$\nu_1 = 1 - H\left[\left(\frac{P}{P_a}\right)^L \left(\frac{q_m}{P_a}\right)^M \left(\frac{p_a}{P_m}\right)^N\right] \tag{2.7}$$

$$\nu_2 = R\left[\left(\frac{P}{P_a}\right)^S \left(\frac{q_m}{P_a}\right)^T \left(\frac{p_a}{P_m}\right)^U\right] \tag{2.8}$$

$$M_R = A\left[\left(\frac{P_m}{P_a}\right)^B \left(\frac{p_a}{P}\right)^C\right] \tag{2.9}$$

where,

ν_1: in-plane Poisson's ratio that shows the effect of horizontal strain on the orthogonal horizontal strain,

ν_2: out-of-plane Poisson's ratio that shows the effect of horizontal strain on vertical strain,

M_R: resilient modulus

$P=P_2-P_1$,

$P_m = (P_2 - P_1)/2$,

$q_m = (q_1 - q_2)/2$,

P_a = atmospheric pressure, and

A,B,C,H,L,M,N,R,S,T,U = model constants.

Karasahin and Dawson model can predict resilient response in both vertical and horizontal directions. However, only one stress- dependent resilient modulus instead of two moduli for vertical and horizontal directions can be obtained although vertical and horizontal Poisson's ratios are obtained.

FACTORS AFFECTING RESILIENT BEHAVIOR OF GRANULAR MATERIALS

Over four decades, many researchers who have investigated the resilient behavior of granular materials placed a relatively high degree of importance on the effect of degree of saturation, dry density, aggregate gradation and shape, fines content, and stress state, etc. For design purposes, it is extremely important to consider how the resilient modulus changes when the influencing factors vary in certain amounts. In this section, those factors affecting resilient behavior of unbound aggregate base are illustrated.

Effect of Degree of Saturation

It is generally agreed that the degree of saturation or moisture content greatly affects the resilient modulus of unbound aggregate base (8, 21, 22, 23). Dawson et al. (24) studied the behavior of granular materials with high degree of saturation and found that the resilient modulus of granular materials decreases with approaching complete saturation level. Over the optimum moisture content, the stiffness decreases rapidly with growing saturation level due to the development of excess pore pressure.

Several researchers demonstrated that the effect of degree of saturation on resilient behavior of granular materials varies with the aggregate type, gradation, stress state and fine content (21, 22, 25, 26, 27). Barksdale and Itani (21) showed that the resilient modulus of granite decreased almost 40% after soaking the sample and about 20% at 103 kPa and 690 kPa bulk stresses, respectively while resilient modulus of a river gravel has 50% and 25% reductions. Haynes and Yoder (22) observed a 50% resilient modulus reduction of gravel when the degree of saturation varied from 70 to 97%. Raad et al (26, 27) showed that the moisture content has significant effect in well graded materials with high proportion of fine because the water has better chance to be held in the pores in such gradation while the water can drain or infiltrate freely in open gradation.

Smith and Nair (23) observed that the resilient modulus of granular materials decrease with increase in moisture content and they attributed the reduction of the resilient modulus to the development of excess pore water pressure. Several researchers (28, 29) who conducted similar studies indicated that no dynamic or residual pore pressure is developed in open graded aggregates while significant dynamic pore pressure is developed in dense graded aggregates with high fine contents causing the resilient modulus reduction. The development of excess pore water pressure causes the decrease of the effective stress of granular materials and subsequently, reduction of both strength and stiffness of the materials. Thom and Brown (28), however, argued that water has the lubricating effect in the aggregate assembly and this lubricating effect increases the deformation in the aggregate assembly with lack of excess pore water pressure. Lekarp et al. (11) illustrated these observations as the decrease of the localized pore suctions with higher water content, leading to lower interparticle contact forces.

Effect of Dry Density

The increase of dry density or degree of compaction of aggregate materials makes the aggregate medium stronger and stiffer. However, there is no overall agreement as to the effect of dry density on resilient behavior of unbound granular base. Researchers indicated that the effect of dry density or degree of compaction has been considered as the significant influencing factors for the resilient behavior of unbound aggregate base, by increasing the resilient modulus with increasing dry density (8, 25, 30, 31, 32). On the other hand, Thom and Brown (28) mentioned that the dry density has relatively insignificant effect.

The effect of dry density varies with the aggregate types, fine contents and stress state (8, 21, 30). Hicks and Monismith (8) found that the dry density plays an important role for the partially crushed aggregates much more than for fully crushed aggregates. They also mentioned that the effect of the dry density decreases with increase of fine content. Barksdale and Itani (21) found that the resilient modulus increases as the dry density increases at a low mean normal stress. There was no consensus as to the effect of the dry density on Poisson's ratio. Allen and Thompson (31) indicated that the dry density has small influence on the Poisson's ratio change without any consistency while Kolisoja (32) reported that there is decrease in Poisson's ratio with increase of dry density of the granular material.

Effects of Gradation and Fine Content

A change in aggregate gradation produces a change in moisture content and dry density to form an appropriate aggregate assembly and the moisture content of unbound granular base significantly affects the resilient response. Researchers (15, 16, 17) reported that uniformly graded aggregates are stiffer than well graded aggregates. Adu-Osei (2) investigated the effect of gradation on resilient modulus and found that open-graded limestone had higher resilient modulus while no significant changes were observed for gravel.

Thom and Brown (28) reported that the resilient modulus generally decreases as the fine content increases. Hicks and Monismith (8) found that the resilient modulus decreases as fines content increases for partially crushed aggregates, but they found an opposite effect for fully crushed aggregates. Hicks (8, 30) mentioned that stiffness initially increases and decreases as fines are added to crushed aggregates. They explained that the initial increase of stiffness is due to the increase of the contacts as voids are filled with fines and the decrease of stiffness is due to the displacement among coarse particles as excess fines are added. This results in the loss of aggregate particle interlocks and load carrying ability lies only on the fines.

The dry density of optimum moisture content decreases as the fine content increases. It may be inferred that aggregate gradation and amount of fines has an indirect effect on the resilient behavior of unbound granular bases by affecting the impact of moisture and density of the system. A more direct impact of gradation on stiffness occurs due to the manner in which the fine particles fill the voids and impact the interaction among the coarser, angular particles. This can be visualized in the extreme when one compares a “floating matrix” where the coarse aggregate floats in the fines – preventing interaction – with a lack of fines where only coarse aggregate interaction provides a resistance to movement. The intermediate case is where the coarse aggregate and fine aggregate blend is appropriately balanced to provide optimum density and maximum particle interaction.

Effect of Aggregate Type and Shape

Aggregate type and shape are significant factors influencing the resilient behavior of granular materials. The rough-textured and angular aggregates provide more strong and stiffer mass by locking together while smooth-textured and rounded aggregate tends to slide.

Studies have indicated that the crushed aggregate, which has high angularity and rough texture, provides better load carrying capacity and shows higher resilient modulus than the rounded gravel (8, 21, 28, 30, 31, 32, 33). Researchers (10, 34, 35) reported that adding flaky particles results in greater particle abrasion, larger permanent strain, and lower stiffness under repeated loading.

Effect of Stress

It has been well known that the stress state is an important factor influencing resilient properties of unbound granular materials (2, 4, 5, 7, 14, 15, 16, 36, 37, 38). They have shown that the resilient modulus of unbound aggregates depends on the confining stress and sum of principal stresses. It is generally agreed that the resilient modulus increases with increasing confining stress and decreasing deviatoric stress. Yandell (39) reported that the effect of deviatoric stress on resilient modulus was negligible at higher confining pressure levels. The resilient modulus, however, increases with an increase in applied dynamic deviatoric stresses at low confining pressures and the significant effect of deviatoric stress on the resilient modulus were observed (8, 9, 30).

Allen and Thompson (31) investigated the effect of constant confining pressure (CCP) and variable confining pressure (VCP) performing laboratory triaxial tests. The pavement in the field is usually loaded by moving wheel loads and the major principal stress due to wheel load is not aligned in the vertical direction, but rotates in the direction of the applied load as load passes. This type of loading can not be ideally simulated in the laboratory by the CCP type repeated load triaxial tests. The VCP type repeated load triaxial tests offer the capability to apply a wide combination of stress paths by pulsing both cell pressure and deviatoric stress. Such stress path loading tests better simulate actual field conditions since in the pavement structure the confining stresses acting on the material are cyclic in nature. Allen and Thompson (31) compared the results from two different types of experiments and showed that the CCP tests resulted in lager lateral deformations and higher Poisson's ratio. Figure 2.2 and 2.3 show a typical result reported by Allen and Thompson. The rotation of principal stress affects the resilient modulus of anisotropic materials although it doesn't affect significantly the resilient modulus of isotropic materials.

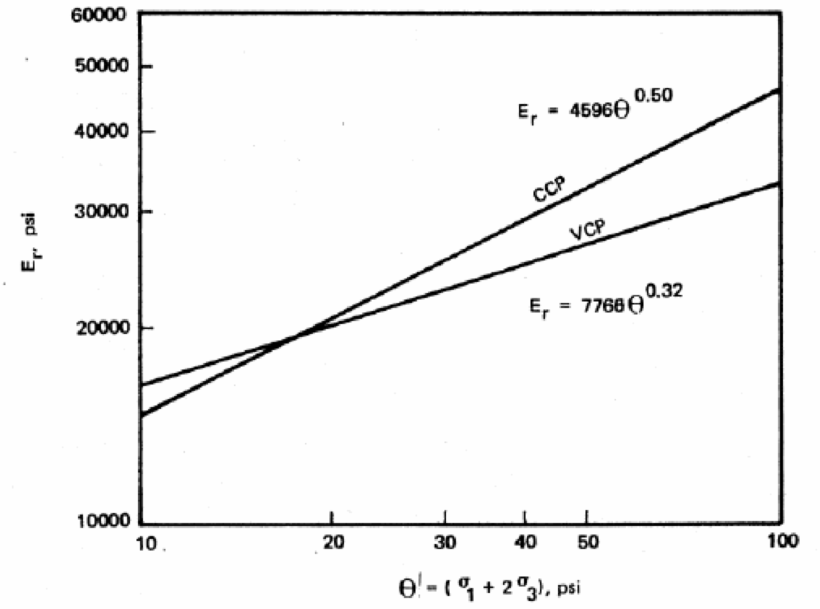

FIGURE 2.2 Comparison of Resilient Modulus with CCP and VCP (31)

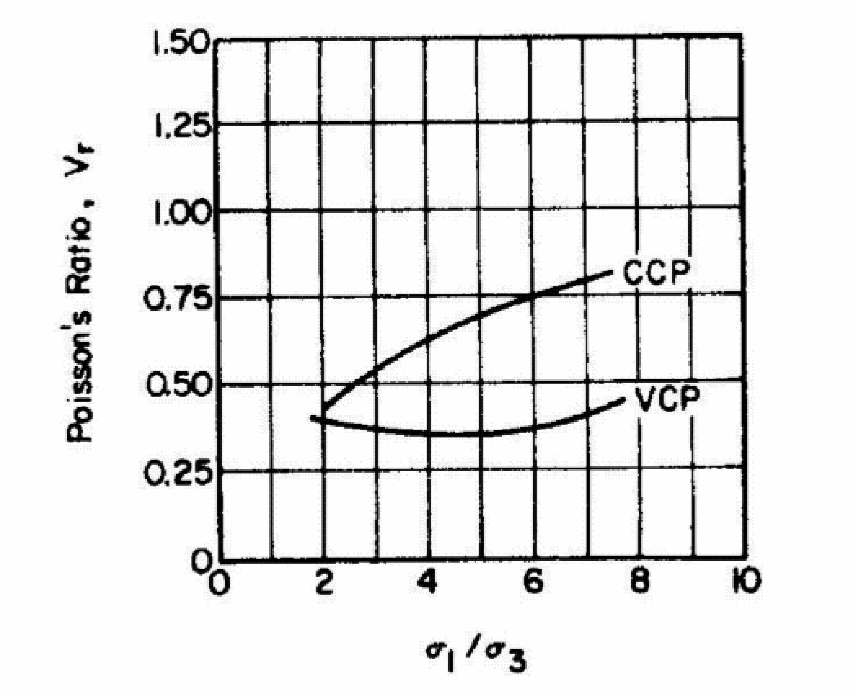

FIGURE 2.3 Comparison of Poisson's Ratio with CCP and VCP (31)

For constant confining type repeated load triaxial tests, the resilient modulus and Poisson’s ratio are defined as Equations 2.10 and 2.11 (11).

$$M_R = \frac{\Delta(\sigma_1 - \sigma_3)}{\varepsilon_1} \tag{2.10}$$

$$\nu = -\frac{\varepsilon_3}{\varepsilon_1} \tag{2.11}$$

where;

M_R = Resilient modulus,

ν = Resilient Poisson’s ratio,

σ_1 = Major principal or axial stress,

σ_3 = Minor principal or confining stress,

ε_1 = Major principal or axial resilient strain, and

ε_3 = Minor principal or radial resilient strain.

For variable confining type repeated load triaxial test, resilient modulus and Poisson's ratio are defined as (11):

$$M_R = \frac{\Delta(\sigma_1 - \sigma_3)\,\Delta(\sigma_1 + 2\sigma_3)}{\varepsilon_1\,\Delta(\sigma_1 + \sigma_3) - 2\varepsilon_3\,\Delta\sigma_3} \tag{2.12}$$

$$\nu = \frac{\Delta\sigma_1\varepsilon_3 - \Delta\sigma_1\varepsilon_1}{2\Delta\sigma_3\varepsilon_3 - \varepsilon_1\Delta(\sigma_1 + \sigma_3)} \tag{2.13}$$

ANISOTROPIC RESILIENT BEHAVIOR OF GRANULAR MATERIALS

The significant problem encountered in the pavement analysis is the observation of tensile stresses at the bottom of base layer when the linear isotropic model is used to characterize unbound aggregate behaviors. The horizontal tensile stress in the base layer can not be achieved because unbound aggregate base transfers the surface loading through compression and shear forces among the particles.

Anisotropy in unbound granular bases is inherent even before the aggregate base is subjected to traffic due to the effects of compaction and gravity (40). Particle orientation which tends to align the maximum dimension in horizontal direction occurs during aggregate material deposition (41, 42). Stresses due to construction operations and traffic are anisotropic and new particle contacts are formed due to breakage and slippage of particles, which induces further anisotropy (5). Several researchers (2, 4, 5, 6, 14, 15, 37) studied the anisotropic resilient behavior or unbound aggregate base materials and emphasized the importance of accounting not only for stress dependency but also anisotropy in order to properly model the unbound aggregate layer.

Barksdale et al. (21, 43) stated that a cross-anisotropic model of unbound granular bases is better for predicting pavement response than simplified isotropic models based on their observations from instrumented test sections. Tutumluer (4) successfully modeled the unbound granular base as nonlinear cross-anisotropic material implementing the Uzan model in the GT-PAVE finite element program. Tutumluer (4) observed that a cross-anisotropic representation of the unbound granular layers reduces the predicted tensile stresses in these layers by up to 75 percent compared to isotropic elastic analysis.

Tutumluer et al. (6) described how the horizontal resilient modulus may be only a small fraction of the vertical resilient modulus and that if this fact is not taken into account, then the resulting stress distributions in the unbound layer will be unrealistic. For example, even if stress-sensitivity is considered in an isotropic unbound aggregate layer, a strong negative tensile stress in the lower portion of the layer often results. An unbound layer cannot withstand such large tensile stresses. On the other hand, if both stress-sensitivity and anisotropy are properly considered, then the stress distributions in the unbound layer are reasonable. Moreover, a stress-sensitive and cross-anisotropic representation of the unbound aggregate base layer in a finite element model of the pavement structures led to a more accurate prediction of stresses in the pavement structure. This is particularly true for the vertical compressive stresses induced by wheel loads at the top of the subgrade, which are often used in “transfer functions” to predict pavement life due to permanent deformation (rutting) in the subgrade. Tutumluer (37) and Tutumluer et al. (6) compared computed stresses and strains to actually measured stresses and strains in instrumented pavement test sections at Georgia Tech. Their analyses showed that an isotropic, linear elastic characterization of unbound aggregate base in a finite element model of the pavement, underpredicted the vertical compressive stress imparted from the wheel load to the subgrade by approximately 100 percent and that a stress-sensitive, isotropic finite element model improved the accuracy considerably. However, a stress-sensitive and cross-anisotropic characterization of the unbound layer was necessary in order to provide the best match of calculated and measured stress and strain conditions. Tutumluer and Thompson (5) observed that using 3% to 21% of the vertical resilient modulus as the horizontal resilient modulus was required to correctly predict the horizontal and vertical strains in unbound aggregate base. A constant vertical and horizontal Poisson's ratio were assumed for this analysis. Lytton (44) proposed that a full description of the anisotropic behavior of unbound granular materials should include stress-dependent Poisson’s ratio models and that the cross-anisotropic resilient Poisson's ratios are not constant, but depend on the first and second stress invariants.

Although it has been shown that a cross-anisotropic model is superior to characterize unbound granular materials, the determination of anisotropic material properties from conventional triaxial test has been difficult. Researchers at the International Center for Aggregates Research (ICAR) and the Texas Transportation Institute (TTI) focused on determining an efficient way to characterize the stress-sensitivity and cross anisotropy of unbound aggregate bases. These important properties can be properly considered in pavement design approaches such as future upgrades to the 2002 Pavement Design Guide that may ultimately be accepted by AASHTO.

Cross-Anisotropic Characterization of Granular Materials

Cross-anisotropic representation of the unbound aggregate layer requires five different resilient properties in vertical and horizontal directions while an isotropic representation uses the same resilient properties in all directions. The constants, υ_{xx} and υ_{xy} are defined as Poisson's ratio for strain in any horizontal direction due to load applied also in the horizontal direction and Poisson's ratio for strain in the vertical direction due to the load applied in the horizontal direction, respectively. E_x and E_y, are defined as resilient moduli in the horizontal and vertical directions, respectively. G_{xy} is the shear modulus.

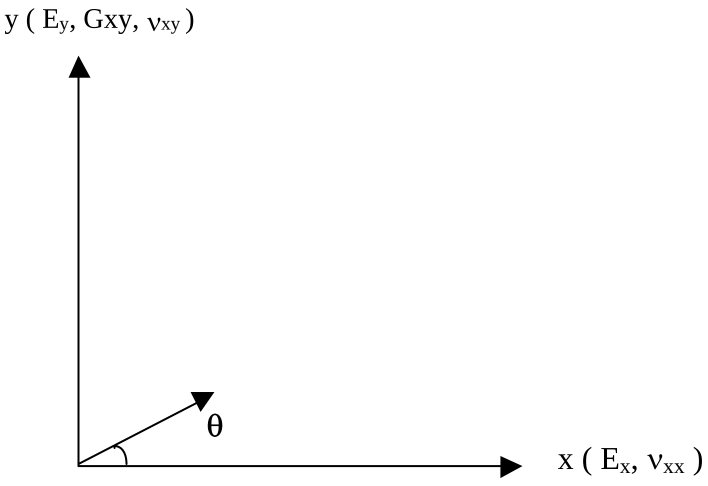

FIGURE 2.4 Cross-Anisotropic Representation

$$\begin{bmatrix} \frac{1}{E_x} & -\frac{\nu_{xy}}{E_x} & -\frac{\nu_{xx}}{E_x} & 0 \\ & \frac{1}{E_y} & -\frac{\nu_{xy}}{E_x} & 0 \\ & & \frac{1}{E_x} & 0 \\ & & & \frac{1}{G_{xy}} \end{bmatrix} \begin{Bmatrix} \sigma_x \\ \sigma_y \\ \sigma_z \\ \tau_{xy} \end{Bmatrix} = \begin{Bmatrix} \varepsilon_x \\ \varepsilon_y \\ \varepsilon_z \\ \gamma_{xy} \end{Bmatrix} \tag{2.14}$$

where:

E_y = vertical elastic modulus,

E_x = horizontal elastic modulus,

G_{xy} = shear modulus,

ν_{xy} = vertical Poisson's ratio, and

ν_{xx} = horizontal Poisson's ratio.

Elastic theory requires that the portion of the energy that is put into a material while it is being loaded be completely recovered when it is unloaded. This requirement in an orthotropic material is expressed mathematically as:

$$\oint dW = \oint \left[\frac{I_1 dI_1}{9E_y}(1+2m-4p-2q) + \frac{dJ_2^{/}}{2G_{xy}} + \frac{\tau_{zx}}{E_y}(2m+2q-s)d\tau_{zx} \right] \tag{2.15}$$

where,

W = elastic work potential of orthotropic elastic material,

I_1 = first invariant of stress tensor,

J'_2 = second invariant of deviatoric stress tensor,

E_y = elastic modulus of material in vertical direction,

G_{xy} = shear modulus between vertical and horizontal directions,

τ_{xy} = shearing stress in horizontal plane,

$m = E_y/E_x$, ratio between vertical and horizontal modulus,

p = $\nu_{xy} \bullet m$, Poisson's ratio between vertical and horizontal planes multiplied by modulus ratio,

$q = \nu_{xz} \bullet m$, Poisson's ratio in horizontal plane multiplied by modulus ratio, and

$s = E_y/G_{xy}$, ratio of vertical modulus to shear modulus.

The change of the shear stress in a horizontal plane, $d\tau_{xz}$ is zero and Equation (2.15) can also be written as (2.16):

$$\oint dW = \oint \frac{I_1 dI_1}{9E_y}\left[1 + 2m - 4p - 2q\right] + \frac{dJ_2^{/}}{2G_{xy}} = 0 \tag{2.16}$$

The work potential can thus be written as:

$$dW = \frac{dW}{dI_1} dI_1 + \frac{dW}{dJ_2^{/}} dJ_2^{/} = 0 \tag{2.17}$$

where:

$$\frac{dW}{dI_1} = \frac{I_1}{9E_y}\left[1 + 2m - 4p - 2q\right] \tag{2.18}$$

and,

$$\frac{dW}{dJ_2^{/}} = \frac{1}{2G_{xy}} \tag{2.19}$$

But,

$$\frac{d^2W}{dI_1 dJ_2^{/}} = \frac{d^2W}{dJ_2^{/} dI_1} \tag{2.20}$$

Adu-Osei et al. (14, 15) assumed that the elastic moduli in different directions obey the Uzan model and thus, can be represented as smooth functions of the stress invariants as shown in Equations 2.21, 2.22, and 2.23.

$$E_y = k_1 (I_1)^{k_2} \left(J_2^{'} \right)^{k_3} \tag{2.21}$$

$$E_x = k_4 (I_1)^{k_5} \left(J_2^{'} \right)^{k_6} \tag{2.22}$$

$$G_{xy} = k_7 (I_1)^{k_8} \left(J_2^{'} \right)^{k_9} \tag{2.23}$$

where:

I_1 = first stress invariant (bulk stress),

τ_{oct} = second deviatoric stress invariant,

P_a = atmospheric pressure, and

k_i = material coefficients.

Equations 2.20, 2.21, 2.22 and 2.23 can be combined to generate a partial differential equation for the vertical and horizontal Poisson's ratios as (44):

$$2\frac{\partial \nu_{xy}}{\partial J_2^{/}} - \frac{k_6}{I_1 J_2^{/}} \nu_{xy} = -\frac{\Phi_1(I_1, J_2^{/})}{2I_1} \tag{2.24}$$

$$2\frac{\partial \nu_{xx}}{\partial J_2^{/}} - \frac{k_6}{I_1 J_2^{/}} \nu_{xx} = -\frac{\Phi_2(I_1, J_2^{/})}{2I_1} \tag{2.25}$$

where:

$\Phi_i(I_1, J_2^{/})$ = functions of I_1, $J_2^{/}$ and the k-values from k_2 through k_9

Since the shear stress and strain can not be measured in triaxial test, only 2 equations from Equation (2.14) can be used to solve for 4 of 5 material properties of a cross-anisotropic elastic material.

$$\begin{bmatrix} \dfrac{1}{E_x} & -\dfrac{\nu_{xy}}{E_x} & -\dfrac{\nu_{xx}}{E_x} \\ -\dfrac{\nu_{xy}}{E_x} & \dfrac{1}{E_y} & -\dfrac{\nu_{xy}}{E_x} \end{bmatrix} \begin{Bmatrix} \sigma_x \\ \sigma_y \\ \sigma_x \end{Bmatrix} = \begin{Bmatrix} \varepsilon_x \\ \\ \varepsilon_y \end{Bmatrix} \tag{2.26}$$

To numerically solve the anisotropic material properties, ICAR developed a method to fully characterize the required gamut of stress-sensitive and cross-anisotropic properties of the unbound aggregate base. The laboratory testing protocol is efficient and material properties from the testing protocol conform the elastic theory. More detail information on the ICAR testing protocol will be found in elsewhere (2, 14, 15).

Determination of Anisotropic Resilient Moduli

Adu-Osei (2) used the System Identification (SID) method (45) to backcalculate anisotropic resilient properties from the results of repeated triaxial tests. The SID estimates the system characteristics using only input and output data from the system to be identified (45). The error between the model and the real process will be minimized to a certain predefined level. Figure 2.5 is a schematic diagram of the SID procedure. The model response, Y_k, is compared to the actual response of the system, Y, and the error, e, between the two is used to adjust the parameters of the model by means of an algorithm, which optimizes some prescribed criterion.

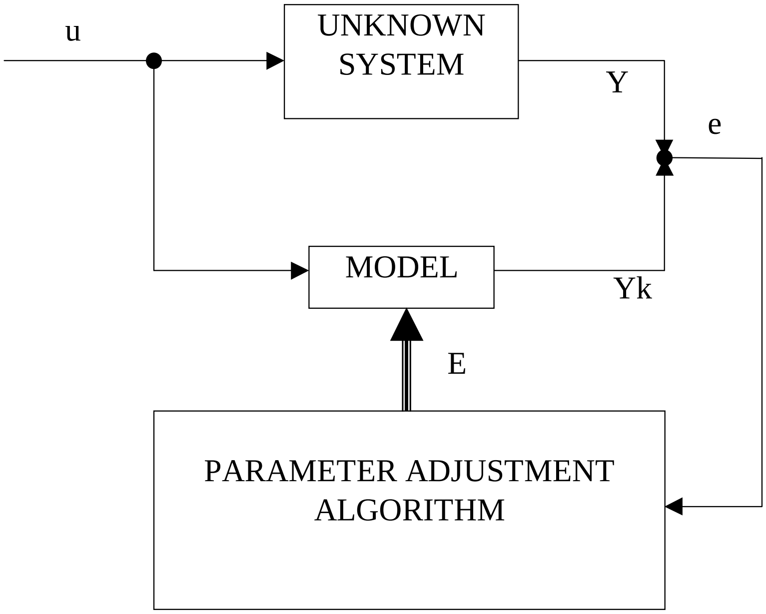

FIGURE 2.5 System Identification Scheme (45)

The accurately measured output data from unknown system and constitutive model to represent the system behavior as well as a parameter adjustment algorithm are required in SID. To adjust the model parameters, an algorithm based on Taylor's series expansion were used and following relation was developed.

$$r = F\alpha \tag{2.27}$$

The vector, r is determined from the outputs of the model and the real system. The sensitive matrix, F, is generated by the differentials of the output with respect to the parameter and the vector *r* is obtained from the output of the model (45). Adu-Osei (2) accommodated the SID method to back-calculate the five different anisotropic properties and defined Equations 2.27 as follows:

$$F = \begin{bmatrix} \dfrac{\partial(\Delta\varepsilon_x)}{\partial E_x} \cdot \dfrac{E_x}{\Delta\varepsilon_x^{\wedge}} & \dfrac{\partial(\Delta\varepsilon_x)}{\partial \nu_{xy}} \cdot \dfrac{\nu_{xy}}{\Delta\varepsilon_x^{\wedge}} & \dfrac{\partial(\Delta\varepsilon_x)}{\partial \nu_{xx}} \cdot \dfrac{\nu_{xx}}{\Delta\varepsilon_x^{\wedge}} & \dfrac{\partial(\Delta\varepsilon_x)}{\partial E_y} \cdot \dfrac{E_y}{\Delta\varepsilon_x^{\wedge}} \\ \dfrac{\partial(\Delta\varepsilon_y)}{\partial E_x} \cdot \dfrac{E_x}{\Delta\varepsilon_y^{\wedge}} & \dfrac{\partial(\Delta\varepsilon_y)}{\partial \nu_{xy}} \cdot \dfrac{\nu_{xy}}{\Delta\varepsilon_y^{\wedge}} & \dfrac{\partial(\Delta\varepsilon_y)}{\partial \nu_{xx}} \cdot \dfrac{\nu_{xx}}{\Delta\varepsilon_y^{\wedge}} & \dfrac{\partial(\Delta\varepsilon_y)}{\partial E_y} \cdot \dfrac{E_y}{\Delta\varepsilon_y^{\wedge}} \end{bmatrix} \tag{2.28}$$

$$\alpha = \begin{bmatrix} \dfrac{E_x^{r+1}}{E_x^r} & \dfrac{\nu_{xy}^{r+1}}{\nu_{xy}^r} & \dfrac{\nu_{xx}^{r+1}}{\nu_{xx}^r} & \dfrac{E_y^{r+1}}{E_y^r} \end{bmatrix}^T \tag{2.29}$$

$$r = \begin{Bmatrix} \dfrac{\Delta\varepsilon_x^m - \Delta\varepsilon_x^{\wedge}}{\Delta\varepsilon_x^{\wedge}} \\ \dfrac{\Delta\varepsilon_y^m - \Delta\varepsilon_y^{\wedge}}{\Delta\varepsilon_y^{\wedge}} \end{Bmatrix} \tag{2.30}$$

where:

$$\frac{\partial\Delta\varepsilon_x}{\partial E_x} = -\frac{1}{E_x^2}\left[(1-\nu_{xx})\Delta\sigma_x - \nu_{xy}\Delta\sigma_y\right],$$

$$\frac{\partial\Delta\varepsilon_x}{\partial \nu_{xy}} = -\frac{1}{E_x}\Delta\sigma_y\,,$$

$$\frac{\partial\Delta\varepsilon_x}{\partial \nu_{xx}} = -\frac{1}{E_x}\Delta\sigma_x\,,$$

$$\frac{\partial\Delta\varepsilon_x}{\partial E_y} = 0\,,$$

$$\frac{\partial\Delta\varepsilon_y}{\partial E_x} = \frac{2\nu_{xy}}{E_x^2}\Delta\sigma_x\,,$$

$$\frac{\partial\Delta\varepsilon_y}{\partial E_x} = -\frac{2}{E_x}\Delta\sigma_x\,,$$

$$\frac{\partial\Delta\varepsilon_y}{\partial \nu_{xx}} = 0\,,$$

$$\frac{\partial \Delta\varepsilon_y}{\partial E_y} = -\frac{1}{E_y^2}\Delta\sigma_y \,,$$

$\Delta\varepsilon_x{}^m$ = measured (actual system) radial strain,

$\Delta\varepsilon_y{}^m$ = measured (actual system) axial strain,

$\Delta\varepsilon_x{}^\wedge$ = calculated (model) radial strain, and

$\Delta\varepsilon_y{}^\wedge$ = calculated (model) axial strain.

Once the vector a is obtained, a new set of parameters is determined:

$$E_x^{r+1} = E_x^r(1+\beta) \qquad (2.31)$$

where r is the iteration number.

The iteration process is terminated when the desired convergence is achieved. The adjustment vector, β works as a relaxation factor for smooth convergence and was assumed as 0.6.

Consideration of Anisotropic Modeling on Pavement Analysis

Existing mechanistic-empirical pavement design approaches assume the pavement structure as a linear isotropic layered system, which means that resilient properties of unbound aggregate base is considered to be the same in all directions. Linear elastic analysis can be used with high confidence for the full depth asphalt pavement structures, but it is not proper for the unsurfaced or thinly surfaced flexible pavements because the resilient properties of unbound granular materials are nonlinear and stress dependent (8, 9, 10, 18, 30, 33).

Several researchers (2, 4, 5, 6, 14, 15, 38) have found that nonlinear cross-anisotropic modeling for unbound aggregate base reduced the significant tensile stress at the bottom of base layer, which is normally observed when linear isotropic model is used. They also revealed that the critical pavement responses such as tensile strain at the bottom of asphalt concrete layer (AC) and compressive strain at the top of subgrade predicted by nonlinear cross-anisotropic finite element program are higher than those predicted by linear or nonlinear isotropic models. Especially, the vertical strain at the top of subgrade, which is direct input for base rutting calculation, is higher because of the reduced horizontal stiffness of granular base.

Since the pavement critical responses are inputs of transfer functions which estimate the pavement thickness and design life, predicted higher critical responses directly affect the pavement layer thickness. Tutumluer and Thompson (5) investigated the effects of varying anisotropic modular ratio on the critical pavement responses; surface deflection, strains for AC and subgrade, deviatoric stress at the subgrade layer. They showed that the vertical subgrade deviator stress is mainly influenced by the variations of horizontal modular ratio. Since the tendency to spread in horizontal direction increases when horizontal modulus decreases, it is feasible for vertical strain or stress at the top of subgrade to be higher when some percentages of vertical modulus are taken into account as the horizontal modulus. Tutumluer and Thompson (5) also have observed that increasing both horizontal and shear modular ratio decreases the horizontal tensile strains in the HMA layer.

Australian mechanistic pavement design guide, AUSTROAD and Airport Pavement Structural Design System, APSDS already employed an cross-anisotropic model for unbound granular base layer by using the linear cross-anisotropic program, CIRCLY. Some researchers studied the effects of various degrees of anisotropy on the flexible pavement behavior using CIRCLY program and showed that horizontal strain at the bottom of HMA and vertical strain at the top of subgrade are always increased when cross-anisotropy is taken into account as shown in Figure 2.6 and 2.7.

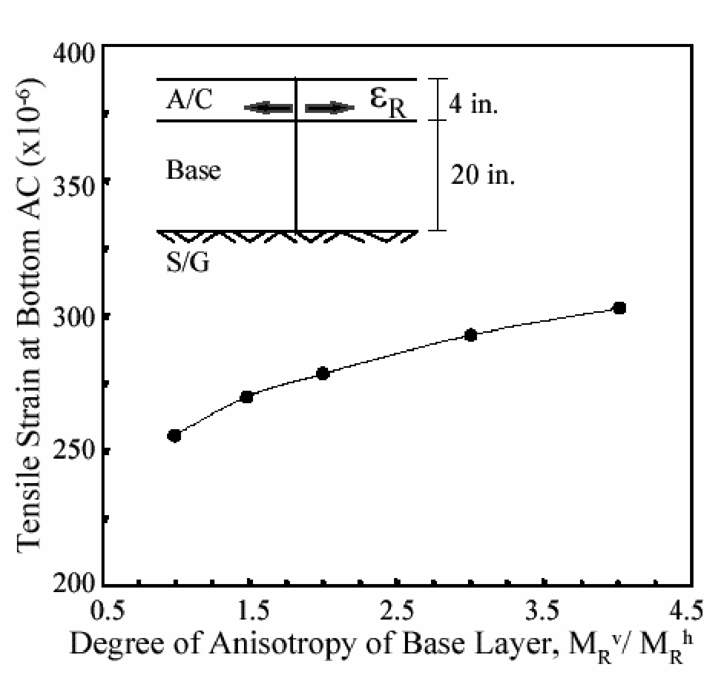

FIGURE 2.6. Effect of Cross-Anisotropy on Tensile Strain at the Bottom of HMA Layer (46)

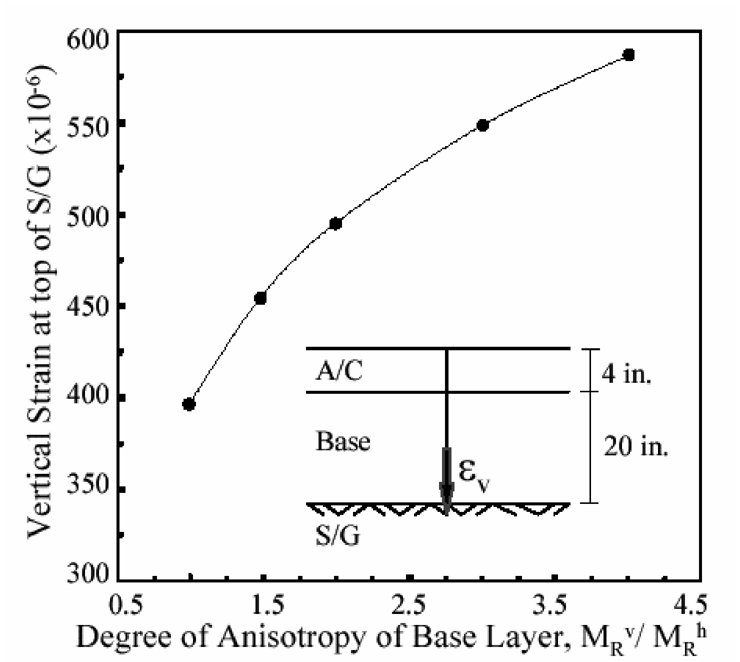

FIGURE 2.7. Effect of Cross-Anisotropy on Vertical Strain at the Top of Subgrade Layer (46)

PERMANENT DEFORMATION IN UNBOUND GRANULAR MATERIALS

Permanent deformation is one of the most significant load-induced distresses in flexible pavement. Excess rutting causes asphalt surface cracking around the rutting and it gives a chance for water to penetrate into the unbound aggregate base under repeated surface loadings. The penetration of excess water makes unbound granular base to be susceptible for rutting and accelerates the rutting within base layer. Although the rutting occurred within unbound granular base is serious it has been assumed that no rutting occurs above the subgrade. The efforts to account for the rutting for unbound granular base has been performed and the prediction models for permanent deformation of unbound aggregate base have been developed. Several prediction models of permanent deformation are reviewed.

VESYS Model

The VESYS model assumes that the permanent strain is proportional to the resilient strain.

$$\varepsilon_p(N) = \varepsilon\mu N^{-\alpha} \tag{2.32}$$

where

$\varepsilon_p(N)$ = permanent or plastic strain due to single load or Nth application,

ε = the elastic/resilient strain at the 200th repetition,

N = the number of load application,

μ = Parameter representing the constant of proportionality between permanent and elastic strain, and

α = Parameter indicating the rate of decrease in permanent strain with number of load applications.

Ohio State Model

Ohio State University (OSU) proposed permanent deformation prediction model. The OSU model has the relationship between the accumulated permanent strain (εp) and number of repeated load (N) as follows:

$$\varepsilon_P / N = AN^m \tag{2.33}$$

where,

εp = plastic strain at N number of load repetitions

N = number of repeated load applications

A = experimental constant dependent on material and state of stress conditions

m = experimental constant depending on material type

Michigan State Model

Michigan state model assumes the straight line can be developed between permanent strain and logarithm of number of load cycles as follows.

$$\varepsilon_p = a + b\ln(N) \tag{2.34}$$

where,

ε_p = Accumulated permanent strain

N = Number of load repetitions

a, b = Regression constants

Tseng and Lytton Model

Tseng and Lytton (47) developed a model to characterize the permanent deformation. The stress-strain response is modeled by three parameters ε_0, β, and ρ. The basic relationship is:

$$\varepsilon_a = \varepsilon_0 \times EXP\{-(\rho / N\}^{\beta} \tag{2.35}$$

where,

ε_a = permanent axial strain

N = number of load repetitions

ε_0, β, and ρ = material parameters

Rutting Rate (RR) Model

Thompson and Naumann (48) developed RR model and validated the RR model through the analyses of AASHTO Road test data. The RR model uses the ratio of repeated deviator stress to unconfined compressive stress as an indicator for rutting. Thompson (49) reported that stress ratio is important indicator for rutting potential and thus, the factors influencing the stress state and strength of the in-situ granular materials should be taken into account.

$$RR = RD / N = A / N^{B} \tag{2.36}$$

where,

RR = Rutting Rate

RD = rut depth, inches

N = number of repeated load applications

A, B = terms developed from field calibration testing data and information

CHAPTER III

DETERMINATION OF ANISOTROPIC RESILIENT RESPONSES OF UNBOUND GRANULAR LAYER

MECHANISTIC-EMPIRICAL DESIGN PROCEDURE

The State-of-the-practice design guides rely on empirical approaches developed through the long-term performance observation of specific pavement structures, which were constructed at one general location with limited number of types of pavement material and one climatic condition. Since these pavement performance observations are based on the conditions on which they are based, it is problematic when the empirical design approach is used at the traffic load levels and in environmental conditions well beyond their observational base. To correct the problems induced from the use of empirical approaches, there has been a movement towards the use of mechanistic-empirical design approach recently and there are comprehensive well-established theories to embark on a different approach to pavement design.

The first mechanistic design curves for flexible pavements, based on elastic layered theory, were developed in the early 1960s. Due to the lack of computational resources, each design curve had to be laboriously calculated by hand and thus, they could only be developed for a limited range of idealized pavement systems. The advent of innovative computational resources made it possible to calculate the load-induced pavement responses in multi-layered pavement systems. This has made it much more feasible to employ mechanistic analysis procedures in pavement design. Since 1986, the AASHTO Joint Task Force on Pavements (JTFP) has supported and prompted the development of Mechanistic-Empirical procedures for pavement thickness design. The National Cooperative Highway Research Project (NCHRP) 1-26 (1990 and 1992) was the first sponsored research project for developing mechanistic empirical pavement design procedures. NCHRP 1-26 researchers proposed working versions of mechanistic empirical design processes and procedures that relate pavement response variables, such as stresses, strains and deflections (σ, ε, Δ) due to the surface wheel loads. Since 1997, NCHRP 1-37 (Development of the 2002 Guide for the Design of New and Rehabilitated Pavement Structures) was initiated with the objective of developing mechanistic pavement analysis and design procedures suitable for use in future versions of the AASHTO guide. The general concepts of a mechanistic-empirical design procedure are illustrated in Figure 3.1.

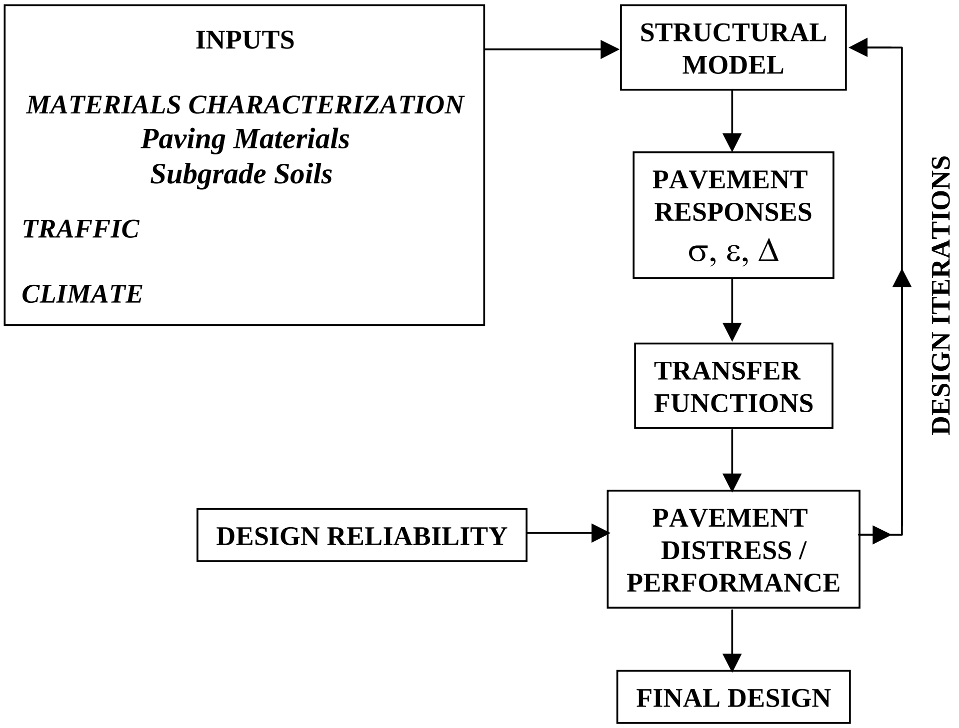

FIGURE 3.1 Components of Mechanistic-Empirical Pavement Design (1)

The two major components are: (1) a pavement structural model to calculate as accurately as possible the critical pavement responses (σ, ε, Δ) and (2) transfer functions to translate those responses into measures of pavement performance. The design process entails iteratively adjusting the pavement structure until the desired level of performance and reliability are achieved.

A prerequisite for the successful mechanistic pavement design approach is that the material behavior is properly understood. The pavement materials are characterized by strength and resilient properties that can be obtained directly from laboratory tests or backcalculated from nondestructive tests conducted in situ. Since unbound granular layer is composed of numerous numbers of individual aggregate particles with different shape and size, and experiences the change of moisture conditions due to rainfall, drainage, and evaporation under repeated traffic loadings. It is obvious that the physical characteristics of individual aggregates as well as moisture contents and dry density affect on the resilient properties of unbound granular bases. It is significant to take into account how the resilient behavior is affected with the change in different influencing factors for the design purpose. The pavement design approach, which takes into account these various environmental conditions as well as aggregate physical characteristics is important for the pavement performance and service life.

Aggregate gradation and shape properties have significant influence on the mechanical response of unbound base layers. In this study, these properties are related to the elastic moduli in Equations 2.21, 2.22, and 2.23 by means of k-coefficients. K-values obtained by the laboratory testing can be used to predict the vertical, horizontal, and shear moduli as they vary with stress state. Knowing how k-values depend on aggregate physical characteristics allows simple tests to be run and the results to be fed directly into a finite element computer program or a layered elastic program that can predict how that base layer will respond to the surface traffic loadings. This simple prediction makes it possible to determine specification limits on k-values and to relate those limits back to the needed size, gradation, shape specifications of the base course.

Ultimately, the influence of the physical properties, and consequently, the cross-anisotropic moduli on pavement response is investigated using mechanistic computer model and the calculated pavement critical responses are used in order to estimating the pavement design life. Thus, it is extremely valuable to approximate the degree of cross-anisotropy in unbound aggregates in order to adequately model unbound aggregate bases for pavement design and analysis.

CHARACTERIZATION OF AGGREGATE SHAPE

Aggregate particle shape can be expressed using three independent properties: form, angularity, and surface texture (50, 51, 52, 53). Form quantifies the dimensional proportions of the aggregate. Angularity refers to the sharpness or roundness of the corners, while texture refers to the small-scale asperities. Figure 3.2 shows a two-dimensional schematic of these three properties. Within a specific type of aggregate (mineralogy and classification), shape characteristics significantly influence the resilient response of the granular material. Rough-textured and angular aggregates develop a stronger and stiffer mass by locking together while smooth-textured and rounded aggregate particles tend to slide past one another.

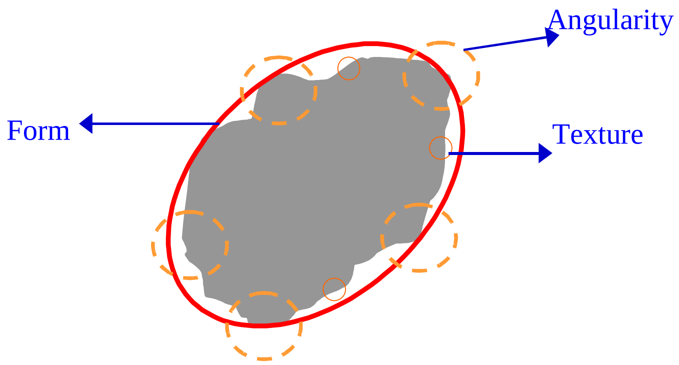

FIGURE 3.2 Schematic Diagram of Aggregate Shape Properties (53)

Studies have proven that the intuitive and obvious is true: crushed aggregates, high in angularity and roughly textured, provide better load carrying capacity and a higher resilient modulus than rounded, uncrushed particles (11, 30, 34, 35, 50, 51, 52, 53). The aggregate shape characteristics were measured from two-dimensional projections of aggregates using the Aggregate Imaging System (AIMS) (53). This is a computer-controlled system that captures images of particles placed on a lighting table. The system adjusts the image resolution as a function of particle size in order to capture the details of particle form, angularity, and texture. Figure 3.3 illustrates the image analysis system. Aggregates were placed under an optical microscope equipped with a digital camera, which is capable of capturing gray-scale images of 256 intensities. The captured images are converted to black and white. The particle size used to capture the form and angularity was 4.75 mm in diameters and 50 aggregate particles were used for each analysis.

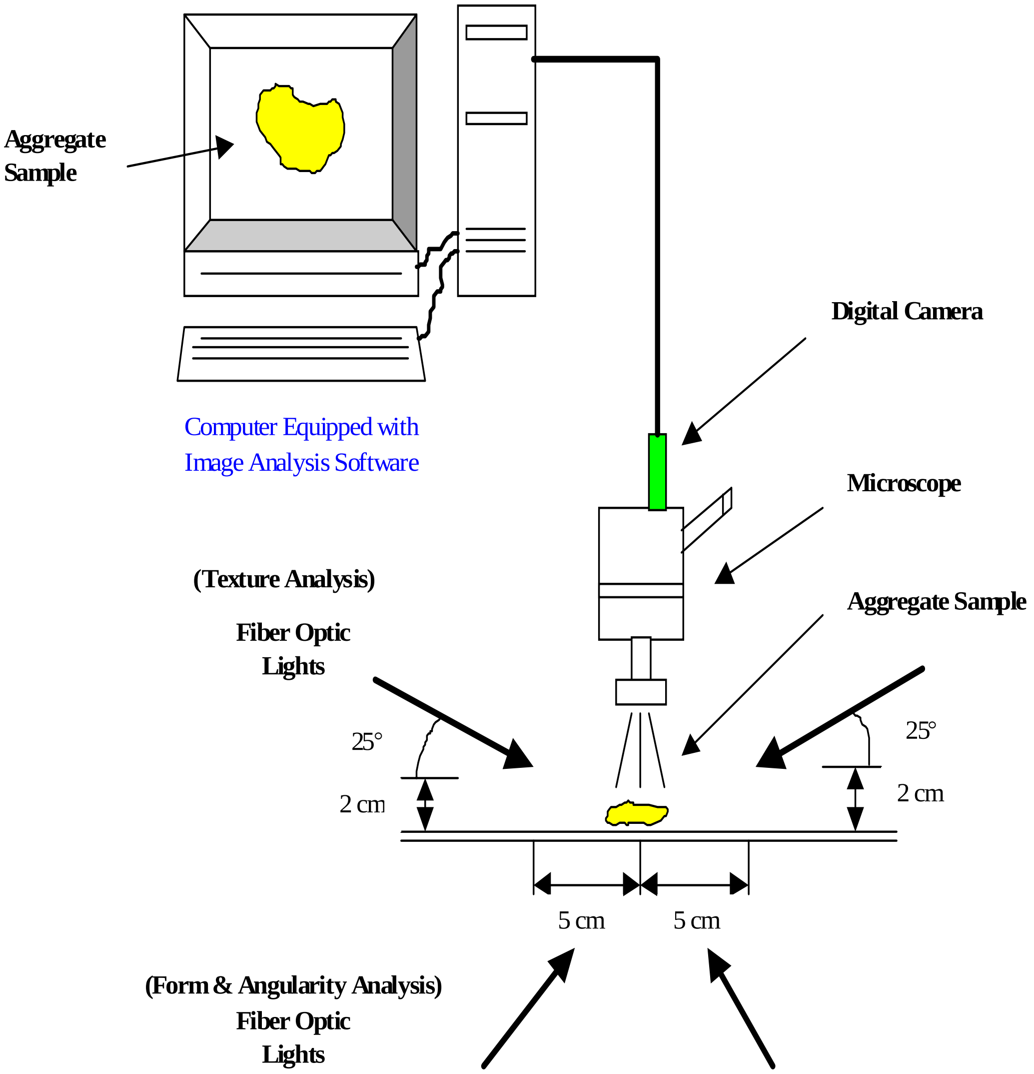

FIGURE 3.3 Image Analysis System (50)

Masad et al. (52) proposed the use of a parameter in order to quantify a particle form that utilizes the incremental change in the particle radius in all directions in order to quantify a particle form. The radius is defined as the length of the line that connects the particle center to points on the boundary. This form index is expressed as:

$$\text{Form Index} = \sum_{\theta=0}^{\theta=360-\Delta\theta} \frac{\left|R_{\theta+\Delta\theta} - R_{\theta}\right|}{R_{\theta}} \tag{3.1}$$

Where R: the radius of the particle in different directions, and

θ: the directional angle.

If the form index is zero, it means that there is no changes in radii and thus, the particle shape is circle. The form index takes into account the changes in particle dimension in all directions.

Aggregate angularity is measured using the gradient method. In this method, the change in the gradients on the boundary of a two-dimensional projection of a particle is calculated (53).

Smooth particles have small gradients while rough particles have higher gradients. Texture is analyzed using the wavelet transform, which captures the changes of texture on gray scale images. The wavelet transform gives a higher texture index for particles with rougher surfaces. The surface irregularities manifest themselves in a gray-scale image as variations in gray-level intensities that range from 0 to 255. Large variation in gray-level intensity means a rough surface texture, whereas a smaller vaiation in gray-level intensity means a smooth particle. The Shape properties are represented by cumulative distribution functions as it is common practice to represent aggregate gradation using a cumulative distribution function (53).

AGGREGATE SHAPE AND GRADATION PARAMETER MODEL

In this study, we used a three-parameter Equation to fit cumulative distribution functions of aggregate gradation and shape properties. Equation 3.2 provides a continuous fit for the gradation curves (54). Equation parameters, called g-values for the size gradation curve, can then be used to quantify the continuous relationships that define size gradation. Similar values are used to quantify form distribution.

$$P_p = \frac{100}{\ln\left[\exp(1) + \left(\frac{g_a}{d}\right)^{g_n}\right]^{g_m}} \tag{3.2}$$

where:

P_p = percent passing a particular grain-size, d,

g_a = fitting parameter corresponding to the initial break in the grain-size curve,

g_n = fitting parameter corresponding to the maximum slope of the grain-size curve,

g_m = fitting parameter corresponding to the curvature of the grain-size curve,

d = particle diameter (mm).

Non-linear regression analyses are performed to obtain a set of parameters that fit a specific gradation. Figures 3.4 through 3.6 show the effect of varying the three parameters g_n, g_m, and g_a on the particle gradation curve. Figure 3.4 shows that when the g_n and g_m are fixed, the parameter g_a is related to the percent of coarse aggregates. It can be seen from Figure 3.5 that parameter g_n controls the slope of gradation curve which determines if the gradation curve is open, gap or well graded. When the value of the parameter g_n increases, the gradation moves toward a gap-gradation, and slope differences between the slopes in the early and latter portion of the curves become more severe; see the change in curve shape as the g_n values change from 1.5 to 10. Figure 3.6 indicates that the parameter g_m governs the fine aggregate content and thus, a parametric study varying g_m can be used to investigate the effect of fine content on the level of anisotropy of the aggregate blend. A smaller value of g_m represents a higher level of fines. The g-coefficients in Equation (3.2) can be replaced with f-, a-, and t-coefficients when used to fit the distribution of form, angularity, and texture, respectively.

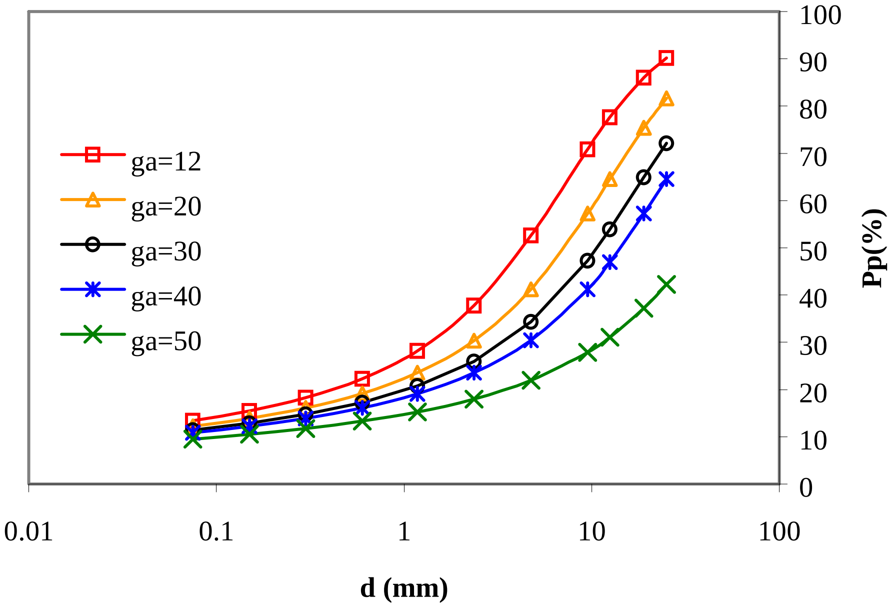

FIGURE 3.4 Sample Plots with g_n = 1.544 and g_m = 0.9764 (g_a varies)

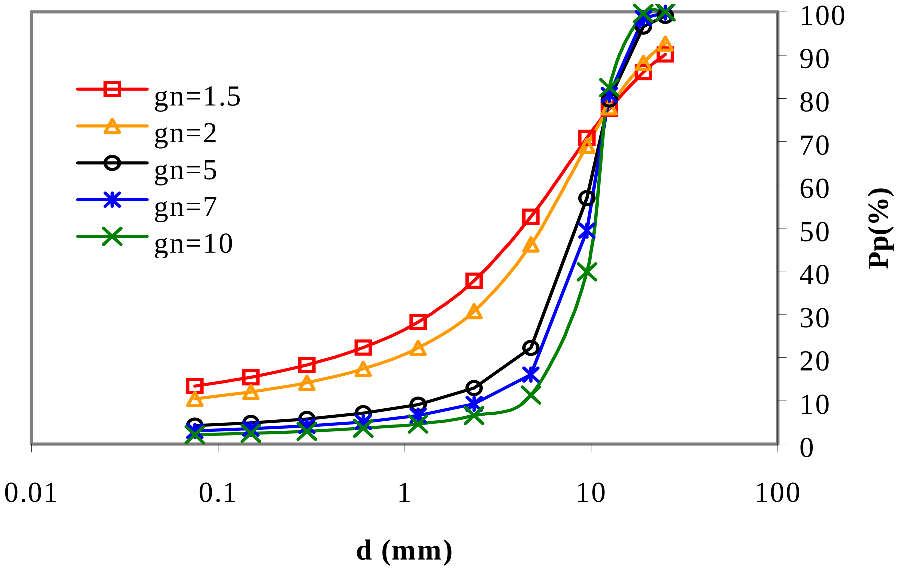

FIGURE 3.5 Sample Plots with g_a = 11.997 and g_m = 0.9764 (g_n varies)

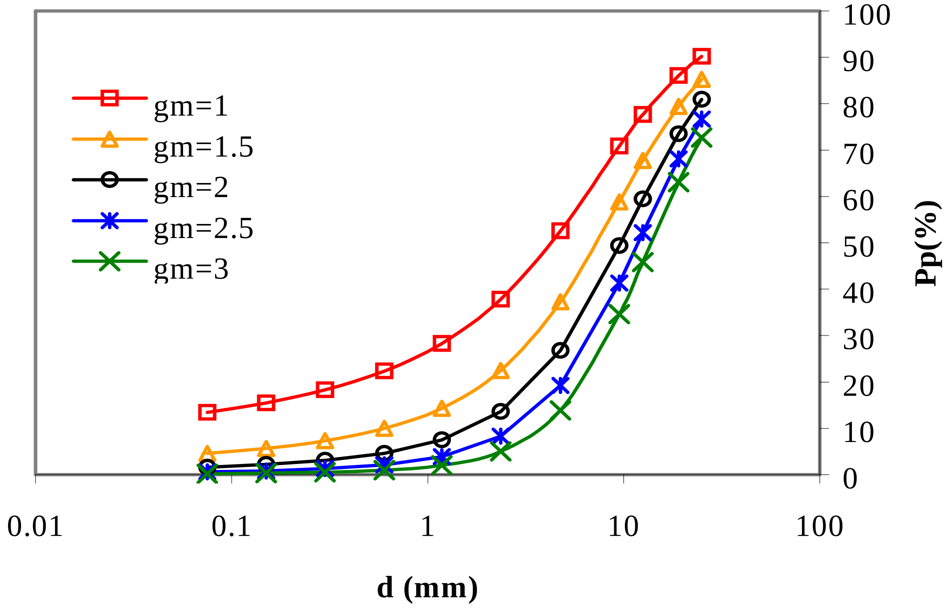

FIGURE 3.6 Sample Plots with g_n = 1.544 and g_a = 11.997 (g_m varies)

STATISTICAL CORRELATIONS

Because of the need to account for stress-sensitivity and cross-anisotropy in characterizing unbound aggregate layers, the experimental protocol required to determine the k_1 to k_9 coefficients can be time consuming. New procedure offers an alternative approach to characterize cross-anisotropy by simply measuring k_1 through k_3 following a traditional protocol such as AASHTO T 307-99 and then approximating the level of anisotropy from statistical relations.

We found that the sphericity, angularity, and texture were highly correlated in the three materials investigated. It is reasonable that the k-values are related to aggregate shape and gradation properties and ratios such as k_4/k_1, k_7/k_1, k_5-k_2, k_6-k_3, k_8-k_2, and k_9-k_3

which define the level of anisotropy are also related to these gradation and shape properties.

These statistical relations can possibly approximate the level of cross-anisotropy from repeated load triaxial tests in which only vertical resilient modulus is measured (k_1 through k_3). Once this is accomplished, the modular ratios (E_x/E_y and G_{xy}/E_y) can be determined using Equations (3.3) and (3.4). The obtained level of anisotropy is used as input for mechanistic computer program. Following section describes the mechanistic computer model to account for the anisotropic behavior of unbound aggregate base.

$$E_x / E_y = \frac{k_4}{k_1}\left(\frac{I}{P_a}\right)^{k_5 - k_2}\left(\frac{\tau_{oct}}{P_a}\right)^{k_6 - k_3} \tag{3.3}$$

$$G_{xy} / E_y = \frac{k_7}{k_1}\left(\frac{I}{P_a}\right)^{k_8 - k_2}\left(\frac{\tau_{oct}}{P_a}\right)^{k_9 - k_3} \tag{3.4}$$

MECHANISTIC COMPUTER MODEL

Recommendations developed in NCHRP 1-26 Phase I indicated that the elastic layer programs (ELPs), such as BISAR, WESLEA, CHEVRON, JULEA, ELSYM5, and KENLAYER, and finite element programs (FEP), like ILLI-PAVE and MICH-PAVE are adequate to support the development of mechanistic-empirical pavement thickness design procedures. In the ELPs, which are computationally much simpler than the finite-element models (FEMs), pavement materials are assumed to be linearly elastic, isotropic, and homogeneous within well-defined horizontal layers. The stress- and direction-dependent (anisotropic) mechanical properties of the unbound granular materials and subgrade soils naturally conflict with the previous assumptions. The limitation of the

ELPs is that moduli are kept constant within each horizontal layer and thus, the material non-linearity which exists in unbound granular material is not considered and the variation of horizontal stress distributions along depth are not effectively taken into account. The FEMs, on the other hand, easily accommodate irregular geometries and anisotropic and stress-dependent material properties and provide the most modern technology and the state-of-the-art sophisticated characterization of the pavement materials. Such realistic characterizations of the UABs accomplished through the use of finite element solutions significantly improve the ability to reliably predict pavement responses, which leads to a better design methodology. The consideration of the nonlinear cross-anisotropic behavior of unbound aggregate base is still in its early stage in the ELPs and FEMs.

There are currently only few ELPs and FEM programs existing that possibly take into account the cross-anisotropic analysis, which are CIRCLY and TTIPAVE. CIRCLY is a layered elastic program which has special ability to consider material anisotropy of each layer and TTIPAVE is a finite element program which accounts for linear, nonlinear, isotropy, and anisotropic model in the unbound granular layer.

Finite Element -Cross Anisotropic Model

The finite element method has capability to consider the material non-linearity, different types of loading conditions, and interface conditions. Since unbound aggregate materials are known to show nonlinear behavior, many researchers have preferred to use the finite element method for analysis of the unbound granular base in a flexible pavement. However, significant problem that tends to predict the horizontal tensile stress at the bottom of unbound granular layer was encountered. To make up the defects of predicting the tensile stress at the bottom of base layer, efforts to incorporate the cross-anisotropic model in the finite element program such as GT-PAVE and TTI-PAVE has been made by several researchers (2, 4, 14, 15).

TTI-PAVE is an axisymmetric finite element program using elasto-plastic theory and has been developed to model a flexible pavement’s response to traffic loads. The finite element code originally developed by Owen and Hinton (55) was modified to analyze an axisymmetric problem with material non-linearity. Park (56) made modifications for stress dependent Poisson's ratio and non-linear analysis using load increments. Adu-Osei (2) made efforts to modify the code to incorporate a cross-anisotropic model.

TTI-PAVE uses axisymmetric, isoparametric 8-node elements and a 3rd order quadrature with 9 integration points . The material parameters needed for the finite element analysis are the non-linear vertical resilient modulus k-values (k_1, k_2, k_3), the moduli ratios (*n=Ex/Ey*, *m=Gxy/Ey*) and the value of the vertical Poisson's ratio as well as the ratio of the horizontal to vertical Poisson's ratios. Since the moduli ratios were observed as constant for a particular material at all stress states, horizontal and shear moduli ratios were used as an input instead of k_1 through k_9.

The vertical Poisson's ratio was assumed to be stress-dependent and parameters, k1,k2, and k3 are used to predict the Poisson's ratio (13) as expressed by Equation (3.5):

$$\frac{2}{3}\frac{\partial \nu_{xy}}{\partial J_2^{\prime}}+\frac{1}{I_1}\frac{\partial \nu_{xy}}{\partial I_1}=\nu_{xy}\left[\frac{1}{3}\frac{k_3}{J_2^{\prime}}+\frac{k_2}{I_1^2}\right]+\left[-\frac{1}{6}\frac{k_3}{J_2^{\prime}}+\frac{k_2}{I_1^2}\right] \qquad (3.5)$$

where,

ν = Poisson's ratio,

k_1, k_2, k_3 = material coefficients,

I_1 = normalized first stress invariant, and

J_2 = normalized second invariant of the deviatoric stress tensor.

A numerical solution to Equation 3.5 based on the backward difference method was included in the finite element code by Park (56). Park (56) described the numerical stepwise solution in detail. To ensure convergence, two convergence criteria were included in the finite element program. The equilibrium criteria is based on residual force values such that:

$$\frac{\sqrt{\sum_{i=1}^{N}(\psi_i^r)^2}}{\sqrt{\sum_{i=1}^{N}(f_i)^2}} \times 100 \leq TOLLER \qquad (3.6)$$

where,

N = the total number of nodal points,

r = the iteration number,

ψ = the total applied force,

f = the applied nodal force, and

TOLLER = tolerance in convergence (percent).

To avoid unreasonable moduli predictions at low stress levels, cutoff values for both the first stress invariant and octahedral shear stress are used. The shortcoming of TTI-PAVE is that the maximum input for Poisson's ratio value is confined as 0.48 albeit Poisson's ratios above 0.5 are frequently observed in the laboratory. This shortcoming would be covered by the field conditions, which has residual and confining stress. The details on the nonlinear solution technique are described elsewhere (2).

Layered Elastic - Cross Anisotropic Surrogate Model

The NCHRP research team for project 1-37A has selected a layered elastic model of the pavement to be used in the proposed 2002 AASHTO Pavement Design Guide. This fact alone emphasizes the importance of being able to assess anisotropic effects using elastic layered systems instead of using solution methodologies based on finite element analysis. CIRCLY is a layered elastic model developed by the Australian Road Research Board (57, 58), which can model cross-anisotropic effects in a layered elastic model. CIRCLY can also model the interface between layers as either rough or smooth. It has been reported that the response of the granular layers characterized as cross-anisotropic model in CIRCLY program shows better predictions than the similar response to the field measurement (59). Although the degree of anisotropy is recommended as 2 for pavement design in Australia and New Zealand, an area of fruitful future study would be to alter modular ratios on a trial and error basis to determine what modular ratio provides the best match with actual, measured parameters.

Linear Elastic - Isotropic Model

It has been well known that the unbound aggregate bases show nonlinear and stress dependent behavior (60, 61). The stress variations along the radial and vertical directions from the surface load result in modulus variations in the radial and vertical direction. Thus, it is theoretically not correct to use a stress at a single point in the nonlinear layer to compute the modulus of the layer. Albeit the Finite Element Method (FEM) provides the best solutions for such nonlinear problems, the Layered Elastic Program (LEP) is more favorable to pavement designer due to its simplicity and short computer running time. If only the most critical strains such as the tensile strain at the bottom of asphalt layer and the compressive strain on the top of subgrade are required, it is possible to select a point in the base layer to compute the modulus, so that these critical responses obtained from LEP and FEM can match reasonably well. Although Huang (12) tried to compare the results from KENLAYER and finite element programs (MICH-PAVE, ILLI-PAVE), the critical responses from LEM and FEM were not matched well due to the inaccuracy of the finite element solutions. This study attempts to find the appropriate stress for computing the modulus in KENLAYER so that the reasonably same critical strains from nonlinear cross-anisotropic analysis by TTIPAVE can be obtained.

KENLAYER provides the flexible pavement analysis of the multilayer system under single, dual, dual-tandem, or dual-tridem wheels with each layer behaving differently, either linear elastic, nonlinear elastic, or viscoelastic (12). Three different methods were performed for nonlinear analysis. In method 1, the unbound aggregate base is subdivided into several sublayers and the stresses at the middepth of each sublayer are used as stress points that calculate the modulus. If the horizontal stress is tension (negative), KENLAYER sets the horizontal tensile stress to zero. Thus, this method avoids the unrealistic negative first stress invariant and modulus calculations. In method 2, the unbound aggregate base is regarded as a single layer and appropriate stress point (the upper quarter, upper third, and upper half of the layer) is selected to compute the modulus. Since the selected stress points are within upper part of the base layer (compression zone), the negative first stress invariant cannot be calculated in method 2. The method 1 gives more accurate results but it requires more computing time. By selecting an appropriate point for computing the modulus, method 2 yields comparable results. Huang (12) performed the results between method 1 and 2 and observed that the results from method 1 lie between those obtained by method 2, with one stress point at the upper quarter and the other at the upper third. Huang (12) compared the nonlinear solutions of KENLAYER and MICH-PAVE and found that the selection of stress point at upper half with a internal friction angle of 40 degrees gives the best fit in HMA tensile strains, but the match in the subgrade compressive strain is poor when asphalt layer is thin.

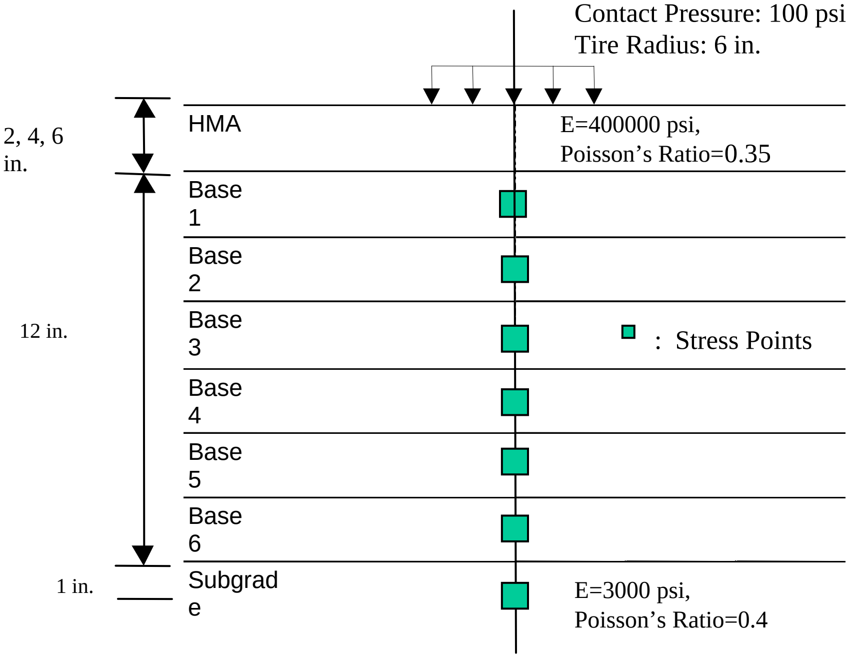

FIGURE 3.7 Method 1 in KENLAYER

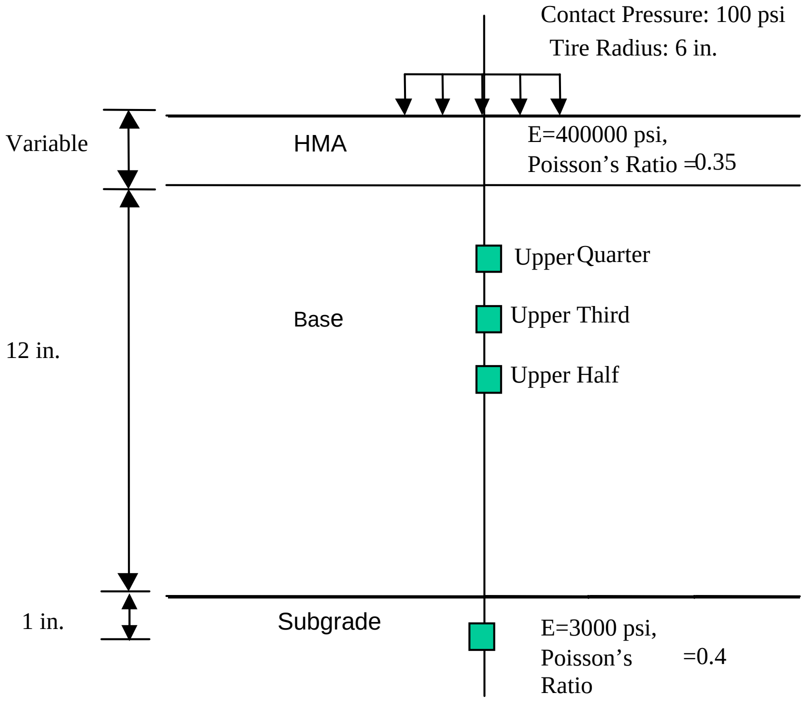

FIGURE 3.8 Method 2 and 3 in KENLAYER

Pavement analysis was performed in method 1 and method 2 using KENLAYER by varying the thickness of HMA and base layer. As shown in Figure 3.7 and 3.8, the HMA thicknesses vary with 2, 4, and 6 inches and the base thickness is 12 inches. KENLAYER incorporates the K-Θ model in the program. Table 3.1 shows the typical ranges of k1 and k2 for unbound aggregate materials and the values of 9000 psi and 0.33 were inputted as k1 and k2, respectively.

Following four cases were considered in KENLAYER and compared with TTI-PAVE.

1. The unbound aggregate base is subdivided into six layers with 2 inches thickness for each sublayer. The vertical coordinates of the stress points are located at mid-depth of each layer and at the 1 inch below the top of subgrade.

2. The unbound aggregate base is regarded as single layer with the stress points at the upper quarter in the layer and at the 1 inch below the top of subgrade.
3. This case is same as case 2 except that the stress point is located at the upper third instead of at the upper quarter.
4. This case is same as case 2 except that the stress point is located at the upper half instead of at the upper quarter.

TABLE 3.1. Range of k1 and k2 for Untreated Granular Materials (12)

Reference	Material	K1 (psi)	k2
Hicks	Partially crushed gravel, crushed rock	1600-5000	0.57-0.73
Hicks and Finn	Untreated base at San Diego Test Road	2100-5400	0.61
Allen	Gravel, Crushed stone	1800-8000	0.32-0.70
Kalcheff and Hicks	Crushed stone	4000-9000	0.46-0.64
Boyce et al.	Well-graded crushed limestone	8000	0.67
Monismith and Witczak	In service base and subbase materials	2900-7750	0.46-0.65

Figures 3.9 through 3.10 shows a comparison of four cases of nonlinear isotropic solutions from KENLAYER with the nonlinear cross-anisotropy solutions from TTIPAVE. Solutions from four cases are getting close together as the HMA thickness increases. The solutions by case 1 were close to those by case 3 and case 4. Especially, the HMA tensile strains by case 1 shows good-agreement with case 4, which has the stress point at the upper half in the layer. It is observed that nonlinear cross-anisotropic solutions by TTIPAVE show higher critical responses than nonlinear isotropic solutions in KENLAYER and TTIPAVE solutions gives best fit in case 4. This is because the computed modulus of the granular base decreases and it results in the increase of vertical

compressive strain at the top of subgrade when the stress point moves down. It is noticed that the case 4 is suitable to obtain comparable critical responses with nonlinear cross-anisotropic solutions. The rut depth has been calculated based on the Tseng and Lytton model and Figure 3.11 shows a comparison of permanent deformation of each case by KENLAYER and TTIPAVE. The dotted line, which is the calculated permanent deformation by case 1 lie between case 3 and case 4. The permanent deformation by TTIPAVE is higher than that of case 1 and fit well with the results of case 4. Therefore, it could be mentioned that the KENLAYER solutions by case 4 are reasonably similar to those by nonlinear cross-anisotropic TTIPAVE solutions.

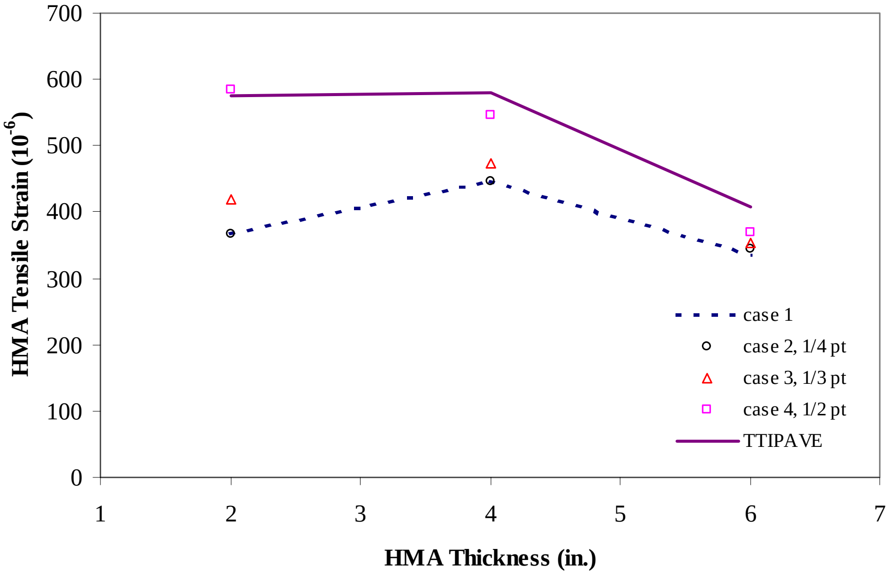

FIGURE 3.9 Nonlinear Solutions of HMA Tensile Strain Between KENLAYER and TTIPAVE

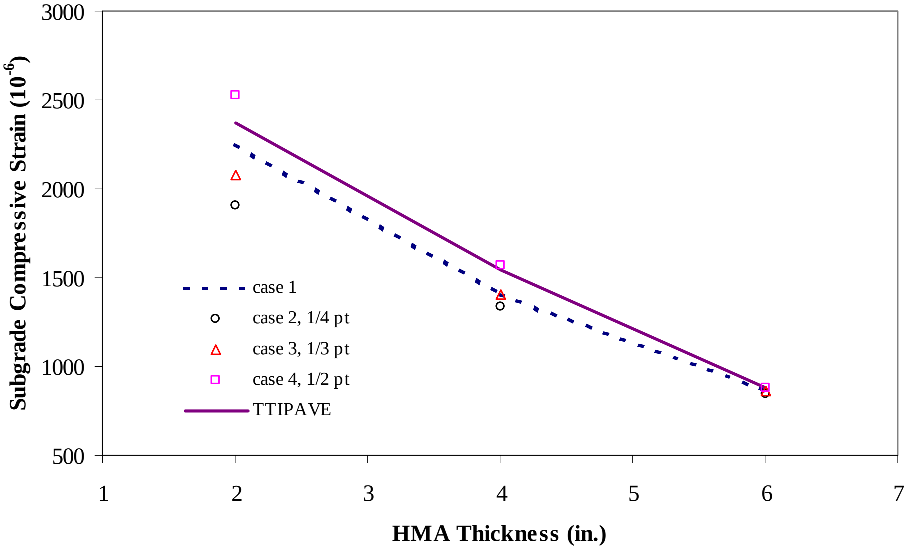

FIGURE 3.10. Nonlinear Solutions of Subgrade Compressive Strain Between KENLAYER and TTIPAVE

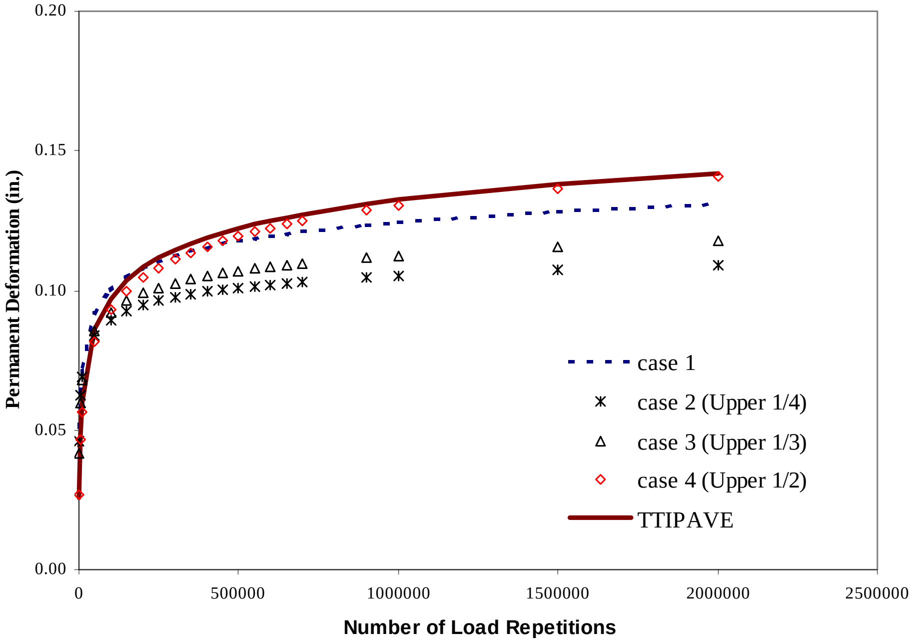

FIGURE 3.11. Comparison of Permanent Deformations Between KENLAYER and TTIPAVE

CHAPTER IV

VARIABLE CONFINING REPEATED LOAD TRIAXIAL TEST

RAPID TRIAXIAL TESTER (RaTT) DEVICE

Several researchers have made efforts to characterize aggregate behavior (62-68). To correctly characterize aggregate behavior, it is important to properly simulate the actual loading conditions in the laboratory. Pavements in the field are usually loaded by moving wheel loads and the major principal stress due to wheel loads is not aligned in the vertical direction, but rotates in the direction of the applied load as load passes. This type of loading can not be ideally simulated in the laboratory by the conventional constant confining pressure type repeated load triaxial tests. The variable confining pressure type repeated load triaxial tests offer the capability to apply a wide combination of stress paths by pulsing both cell pressure and deviatoric stress. Such stress path loading tests better simulate actual field conditions since in the pavement structure the confining stresses acting on the material are cyclic in nature. The University of Illinois FastCell and the Rapid Triaxial Test (RaTT) cell used by TTI are the only equipment that can simulate this field condition in the laboratory.

In this study, the RaTT developed by Industrial Process Controls (IPC), Australia was used for testing. The RaTT cell has internal rubber membrane that can be inflated to apply static and dynamic confining pressure to a sample (69). RaTT cell has special abilities to apply not only the vertical deviatoric and horizontal confining stresses, individually, but also the static and dynamic stress in both vertical and horizontal directions. Horizontal strains are easily measured, which is typically not measured in conventional triaxial test. Figure 4.1 is a picture of the RaTT cell set up. IPC system supports automated control of cell movement and computer control of both confining and axial stress with Linear Variable Differential Transducers (LVDTs) for vertical and horizontal strains. Figure 4.2 and 4.3 are pictures with the cell lowered and raised of the RaTT cell. This automated control of cell movement saves considerable effort and time to get the sample in and out. The apparatus can perform the test at multiple frequencies and stress states. This operation helps to measure resilient response not only time-dependent responses, but also stress-dependent responses of materials.

FIGURE 4.1 RaTT Cell

FIGURE 4.2 Cell Lowered of RaTT Cell

FIGURE 4.3 Cell Raised of RaTT Cell

MATERIALS AND SAMPLE PREPARATIONS

Table 4.1 shows the selected aggregate sources to determine cross-anisotropic elastic properties. The selected materials possess substantially different shape, form and texture properties. Three different gradations which are coarse-graded, well-graded, and fine graded were prepared for all aggregate samples and tested at three different moisture contents which are optimum, dry of optimum, and wet of optimum. Figure 4.4 and Table 4.2 show the three different gradations used in this study. Table 4.3 is the test matrix that was followed in this study. A total of 108 samples (6 materials by 3 gradations by 3 moisture levels by 2 replicates) were tested. However, a number of samples were broken and abandoned because it was too soft for test after compaction.

TABLE 4.1. Aggregate Types

Aggregate #	Producer	Pit	District
1	Marock, Inc.	chambers	fortworth
2	Thompson, Inc., J.R.	Nunnely	Wichita Falls
3	Jobe Concrete Products, Inc	Vado	ElPaso
4	Meridain Aggregate	Mill Creek, OK	Paris
5	Texas Sand & Gravel	Masfield	Amarillo
6	Trinity Materials, Inc	Luckett	Waco

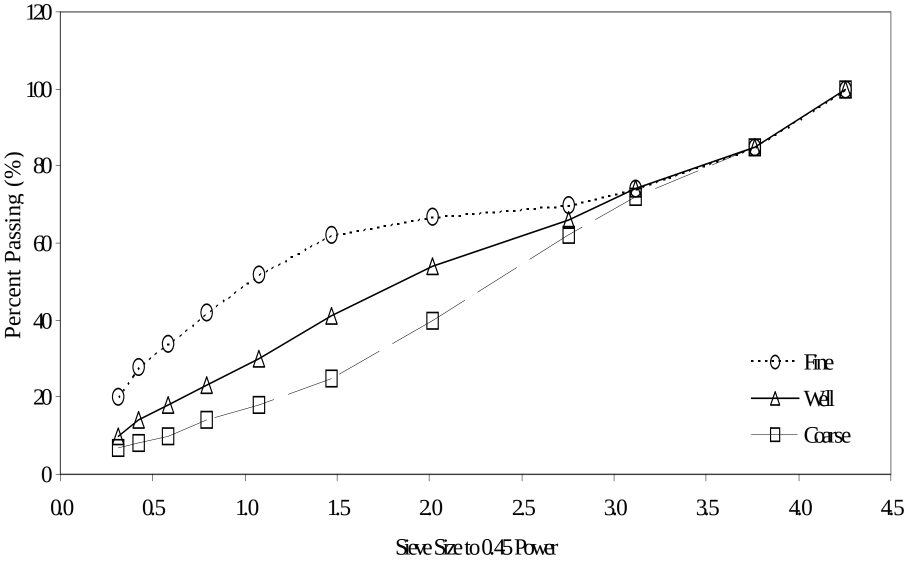

FIGURE 4.4 Gradation on a 0.45 Power Sheet

TABLE 4.2 Gradation

Sieve Size (mm)	Percent Passing (%)		
	Fine Graded	Well Graded	Coarse Graded
25.00	100	100	100
19.00	85	85	85
12.50	74	74	72
9.50	70	66	62
4.75	67	54	40
2.36	62	41	25
1.18	52	30	18
0.60	42	23	14
0.30	34	18	10
0.15	28	14	8
0.075	20	10	7

TABLE 4.3 Test Matrix

	Aggregate Source																	
	Aggregate #1			Aggregate #2			Aggregate #3			Aggregate #4			Aggregate #5			Aggregate #6		
Moisture Conditions	Gradation																	
	C	W	F	C	W	F	C	W	F	C	W	F	C	W	F	C	W	F
Wet	2	2	2	2	2	2	2	2	2	2	2	2	2	2	2	2	2	2
Optimum	2	2	2	2	2	2	2	2	2	2	2	2	2	2	2	2	2	2
Dry	2	2	2	2	2	2	2	2	2	2	2	2	2	2	2	2	2	2

Key:
C- Coarse-graded
W- Well-graded
F- Fine-graded.

A 150-mm in diameter by 150-mm high cylindrical specimens were prepared for testing. This 1:1 height-to-diameter ratio is adequate because the platen is not rigidly fixed to the sample (2). Several samples were prepared using the gyratory compactor and impact compaction methods (70). The specimens in Table 4.3 were compacted with impact compaction method. Samples prepared with the impact compaction method were compacted with AASHTO T-180 using a 4.54 kg hammer and a 457 mm drop. The samples were compacted in 5 layers with high compaction effort with 50 blows for each layer. The prepared specimens were tested with the Rapid Triaxial Tester (RaTT) using the ICAR testing protocol (2, 14, 15). Details of the testing protocol are discussed in Section 4.3.

TESTING PROTOCOL

Researchers at ICAR and the Texas Transportation Institute focused on determining an efficient way to characterize the stress-sensitivity and cross anisotropy of unbound aggregate bases so that these important properties can be properly considered in pavement design approaches such as future upgrades to the 2002 Pavement Design Guide that may ultimately be accepted by AASHTO. In order to numerically solve for the five anisotropic elastic properties, a new testing protocol was developed by International Center for Aggregates Research (ICAR). ICAR test protocol assumes that the elastic moduli obey the Uzan (10) model and thus, the non-linear tangential moduli are smooth functions of the isotropic stress invariants. It is also assumed that the variations of these tangential moduli are negligible within infinitesimal changes in stresses at a particular stress state and thus, at a given stress state, the material is assumed to show linear elastic behavior within a small excursion of stresses. The ICAR protocol uses three stress regimes and ten stress states within each regime to determine stress sensitivity and cross anisotropy. Three stress regimes are conventional triaxial compression, triaxial shear, and conventional triaxial extension.

Conventional Triaxial Compression

In this test mode, the confining stress at each stress state will be kept constant while the axial stress is increased by $\Delta\sigma_y^c$. Thus, the sample will be load to (σ_y^c, σ_x^c), reloaded to ($\sigma_y^c + \Delta\sigma_y^c$, $\Delta\sigma_x^c$), and unloaded back to (σ_y^c, $\Delta\sigma_x^c$) for each cycle.

$$\begin{bmatrix} \dfrac{1}{E_x} & -\dfrac{\nu_{xy}}{E_x} & -\dfrac{\nu_{xx}}{E_x} \\ -\dfrac{\nu_{xy}}{E_x} & \dfrac{1}{E_y} & -\dfrac{\nu_{xy}}{E_x} \end{bmatrix} \begin{Bmatrix} \Delta\sigma_x^c \\ \Delta\sigma_y^c \\ \Delta\sigma_x^c \end{Bmatrix} = \begin{Bmatrix} \Delta\varepsilon_x^c \\ \\ \Delta\varepsilon_y^c \end{Bmatrix} \tag{4.1}$$

where:

$\Delta\varepsilon_x^c$ is a change in radial strain due to an infinitesimal change in axial stress $\Delta\sigma_y^c$ in triaxial compression,

$\Delta\varepsilon_y^c$ is a change in axial strain due to an infinitesimal change in axial stress $\Delta\sigma_y^c$ in triaxial compression, and

$\Delta\sigma_x^c = 0$

Conventional Triaxial Shear

In this phase of the test, the axial stress will be increased slightly by $\Delta\sigma_y^s$, and the confining stress decreased by $\Delta\sigma_x^s = ½\ \Delta\sigma_y^s$. Thus, at the stress state (σ_y^s, σ_x^s), the sample will be loaded to ($\sigma_y^s + \Delta\sigma_y^s$, $\sigma_x^s - \Delta\sigma_x^s$), and unloaded back to (σ_y^s, σ_x^s) per each cycle. This way, there is no change in the first stress invariant, I.

$$\begin{bmatrix} \frac{1}{E_x} & -\frac{\nu_{xy}}{E_x} & -\frac{\nu_{xx}}{E_x} \\ -\frac{\nu_{xy}}{E_x} & \frac{1}{E_y} & -\frac{\nu_{xy}}{E_x} \end{bmatrix} \begin{Bmatrix} \Delta\sigma_x^s \\ \Delta\sigma_y^s \\ \Delta\sigma_x^s \end{Bmatrix} = \begin{Bmatrix} \Delta\varepsilon_x^s \\ \\ \Delta\varepsilon_y^s \end{Bmatrix} \tag{4.2}$$

Conventional Triaxial Extension

In this phase of the test, there is a slight decrease in the axial stress by $\Delta\sigma_y^e$, and a slight increase in the confining stress by $\Delta\sigma_x^e$. Thus, at the stress state (σ_y^e, σ_x^e), the sample will be loaded to ($\sigma_y^e - \Delta\sigma_y^e$, $\sigma_x^e + \Delta\sigma_x^e$), and unloaded back to (σ_y^e, σ_x^e) per each cycle.

$$\begin{bmatrix} \frac{1}{E_x} & -\frac{\nu_{xy}}{E_x} & -\frac{\nu_{xx}}{E_x} \\ -\frac{\nu_{xy}}{E_x} & \frac{1}{E_y} & -\frac{\nu_{xy}}{E_x} \end{bmatrix} \begin{Bmatrix} \Delta\sigma_x^e \\ \Delta\sigma_y^e \\ \Delta\sigma_x^e \end{Bmatrix} = \begin{Bmatrix} \Delta\varepsilon_x^e \\ \\ \Delta\varepsilon_y^e \end{Bmatrix} \tag{4.3}$$

where:

$\Delta\varepsilon_x{}^e$ is a change in radial strain due to an infinitesimal change in axial stress $\Delta\sigma_y{}^c$ and radial stress $\Delta\sigma_x{}^e$, and

$\Delta\varepsilon_y{}^c$ is a change in axial strain due to an infinitesimal change in axial stress $\Delta\sigma_y{}^c$ and radial stress $\Delta\sigma_x{}^e$.

The stresses applied and the strains obtained from the three stress regimes described are used in a system identification scheme to determine the five cross-anisotropic parameters.

At each static stress state, small dynamic changes in stresses are applied to obtain three triaxial stress regimes such that the net stress changes represent triaxial compression, triaxial shear, and triaxial extension. A loading cycle of dynamic stress consists of 1.5 seconds loading and 1.5 seconds unloading period. A dynamic loading is applied to a sample for 25 repetitions until a stable resilient strain is achieved. The resilient axial and radial strains are determined for each stress regime and implemented in the system identification scheme to backcalculate the five anisotropic elastic properties at that particular stress state. The applied static and dynamic stresses are shown in Table 4.4.

TABLE 4.4 Static and Dynamic Stresses

Stress State	Static Stress (kPa)		Dynamic Stress (kPa)					
			Triaxial Compression		Triaxial Shear		Triaxial Extension	
	σ_y	σ_x	$\Delta\sigma_y^c$	$\Delta\sigma_x^c$	$\Delta\sigma_y^s$	$\Delta\sigma_x^s$	$\Delta\sigma_y^e$	$\Delta\sigma_x^e$
1	40	25	5	0	10	-5	-5	5
2	50	25	10	0	10	-5	-10	5
3	70	40	10	0	10	-5	-10	10
4	130	60	20	0	20	-10	-10	10
5	150	70	20	0	20	-10	-10	10
6	170	100	20	0	20	-10	-20	20
7	220	120	30	0	30	-15	-20	20
8	250	140	30	0	30	-15	-20	20
9	250	120	30	0	30	-15	-20	20
10	250	105	30	0	30	-15	-20	20

CHAPTER V

LABORATORY TEST RESULTS AND ANALYSIS

GENERAL

Specimens were prepared with three different gradations and three different moisture levels for compaction. Achieved moisture contents and dry densities are tabulated in Table 5.1 through 5.3.

Equation (3.2) was utilized to calculate the gradation parameters, called g-values which quantify a continuous fit of particle size distribution. The calculated g-values are tabulated in Table 5.4. The predicted gradation curves, which is calculated based on gradation parameters show good-match with actual gradations as shown in Figure 5.1. The g-coefficients in Equation (3.2) can be replaced with f-, a-, and t-coefficients when used to fit the distribution of form, angularity, and texture, respectively.

TABLE 5.1 Moisture Contents and Dry Densities of Aggregate #1 and #2

Aggregate #	compaction	Coarse		Well			Fine	
		Dry	Optimum	Dry	Optimum	Wet	Optimum	Wet
1	wc (%)	4.0	4.5	4.6	4.8	5.2	5.6	6.6
	γd (kg/m^3)	2144	2192	2148	2214	2181	2130	2106
2	wc (%)	4.1	4.6	5	5.5	5.7	6.8	8.2
	γd (kg/m^3)	1906	1980	2020	2068	2008	2014	1958

TABLE 5.2 Moisture Contents and Dry Densities of Aggregate #3 and #4

Aggregate #	compaction	Coarse		Well			Fine		
		Optimum	Wet	Dry	Optimum	Wet	Dry	Optimum	Wet
3	wc (%)	4.5	4.9	4.8	6.4	7	5.6	7	7.2
	γd (kg/m^3)	2060	1977	2069	2111	2107	1968	2021	1985
4	wc (%)	3.6	4.0	3.8	4.1	4.6	4.1	4.9	5.7
	γd (kg/m^3)	2002	2040	2005	2052	2012	2015	2223	2102

TABLE 5.3 Moisture Contents and Dry Densities of Aggregate #5 and #6

Aggregate #	compaction	Coarse	Well			Fine		
		Optimum	Dry	Optimum	Wet	Dry	Optimum	Wet
5	wc (%)	4	3.3	4.5	4.9	4.7	5.2	7.2
	γd (kg/m^3)	2143	2087	2199	2140	2060	2118	2013
6	wc (%)	3.0	3.0	4.4	5.0	4.0	5	5.7
	γd (kg/m^3)	2116	2124	2238	2036	2032	2178	2098

TABLE 5.4 Gradation Parameters

Parameter	Coarse Graded	Well Graded	Fine Graded
g_a	13.272	11.997	4.726
g_n	0.988	0.976	1.361
g_m	2.414	1.544	0.685

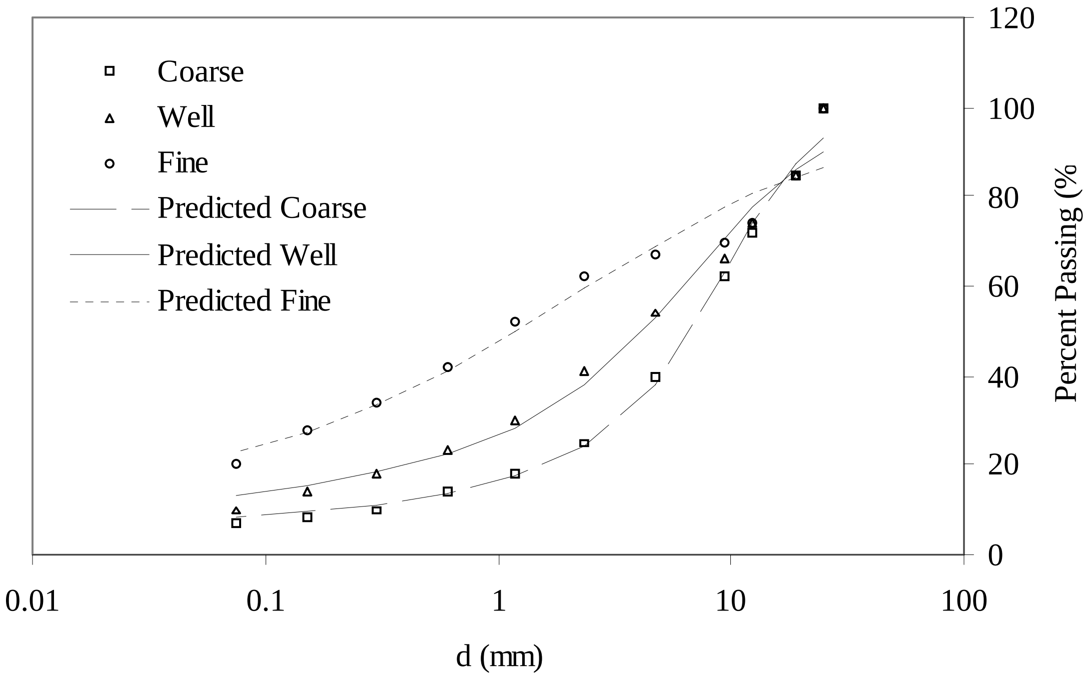

FIGURE 5.1 Gradations with Predictions

Image analysis techniques were utilized to measure the aggregate shape for 50 aggregate particles obtained from each aggregate source. The diameter of particles is 4.75 mm. The measured form, angularity, and texture indices were re-drawn with continuous fit such as particle size distribution. Figures 5.2 shows that aggregates #3 and #4 have the highest form index among aggregate sources. It also illustrates that aggregates #5 and #6 show lower form index than aggregates #1, #2, #3, and #4. Based on these measurements, it can be inferred that aggregates #3 and #4 have more elongated particles than aggregates #1 and #2 while aggregates #5 and #6 have less elongated particles than aggregates #1 and #2. Figure 5.3a shows that aggregates #5 and #6 have lower angularity than other aggregate sources. From Figure 5.3b, it could be mentioned that the lower texture indices that represent smooth texture were observed for aggregate # 5 and #6.

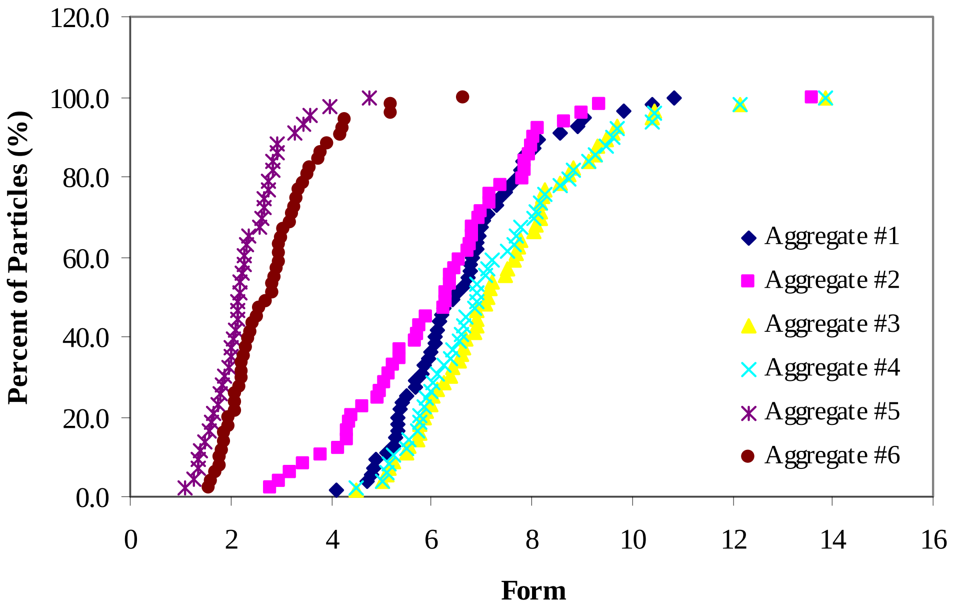

FIGURE 5.2. Cumulative Distribution Curve of Form Index

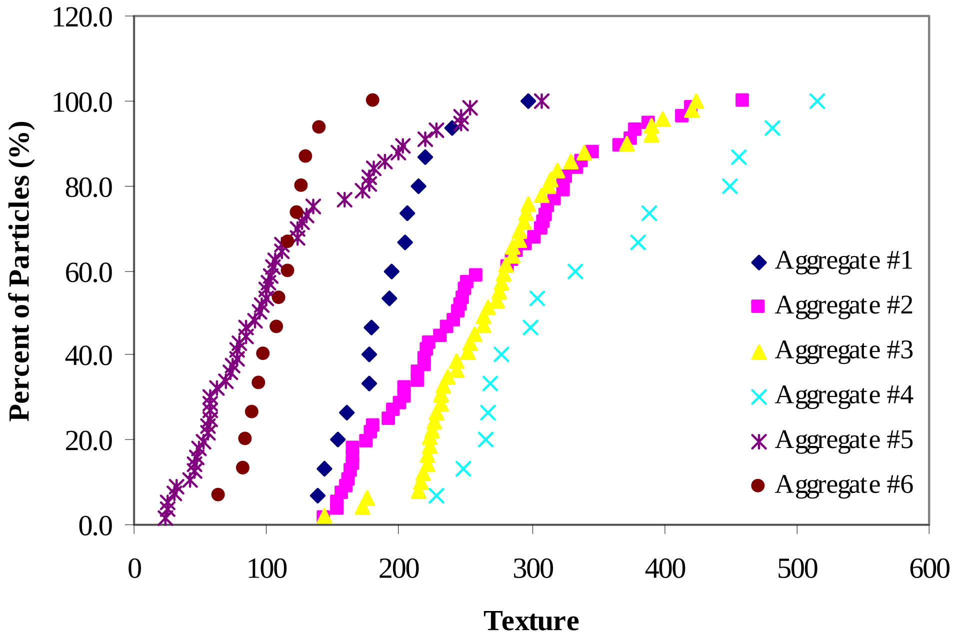

FIGURE 5.3a. Cumulative Distribution Curve of Texture Index

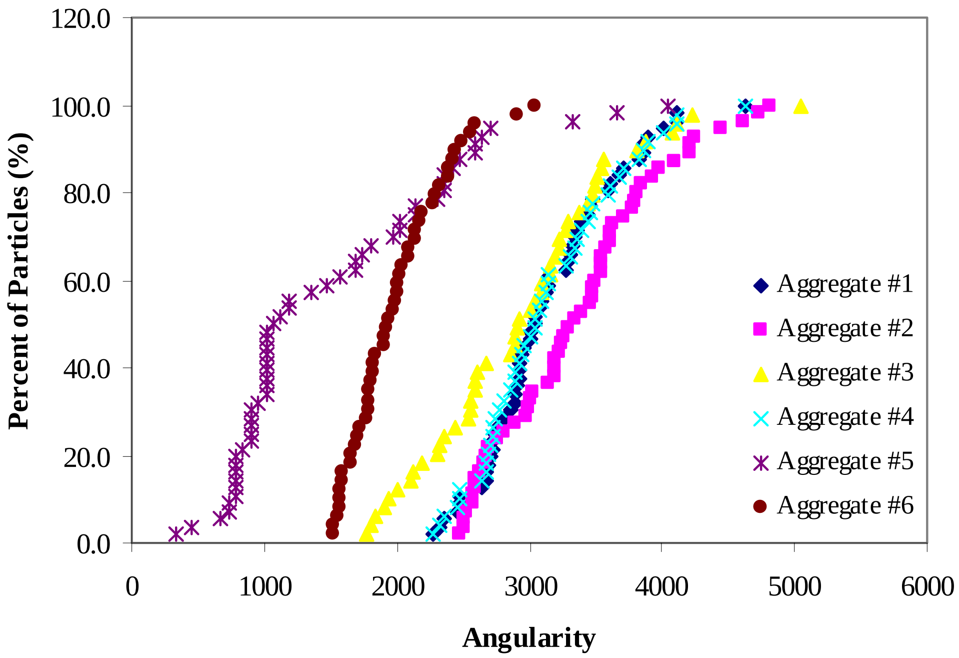

FIGURE 5.3b. Cumulative Distribution Curve of Angularity Index

RAPID TRIAXIAL TEST RESULTS

Repeated triaxial tests using the Rapid Triaxial Tester (RaTT) were performed following the ICAR testing protocol on three aggregate types with three different gradations (coarse, well, and fine) and three different moisture contents (wet, optimum, and dry). Experimental results were analyzed using the ICAR cross-anisotropic model and system identification method. The ICAR model requires nine coefficients to account for the stress-sensitivity and anisotropy of the vertical, horizontal, and shear moduli. Full-scale resilient modulus tests were performed on all combinations and the nine coefficients (k_1 through k_9) were determined. This testing provided the information for an extensive database and offered the opportunity to ascertain whether k-values could be predicted from basic physical properties of the aggregates, including gradation, density, and even perhaps particle shape, etc. The measured resilient axial and radial strains at each stress state were used as an input for the system identification scheme to compute the resilient moduli for vertical and horizontal directions. The static stresses and average resilient strains are tabulated in Table 5.5 and the anisotropic resilient responses obtained from the SID program for aggregate #3 at optimum moisture are tabulated in Table 5.6.

It is generally observed that the vertical resilient moduli are higher than horizontal resilient moduli. Figures 5.4 and 5.5 show the variations of vertical resilient modulus along the first stress invariant and square root of J'_2. The resilient modulus increases both with first stress invariant and square root of J'_2. The moduli tends to peak at high level of J'_2 while it increases with increasing first stress invariant without peak. This illustrates that shear stress significantly affects on the resilient modulus as the stress state increases.

TABLE 5.5 Average Resilient Strains for Aggregate #3 at Optimum Moisture

Stress State		Triaxial Compression		Triaxial Shear		Triaxial Extension	
Stress (kPa)		Strain (με)		Strain (με)		Strain (με)	
Axial	Radial	Axial	Radial	Axial	Radial	Axial	Radial
40.0	25.0	33.1	-6.8	202.1	-120.1	-123.0	61.0
50.0	25.0	65.5	-15.1	130.0	-88.0	-157.5	75.1
70.0	40.0	49.2	-7.4	82.2	-42.3	-169.5	85.3
130.0	60.0	70.1	-14.4	122.9	-83.1	-85.8	58.3
150.0	70.0	61.4	-11.6	101.3	-64.8	-68.6	48.6
170.0	100.0	56.42	-8.4	84.2	-46.8	-138.9	82.4
220.0	120.0	71.5	-11.0	107.9	-63.4	-103.4	71.2
250.0	140.0	61.9	-8.7	91.3	-54.5	-87.8	62.8
250.0	120.0	60.9	-9.7	93.8	-61.0	-88.9	68.7
250.0	105.0	60.1	-10.4	96.6	-68.7	-91.0	73.8

TABLE 5.6 Moduli and Poisson’s Ratios for Aggregate #3 at Optimum Moisture Content

Stress (kPa)		Moduli (MPa)		
Axial	Radial	Vertical	Horizontal	Shear
40.0	25.0	153.0	69.9	42.6
50.0	25.0	176.0	69.7	49.7
70.0	40.0	241.0	116.0	78.5
130.0	60.0	391.0	154.0	106.0
150	70.0	448.0	185.0	125.0
170	100.0	462.0	249.0	156.0
220	120.0	544.0	285.0	178.0
250	140.0	616.0	352.0	210.0
250	120.0	602.0	288.0	188.0
250	105.0	632.0	250.0	171.0

Figures 5.4 and 5.5 show the variation of resilient modulus of well-graded aggregates and higher vertical resilient modulus was obtained for well-graded aggregates #1 and #2 compacted at optimum moisture content. Aggregates #1 and #2, having higher angularity and rough surface texture show higher resilient modulus than other aggregate sources. It is expected that the aggregate particles that have more angularity, rough texture and less elongation provide better load spreading properties and a higher resilient modulus than uncrushed and elongated particles. Thus it can be inferred that the aggregate form, angularity and texture has substantial effects on the unbound aggregate behavior (62).

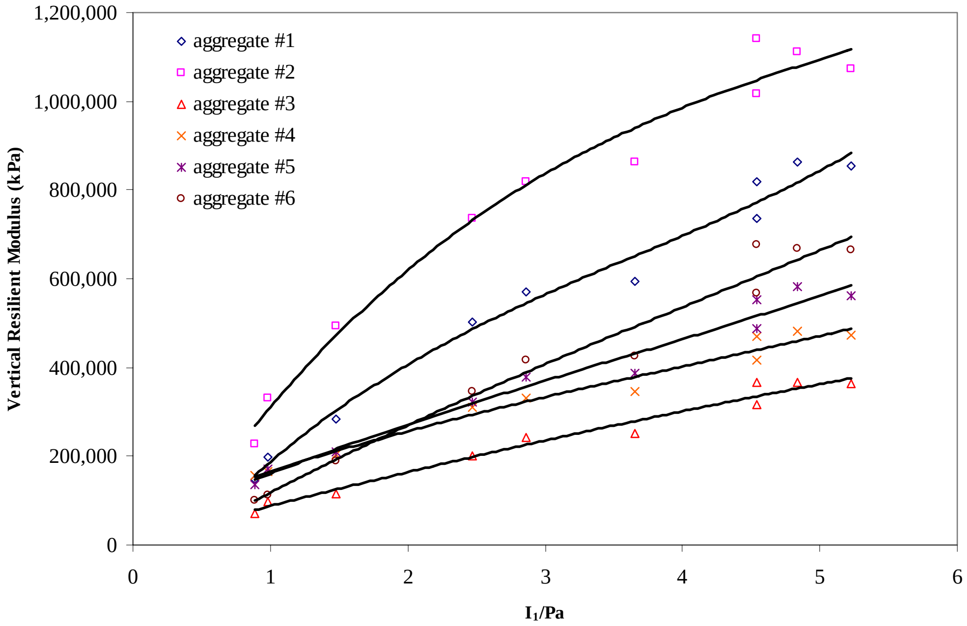

FIGURE 5.4 Vertical Resilient Modulus of Well-Graded Materials along I_1/Pa

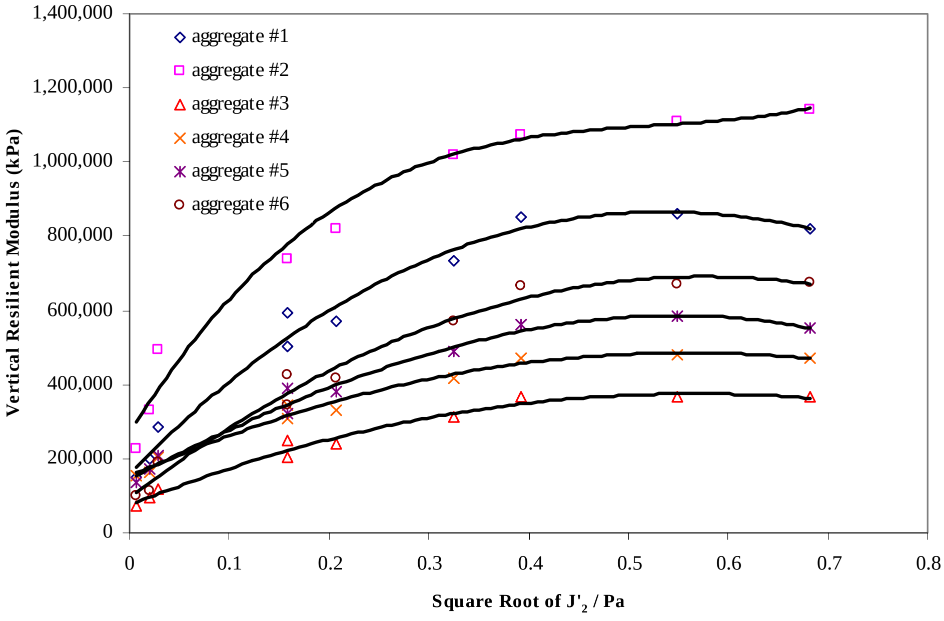

FIGURE 5.5 Vertical Modulus of Well-Graded Materials along Square Root of J'_2/Pa

EFFECT OF GRADATION ON CROSS-ANISOTROPY

The particle size distribution influences on the resilient modulus although it is generally regarded as a minor significance. Figure 5.6 shows the resilient moduli of specimens with fine gradation along the square root of J'_2. By comparing Figure 5.6 to Figure 5.5, it has been observed that the resilient modulus decreases when more fines are included in the sample. Figures 5.7 through 5.8 show the variation of the vertical resilient modulus at optimum moisture content with different gradations. In Figure 5.7, coarse graded aggregate #3 compacted at the optimum moisture content showed higher resilient than well-graded one. Aggregate #3 is composed of angular and rough textured aggregate particles. Thus, this behavior can be explained by the increase of contacts by angular and rough textured particles resulting in strong interlocking. For aggregate #5 which has the lower angularity, higher resilient modulus was observed when well-graded samples were tested rather than coarse-graded samples. The results show the strong interactions between the effects of shape and gradation.

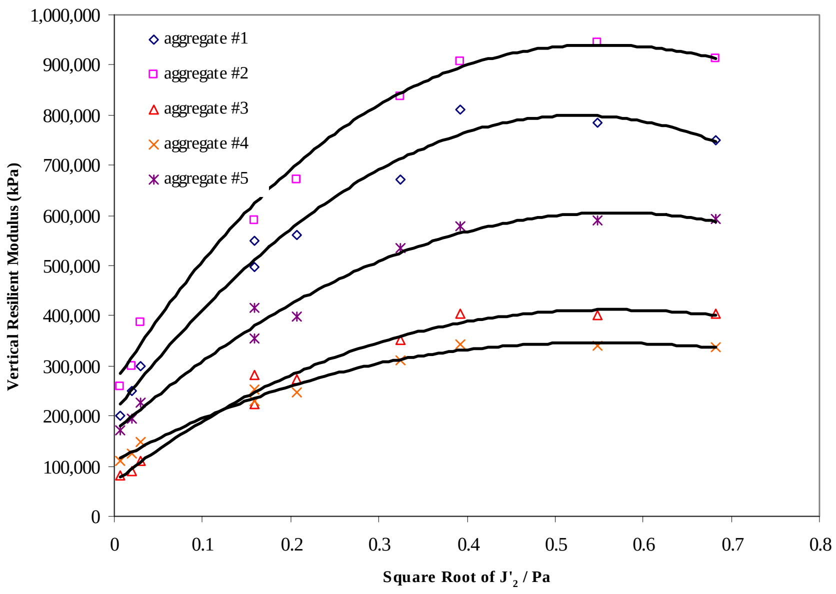

FIGURE 5.6. Vertical Modulus of Fine-Graded Materials along Square Root of J'_2/Pa

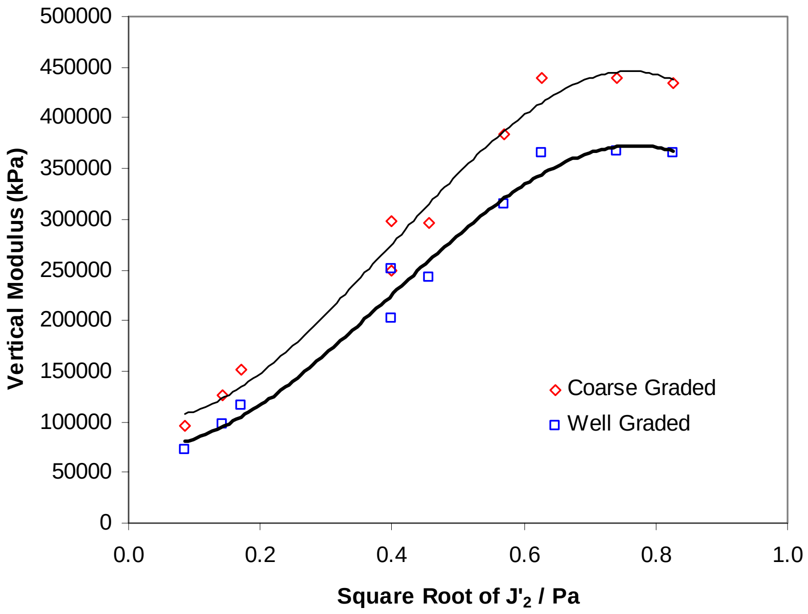

FIGURE 5.7. Variation of Vertical Modulus for Aggregate #3 at Optimum Moisture Content

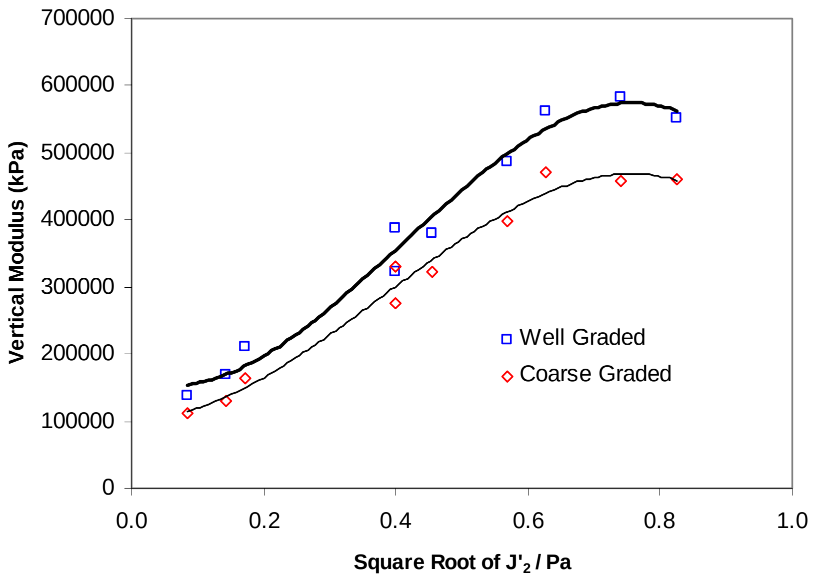

FIGURE 5.8. Variation of Vertical Modulus for Aggregate #5 at Optimum Moisture Content

EFFECT OF MOISTURE CONTENT ON CROSS-ANISOTROPY

From Figure 5.9 through 5.14, samples compacted at optimum and dry of optimum moisture content generally showed higher resilient moduli than ones compacted at wet of optimum moisture content. Figure 5.9 shows the variation of resilient modulus along the moisture content and explains that the resilient modulus of dry of optimum and optimum moisture content is similar, but as complete saturation is approached, the resilient modulus decreases significantly. It also shows that a significant dependence of resilient modulus on moisture content exists with the relations that the modulus decreases with increasing in moisture content.

The resilient modulus in aggregate #3 decreased about 15% as the moisture content increased from 4.3% to 6.8%. Also, it has been observed a 20% decrease in resilient modulus in limestone as the moisture content increased from 5%, which is optimum to 6%. No significant resilient responses were observed between gravel samples compacted at optimum and dry of optimum moisture content.

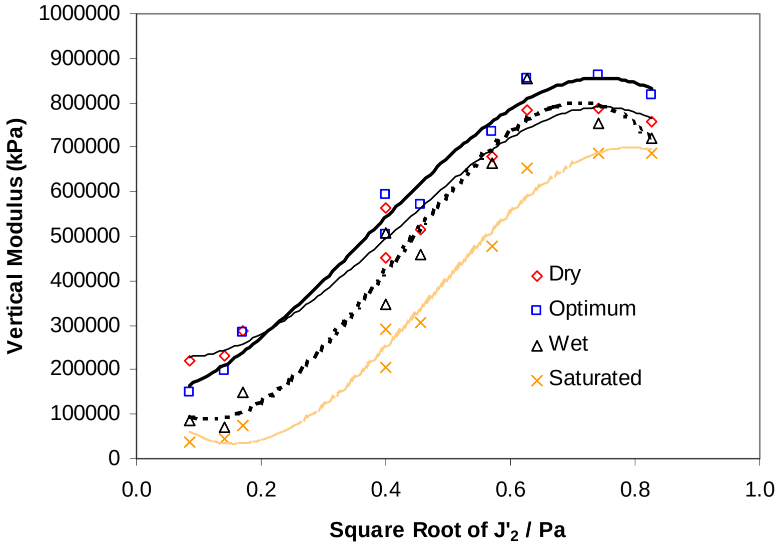

FIGURE 5.9 Variation of Vertical Modulus with Moisture for Well-Graded aggregate #1

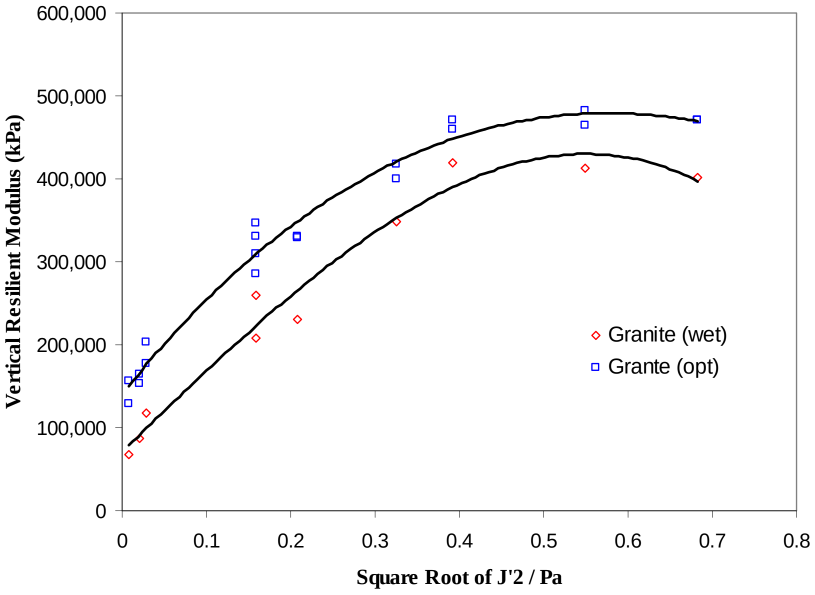

FIGURE 5.10 Variation of Vertical Modulus with Moisture for Well-Graded Aggregates #3 and #4

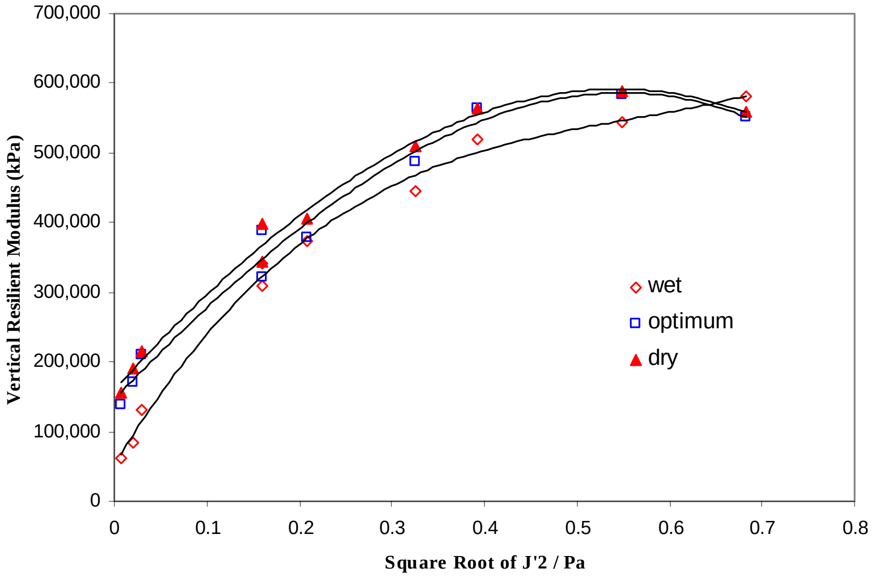

FIGURE 5.11a. Variation of Vertical Modulus with Moisture for Well-Graded aggregate #5

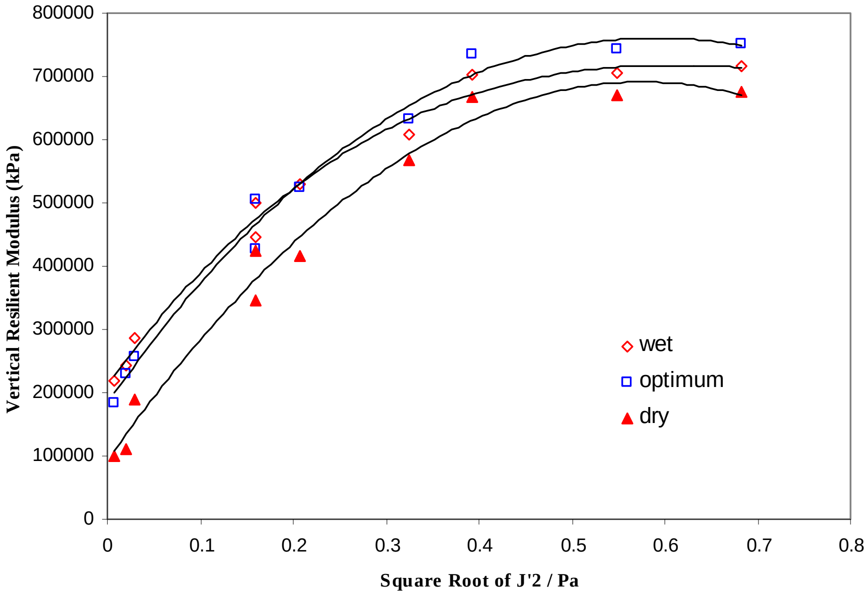

FIGURE 5.11b. Variation of Vertical Modulus with Moisture for Well-Graded aggregate #6

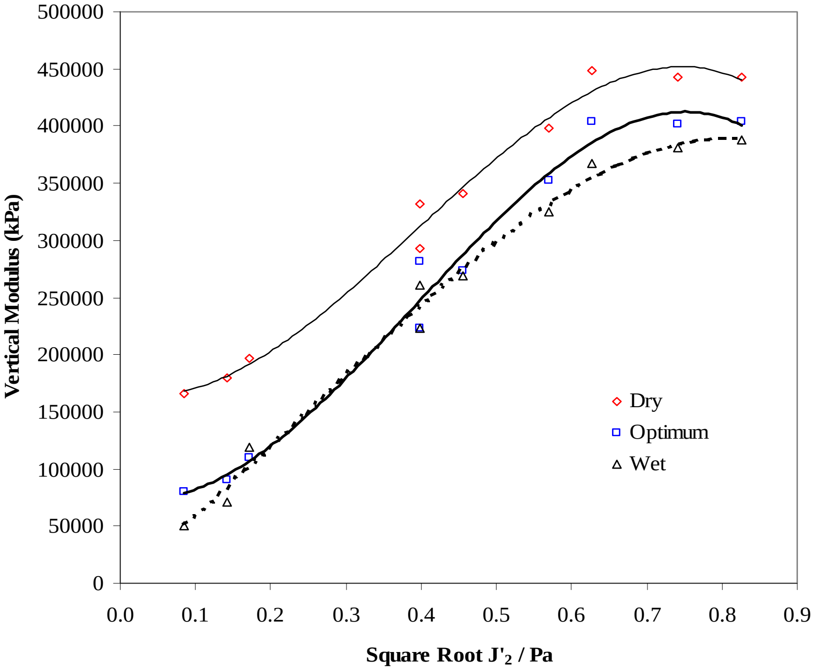

FIGURE 5.12. Variation of Vertical Modulus with Moisture for Fine Graded Aggregate #3

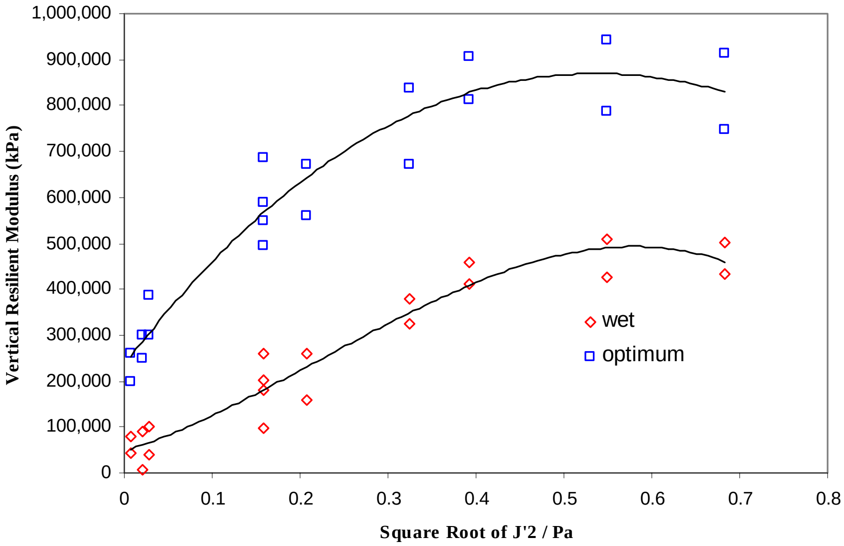

FIGURE 5.13 Variation of Vertical Modulus with Moisture for Fine Graded Aggregate #1 and #2

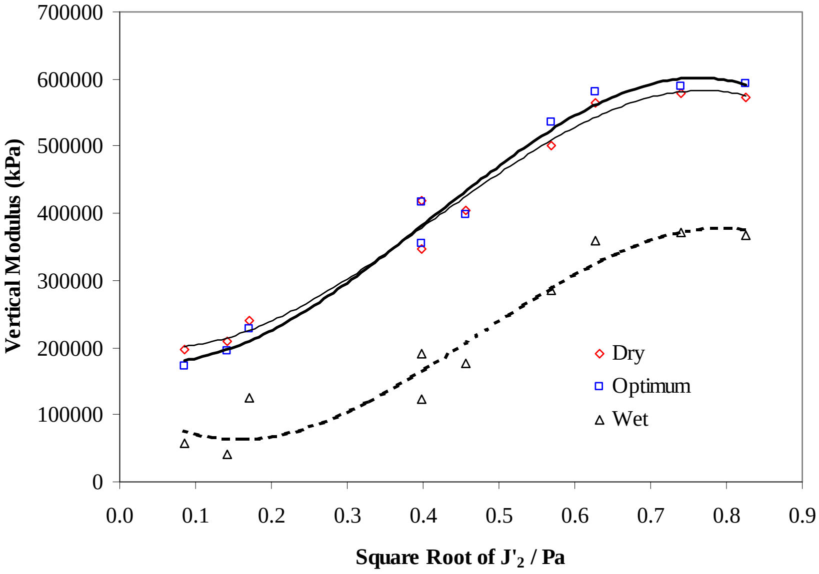

FIGURE 5.14 Variation of Vertical Modulus with Moisture for Fine Graded Aggregate #5 and #6

Regression analysis was performed to determine the k-values that fit with the Uzan models for each gradation and moisture content. The R-square values for k-values were above 0.9. Table 5.7 is summaries of average k-values.

TABLE 5.7 Average k-Values for Aggregates

Nonlinear Anisotropic Analysis										
Materials	Parameters for Ey			Parameters for Ex			Parameters for Gxy			Poisson's ratio
	k1	k2	k3	k4	k5	k6	k7	k8	k9	ν_{xx}/ν_{xy}
Aggregate #1	2519	0.591	0.180	900	0.908	-0.222	489	0.920	-0.100	1.3
	3249	0.515	0.236	852	0.911	-0.275	563	0.862	-0.106	1.3
	3665	0.532	0.226	1672	0.640	-0.175	671	0.866	-0.117	1.4
	4073	0.555	0.308	893	0.971	-0.205	590	0.962	-0.066	1.5
	1432	1.106	0.144	911	1.057	-0.083	430	1.156	0.032	1.5
	4499	0.372	0.166	2469	0.512	-0.058	1070	0.614	-0.049	1.5
	2260	0.726	0.743	160	1.668	-0.266	170	1.446	0.151	1.7
Aggregate #2	6225	0.271	0.357	1129	0.751	-0.313	804	0.715	-0.118	1.5
	6060	0.397	0.204	2824	0.478	-0.102	1428	0.588	-0.036	1.4
	5737	0.420	0.240	2976	0.407	0.039	1229	0.607	-0.056	1.6
	7611	0.321	0.278	2345	0.500	-0.114	1545	0.534	-0.002	1.6
	5802	0.328	0.184	3181	0.297	-0.026	1464	0.464	-0.025	1.5
	851	1.246	0.726	28	2.581	-0.185	31	2.322	0.127	2.4
Aggregate #3	2400	0.478	0.334	501	0.939	-0.342	381	0.846	-0.081	2.2
	3225	0.272	0.446	397	1.046	-0.382	443	0.741	0.005	1.6
	3144	0.348	0.352	571	0.872	-0.373	471	0.740	-0.093	1.3
	1940	0.506	0.356	456	1.070	-0.272	334	0.913	-0.013	1.5
	1564	0.702	0.326	270	1.358	-0.432	247	1.109	-0.082	1.3
	2948	0.326	0.246	759	0.826	-0.374	678	0.569	-0.058	1.3
	1892	0.600	0.375	337	1.244	-0.214	274	1.061	0.016	1.5
	2559	0.408	0.490	488	1.057	-0.071	356	0.909	0.101	1.5
Aggregate #4	2400	0.345	0.293	464	0.966	-0.377	393	0.760	-0.095	1.3
	2928	0.376	0.266	733	0.835	-0.327	580	0.695	-0.055	1.3
	2079	0.381	0.245	621	0.794	-0.202	446	0.668	-0.023	1.6
	2460	0.484	0.296	768	0.859	-0.168	460	0.835	-0.011	1.5

Table 5.7 Continued

Nonlinear Anisotropic Analysis										
Materials	Parameters for Ey			Parameters for Ex			Parameters for Gxy			Poisson's ratio
	k1	k2	k3	k4	k5	k6	k7	k8	k9	ν_{xx}/ν_{xy}
Aggregate #5	3440	0.410	0.310	1396	0.659	-0.142	721	0.694	-0.008	1.3
	3074	0.470	0.309	807	0.939	-0.194	534	0.851	-0.031	1.4
	4762	0.311	0.685	499	1.134	-0.204	491	0.904	0.142	1.5
	3524	0.374	0.264	1587	0.599	-0.178	825	0.625	-0.022	1.5
	3436	0.422	0.291	1170	0.681	-0.242	704	0.687	-0.037	1.4
	1333	0.782	0.510	160	1.577	-0.151	145	1.381	0.144	1.5
Aggregate #6	4708	0.334	0.359	1021	0.873	-0.282	775	0.746	-0.040	1.5
	5262	0.290	0.359	1967	0.655	-0.169	1162	0.607	0.043	1.4
	5068	0.360	0.403	1385	0.776	-0.233	898	0.725	-0.006	1.4
	3283	0.585	0.434	713	1.172	-0.103	502	1.040	0.047	1.7
	3832	0.393	0.649	311	1.278	-0.187	295	1.070	0.041	1.9

REGRESSION MODEL FOR ANISOTROPIC LEVEL DETERMINATION

Tutumluer and Thompson (5) developed a simplified procedure for estimating cross-anisotropic properties from repeated load triaxial test. They observed that Uzan type stress-dependent models in Equation 3.5 and 3.6, when used for modeling the horizontal and shear stiffness ratios, resulted in a constant term (k4/k1 or k7/k1) almost equal to the average ratios predicted by the finite element analysis throughout the base (5).

The data points of bulk stress exponents (k5-k2 or k6-k3) with shear stress exponents (k8-k2 or k9-k3) were generally centered on the equality line indicating that they are equal in magnitude but opposite in sign as shown in Figures 5.15 and 5.16. This indicates that when deviator and bulk stresses take similar values under the applied wheel load, the constant ratio terms (k4/k1 or k7/k1) in the models play the governing role in determining the stiffness ratios. Tutumluer and Thompson (5, 37) analyzed a conventional flexible pavement section with anisotropic resilient models and found that the typically resulted in horizontal modulus varying between 5 % to 30 % of vertical, and the shear modulus between 18% and 35% of the vertical resilient modulus under surface traffic loading throughout the base.

Since those exponent parameters are roughly selected from the center of scattered data points and used as the representative values, other exponent parameters such as k5-k2, k6-k3, k8-k2, and k9-k3 can't be exactly obtained or represent all the scattered data points.

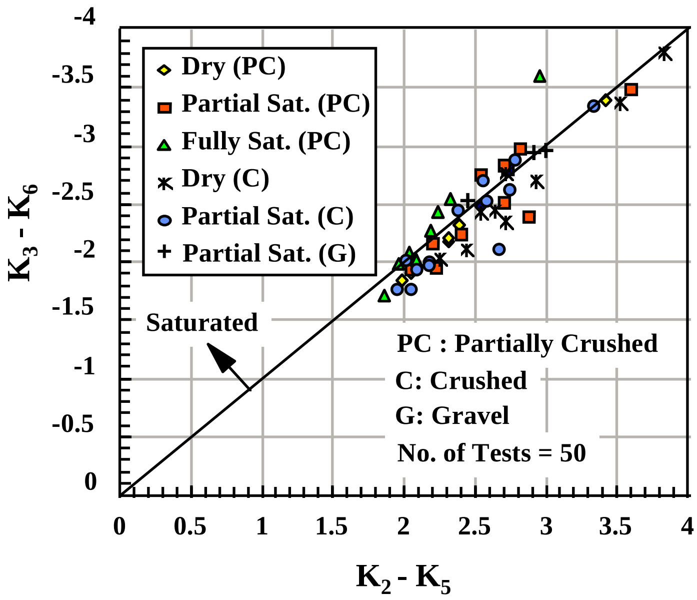

FIGURE 5.15 Variation of Stress Exponents in the Horizontal Stiffness Ratio Model (5)

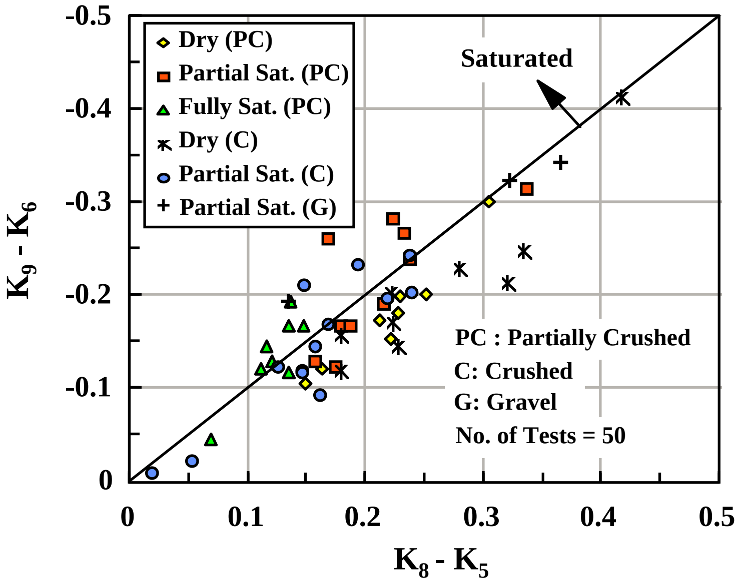

FIGURE 5.16 Variation of Stress Exponents in the Shear Stiffness Ratio Model (5)

The degree of this non-linearity and stress dependency is a function of the stress state, degree of saturation, dry density, level of load, and particle size distribution of the unbound layer material. This was confirmed by Adu Osei et al. (14) experimentally as they compared the impact of aggregate type, aggregate gradation, moisture content, etc. on resilient modulus and permanent deformation. However, such repeated load resilient and permanent deformation tests are time-consuming and expensive to perform and certainly do not lend themselves to routine testing. Since, it is indeed important to be able to consider the stress-sensitive, anisotropic, and time-dependent nature of unbound granular materials in order to realistically model pavement structures containing unbound aggregate layers, a pressing need is to be able to approximate these properties from routine tests.

Adu-Osei et al. (14) studied four different aggregate types. Each aggregate type was prepared at several different gradations, several different moisture contents, and at various densities. Full-scale resilient modulus tests were performed on all combinations and the nine factors (k_1 through k_9) were determined. Because of the need to account for stress-sensitivity and cross-anisotropy in characterizing unbound aggregate layers, the experimental protocol required to determine the k_1 to k_9 coefficients can be time consuming. This time consuming testing provided the information for an extensive database and the experimental results by the author and Adu-Osei et al. (14, 15). This database offered the opportunity to ascertain whether k-values could be predicted from basic physical properties of the aggregates, including gradation, moisture content, and density, etc. Based on additional experimental results form Adu-Osei (2) as well as laboratory results in Table 5.7, multiple regression models were developed in Equation 5.1 to calculate the level of anisotropy from k-values (1 through 3), which are directly measured during laboratory testing.

$$\left\{\begin{matrix} k4/k1 \\ k7/k1 \\ k5-k2 \\ k6-k3 \\ k8-k2 \\ k9-k3 \end{matrix}\right\} = \begin{bmatrix} 1.09 \\ 0.587 \\ -1.50 \\ -0.212 \\ -0.737 \\ 0.336 \end{bmatrix} + \begin{bmatrix} 0.000040 & 0.292 & -0.835 & -0.000367 & -0.00063 & -0.0386 \\ 0.000008 & 0.0609 & -0.338 & -0.000171 & 0.00173 & -0.0176 \\ -0.000072 & -0.294 & 1.75 & 0.000862 & -0.0127 & 0.0883 \\ 0.000057 & 0.342 & -1.17 & -0.000099 & -0.0132 & 0.0207 \\ -0.000019 & -0.0038 & 1.19 & 0.000371 & -0.00115 & 0.0325 \\ 0.000007 & 0.168 & -0.799 & -0.000236 & -0.00011 & -0.0284 \end{bmatrix} \left\{\begin{matrix} k1 \\ k2 \\ k3 \\ \gamma_d \\ g_a \\ g_n \end{matrix}\right\} \begin{pmatrix} R^2 = 71\% \\ R^2 = 72\% \\ R^2 = 76\% \\ R^2 = 73\% \\ R^2 = 78\% \\ R^2 = 81\% \end{pmatrix} \quad (5.1)$$

where,

k_i : material coefficients

γ_d : dry density (kg/m^3)

g_a = fitting parameter corresponding to the initial break in the grain-size curve,

g_n = fitting parameter corresponding to the maximum slope of the grain-size curve,

The variables for Equation (5.1) include the material coefficients, dry density, and gradation and overall R-square value is 71% through 80%. More accurate predictions of k-values could be obtained when the particle shapes such as form, angularity, and texture are taken into account. Fifty particles passing No. 4 sieve size were selected from each aggregate source, and aggregate form, angularity, and texture indices were measured. Aggregate shape indices were represented using a cumulative function such as particle size distribution and shape parameters were calculated based on Equation 5.2. The calculated shape parameters were given in Table 5.8.

$$P_p = \frac{100}{\ln\left[\exp(1) + \left(\frac{f_a}{form\_index}\right)^{f_n}\right]^{f_m}} \tag{5.2a}$$

where:

P_p = percent ratio of aggregate particles with certain form index,

f_a = fitting parameter corresponding to the initial break in the form index curve,

f_n = fitting parameter corresponding to the maximum slope of the form index curve,

f_m = fitting parameter corresponding to the curvature of the form index curve.

$$P_p = \frac{100}{\ln\left[\exp(1) + \left(\frac{A_a}{Angularity\_index}\right)^{A_n}\right]^{A_m}} \tag{5.2b}$$

where:

P_p = percent ratio of aggregate particles with certain form index,

A_a = fitting parameter corresponding to the initial break in the angularity index curve,

A_n = fitting parameter corresponding to the maximum slope of the angularity index curve,

A_m = fitting parameter corresponding to the curvature of the angularity index curve.

$$P_p = \frac{100}{\left[\ln\left[\exp(1) + \left(\frac{T_a}{Texture\_index}\right)^{T_n}\right]\right]^{T_m}} \tag{5.2c}$$

where:

P_p = percent ratio of aggregate particles with certain form index,

T_a = fitting parameter corresponding to the initial break in the texture index curve,

T_n = fitting parameter corresponding to the maximum slope of the texture index curve,

T_m = fitting parameter corresponding to the curvature of the texture index curve.

TABLE 5.8. Aggregate Shape Parameters for Each Aggregate Source

	Aggregate #1	Aggregate #2	Aggregate #3	Aggregate #4	Aggregate #5	Aggregate #6
fa	6.101	6.940	6.805	5.347	2.264	2.332
fm	3.376	1.385	3.246	8.212	2.188	3.924
fn	7.159	7.582	6.524	5.366	5.669	4.190
Aa	1238.895	622.147	165.048	1066.204	87.711	654.794
Am	670.171	2201.664	4344.092	882.510	294.581	789.035
An	6.406	4.072	2.533	5.745	1.915	5.497
Ta	44.062	229.629	242.955	84.485	88.818	17.507
Tm	1437.345	3.078	3.937	308.651	2.608	1653.731
Tn	4.507	4.360	6.878	3.873	2.411	3.659

It is reasonable that the k-ratios k_4/k_1, k_7/k_1, k_5-k_2, k_6-k_3, k_8-k_2, and k_9-k_3 which define the level of anisotropy are related to aggregate shape and gradation properties. By using MINITAB statistical software, Equation 5.3 was developed to approximate cross-anisotropic k-values (k_4 through k_9) from repeated load triaxial tests. The predictors in regression model were selected after performing the best subset method which identifies the best-fitting regression models. The selected aggregate shape parameters for regression model development were ga, gn, fa, fn, Aa, Ta, and Tn.

From Equation 5.3, the constant term, k4/k1 and k7/k1 for anisotropic modular ratio increases when ga increases and gn decreases. An increase in ga indicates that the aggregate gradation becomes coarser. The reduction in gn indicates that the gradation changes from gap graded to well graded. Thus, it could be mentioned that higher modular ratio can be obtained for well graded materials than gap-graded materials. The k4/k1 and k7/k1 increase when fa decreases and fn increases. The aggregate is regarded to have particles with less elongation as fa increases and fn increases. Thus, it is inferred that k4/k1 increases when aggregate particles have less-elongation. Also, k7/k1 increases as particles become less elongated.

The k4/k1 and k7/k1 increase when Aa, Ta, and Tn increase. The increase of Aa and Ta mean that the percentage of particles which have more angularity and texture increases. Thus, it was found that higher angularity and texture result in the increase of both k4/k1 and k7/k1.

$$\begin{Bmatrix} k4/k1 \\ k7/k1 \\ k5-k2 \\ k6-k3 \\ k8-k2 \\ k9-k3 \end{Bmatrix} = \begin{bmatrix} -0.781 \\ 0.312 \\ 1.22 \\ -1.82 \\ -0.19 \\ 0.061 \end{bmatrix} + \begin{bmatrix} -0.000051 & -0.415 & -0.980 & 0.0118 & -0.122 & -0.605 & 0.317 & 0.00151 & 0.00783 & 0.233 \\ 0.0000004 & -0.047 & -0.437 & 0.00047 & -0.0197 & -0.0484 & 0.0095 & 0.000105 & 0.000674 & 0.0202 \\ -0.000007 & 0.222 & 1.72 & -0.0177 & 0.142 & 0.486 & -0.267 & -0.00117 & -0.00622 & -0.176 \\ -0.000046 & -0.172 & -0.982 & 0.0068 & -0.116 & -0.634 & 0.339 & 0.00168 & 0.00871 & 0.218 \\ -0.000031 & -0.031 & 1.19 & -0.00108 & 0.0315 & -0.02 & 0.0428 & 0.000102 & 0.00007 & 0.0066 \\ 0.000013 & 0.160 & -0.695 & -0.00488 & -0.0121 & 0.046 & -0.0349 & -0.000131 & -0.00049 & -0.0262 \end{bmatrix} \cdot \begin{bmatrix} k1 \\ k2 \\ k3 \\ ga \\ gn \\ fa \\ fn \\ Aa \\ Ta \\ Tn \end{bmatrix} \qquad (5.3)$$

Figure 5.17 through 5.22 show the comparisons between measured and predicted k-values. Data points in each figure are centered at the equality line with high R-square values above 0.8. This implies that the prediction models are in good agreement with the experimental measurements and the use of aggregate shape and gradation parameters for estimating the anisotropic level is substantial.

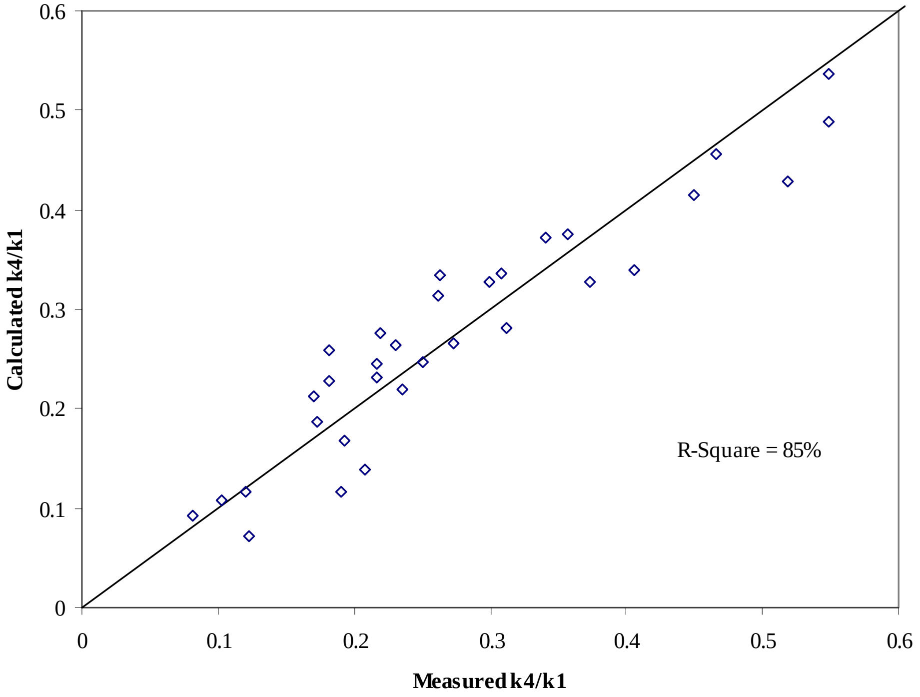

FIGURE 5.17. Comparison of Measured and Calculated k_4/ k_1

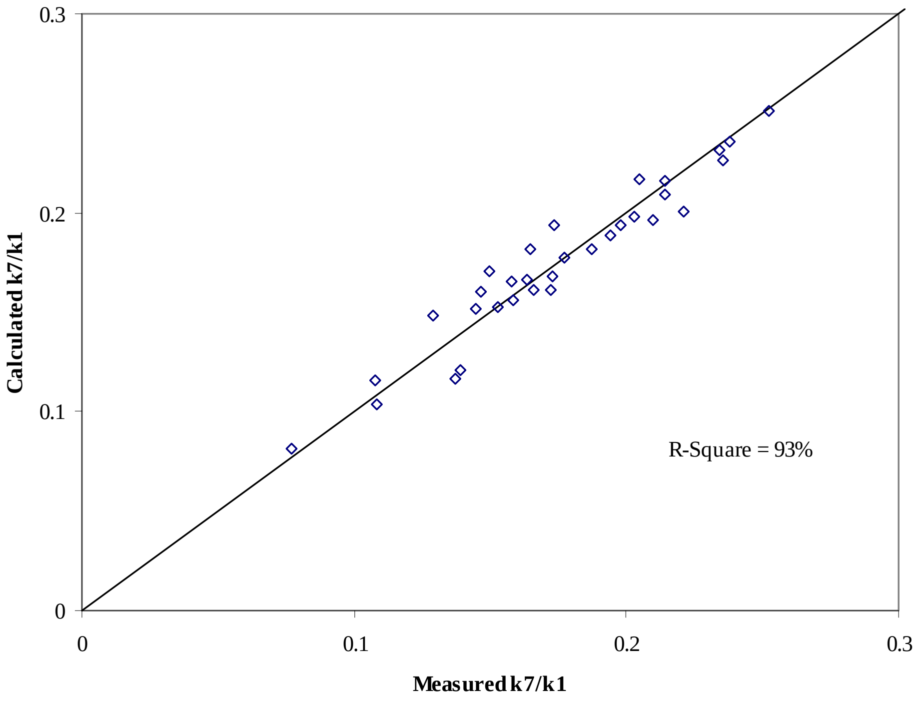

FIGURE 5.18. Comparison of Measured and Calculated k_7/ k_1

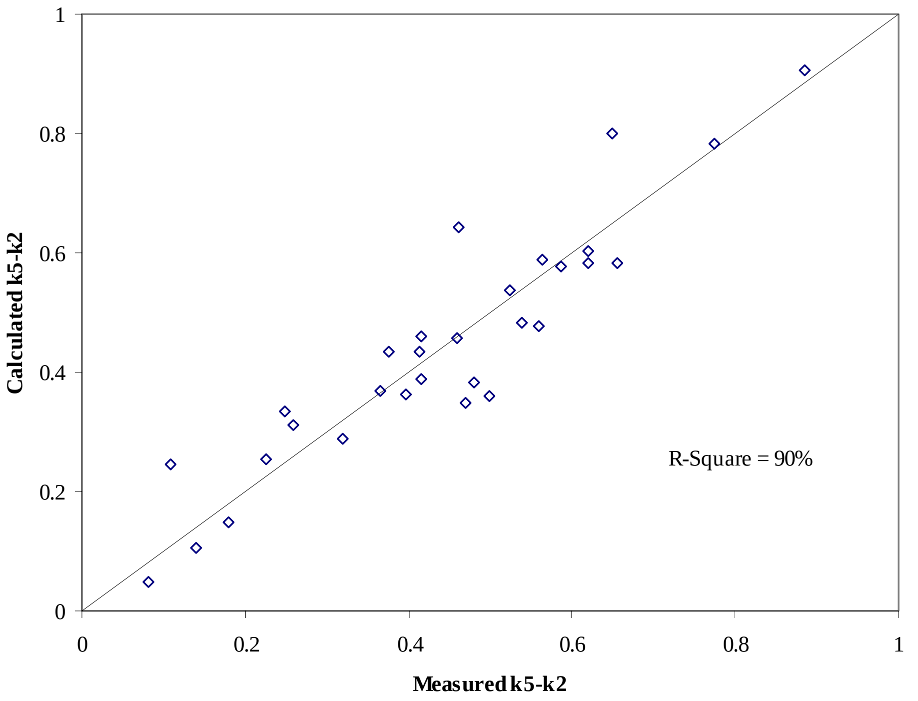

FIGURE 5.19. Comparison of Measured and Calculated $k_5- k_2$

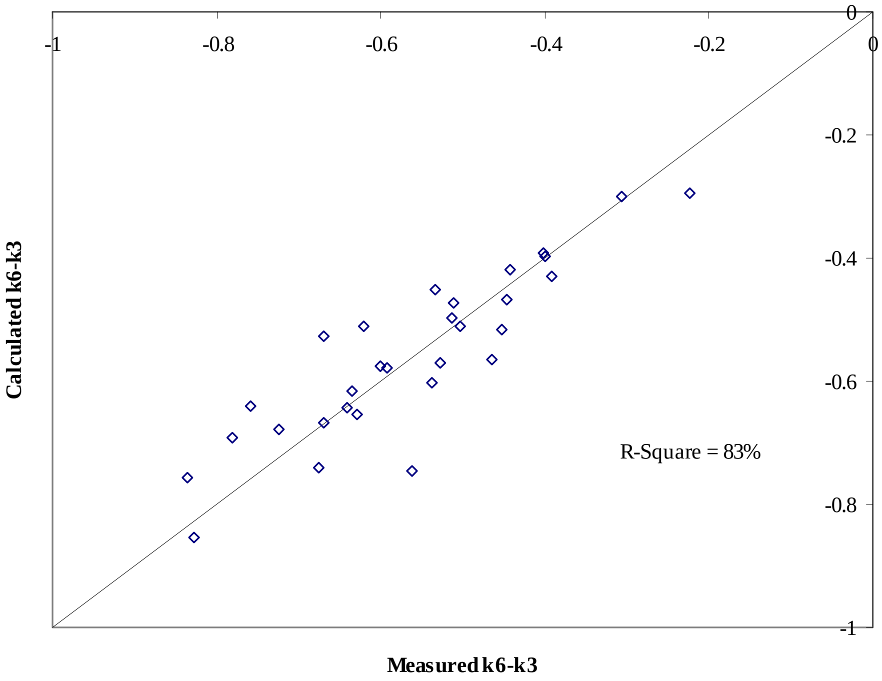

FIGURE 5.20. Comparison of Measured and Calculated k_6- k_3

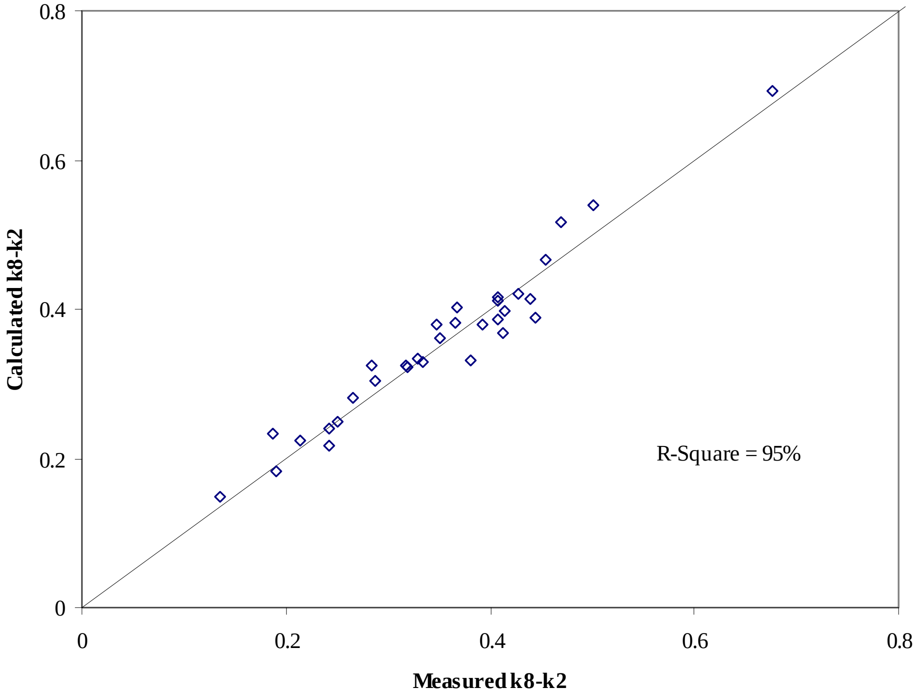

FIGURE 5.21. Comparison of Measured and Calculated k_8 - k_2

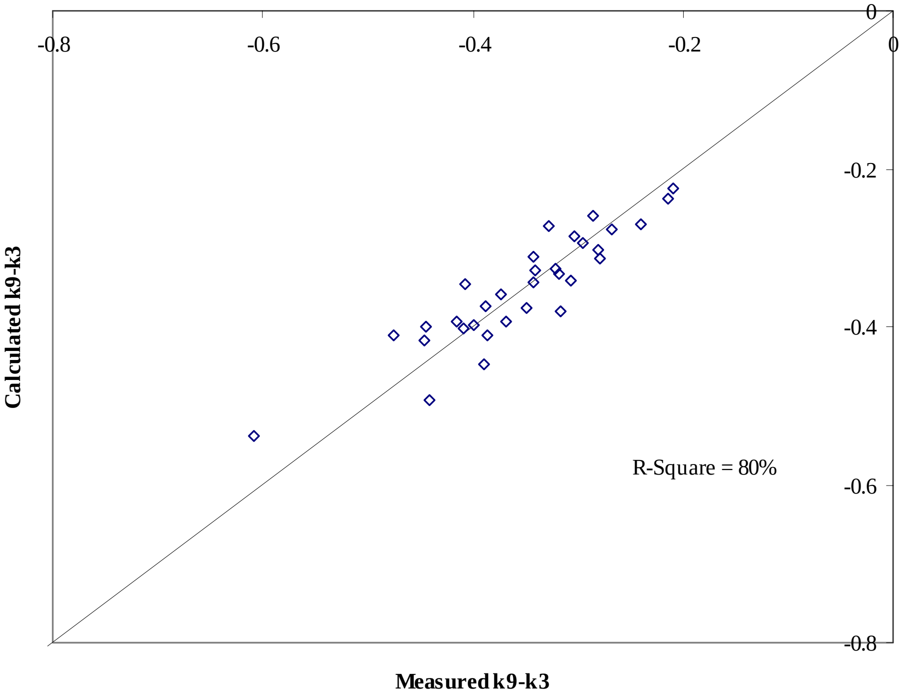

FIGURE 5.22. Comparison of Measured and Calculated $k_9 - k_3$

Comparisons of measured and predicted k4/k1 (horizontal modular ratio) and k7/k1 (shear modular ratio) are shown in Figure 5.23. Figure 5.23 shows that k7/k1 generally increases with increase of k4/k1. As shown in Figure 5.24 and 5.25, the relative influence of confinement and octahedral stresses on the horizontal modular ratio is evaluated through the exponents (k_5-k_2) and (k_6-k_3), while the influence of these stresses on the shear modular ratio is evaluated using the exponents (k_9-k_3) and (k_8-k_2). In general, the octahedral stress and confinement stress have opposite effects as evident in the opposite signs for the exponents. The octahedral shear stress has slightly higher effect on the horizontal modulus rather than the confinement stress. This is inferred from Figure 5.24 where (k_6-k_3) is slightly higher than (k_5-k_2). Both octahedral and confinement stresses have almost the same effect on the shear modular ratio as can be seen in Figure

5.25 where (k_9-k_3) and (k_8-k_2) are almost equal. In general, these results indicate that when the octahedral and confinement stresses have similar values under the applied wheel load, the constant ratio terms (k_4/k_1 or k_7/k_1) in the models play the governing role in determining the anisotropy level which is in agreement with the finding reported by Tutumluer and Thompson (5). The results showed that the typical ranges of horizontal modulus to vertical modulus ration varies between 10 % to 55 %, while the shear modulus to the vertical modulus is between 10 % and 25%.

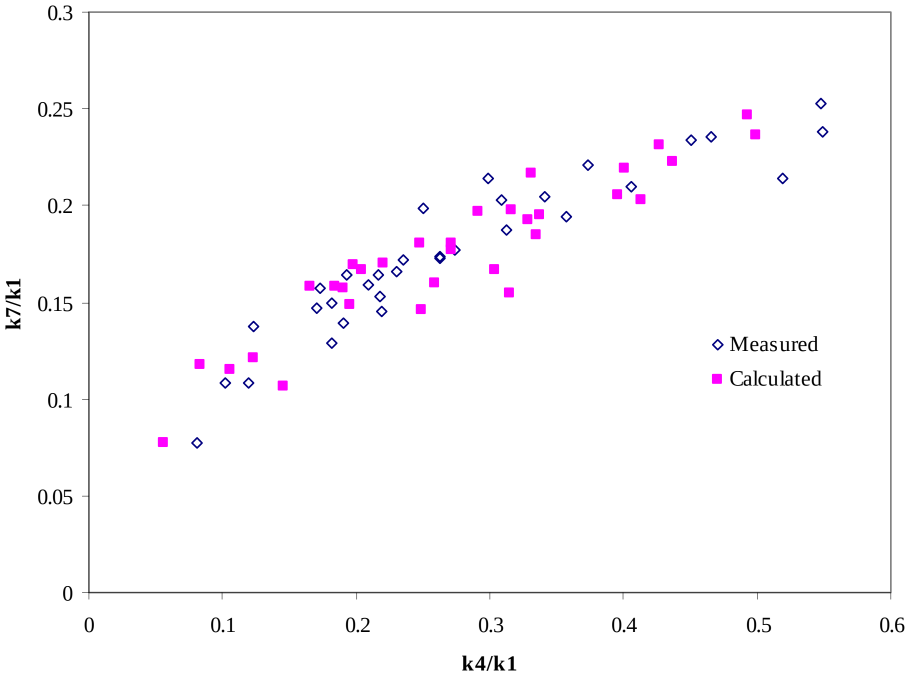

FIGURE 5.23. Variations of Measured and Calculated Constant Terms for Horizontal and Shear Modular Ratio

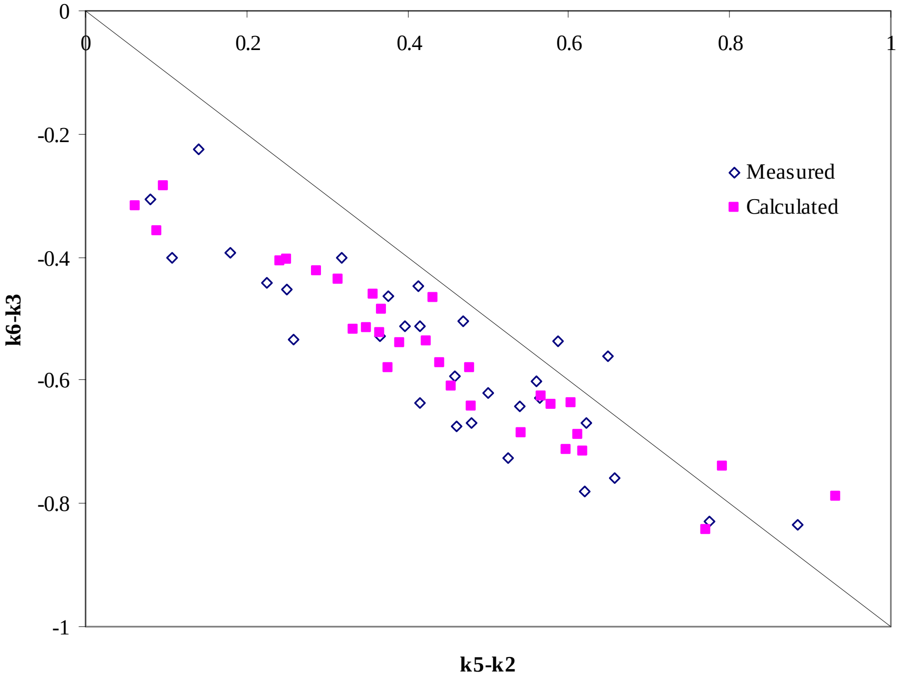

FIGURE 5.24. Comparisons of Bulk and Shear Stress Exponent Term for Horizontal Modular Ratio

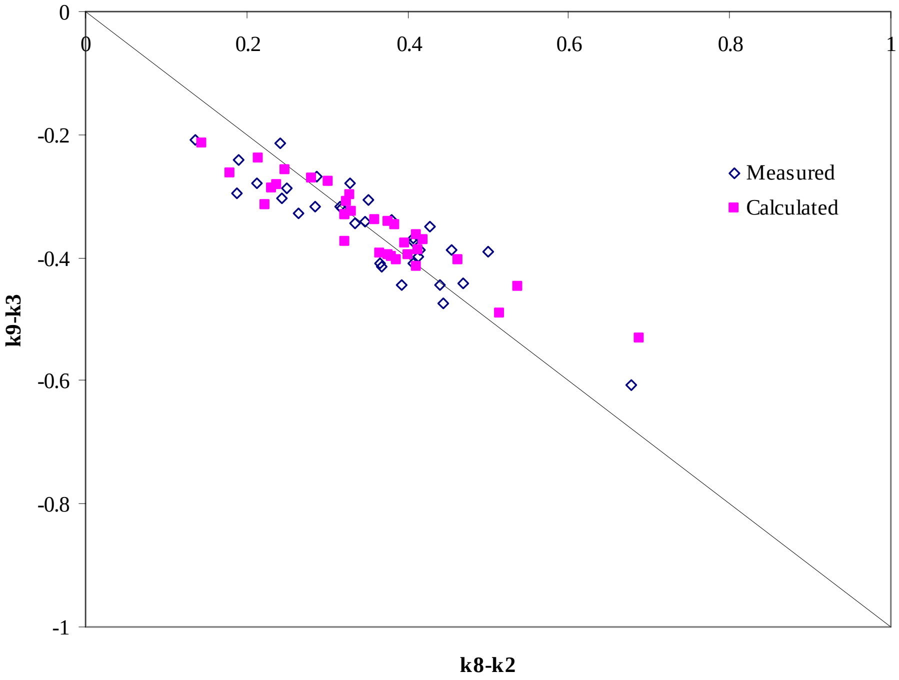

FIGURE 5.25. Comparisons of Bulk and Shear Stress Exponent Term for Shear Modular Ratio

CHAPTER VI

PAVEMENT ANALYSIS AND DISTRESS MODEL DEVELOPMENT

EFFECT OF CONSTITUTIVE MODEL ON PAVEMENT PERFORMANCE

Figure 6.1 shows the cross sections used for the pavement analysis. The thickness of HMA was 50 or 100 inches (2 or 4 mm) and the base course had 300-mm (12-in.). The thickness of subgrade was assumed as semi-infinite. To model the test sections, the wheel load was applied as a uniform pressure of 689 kPa (100 psi) over a circular area of radius 136-mm (5.35 in.). A fixed boundary was assumed at the bottom of the subgrade where the concrete slab was placed.

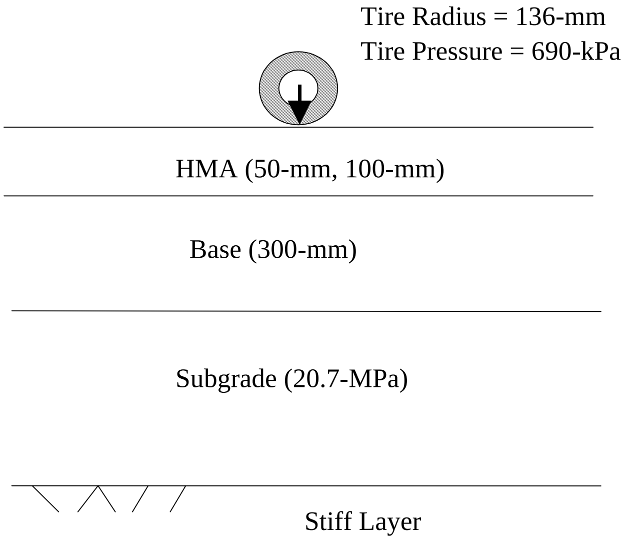

FIGURE 6.1 Cross Section for Pavement Analysis

The base material properties used in the analysis were obtained from a well graded aggregate #1 compacted at optimum moisture content. The HMA layer and subgrade were assumed to be nonlinear isotropic and Table 6.1 is a summary of material input properties for finite element program. Four constitutive models were used to represent the base layer, namely linear isotropic, nonlinear isotropic, linear cross-anisotropic and non-linear cross-anistropic in the finite element program.

Since the Uzan's nonlinear model (Equation 2.19) was implemented in TTI-PAVE implement, it can be downgraded to a linear elastic model by setting the material parameters, k_2, and k_3 as zero. The modular ratio (n, m) and ratio of Poisson's ratio in vertical and horizontal directions are inputted in the finite element program.

where,

$$n = \frac{E_x}{E_y}, \qquad (6.1)$$

$$n = \frac{G_{xy}}{E_y}, \text{ and} \qquad (6.2)$$

$$\mu = \frac{\nu_{xx}}{\nu_{xy}} \qquad (6.3)$$

A axisymmetric finite element mesh is shown in Figure 6.2. It was assumed that the nodal radial strains were negligible at approximately 10 times R (radius of loaded area) from the area of applied wheel load and the nodal stresses and displacements were assumed to be negligible at 20 times R below the pavement surface.

TABLE 6.1 Pavement Material Parameters

HMA Layer (Nonlinear Isotropic Model)			
k_1 = 28,000 k_2 = 0.100 k_3 = 0.001 n = 1.00 m = 0.38 ν_{xy} = 0.35 μ = 1.00			
Base Course			
Linear Isotropic	Non-Linear Isotropic	Linear Anisotropic	Non-Linear Cross-Anisotropic
k_1 = 4,000 k_2 =0.0, k_3=0.0 n =1.0, m=0.38 ν_{xy} =0.2, μ = 1.0	k_1=4,000 k_2=0.555, k_3=0.3 n=1.0, m=0.38 ν_{xy} =0.2, μ = 1.0	k_1=4,000 k_2=0.0, k_3=0.0 n=0.5, m=0.38 ν_{xy} =0.2, μ = 1.0	k_1=4,000 k_2=0.555, k_3=0.3 n=0.5, m=0.38 ν_{xy} =0.2, μ = 1.5
Sub-grade (Non-linear Isotropic Model)			
k1 = 207 k2 = 0.001 k3 = 0.300 n = 1.00 m = 0.38 ν_{xy} = 0.35 μ = 1.00			

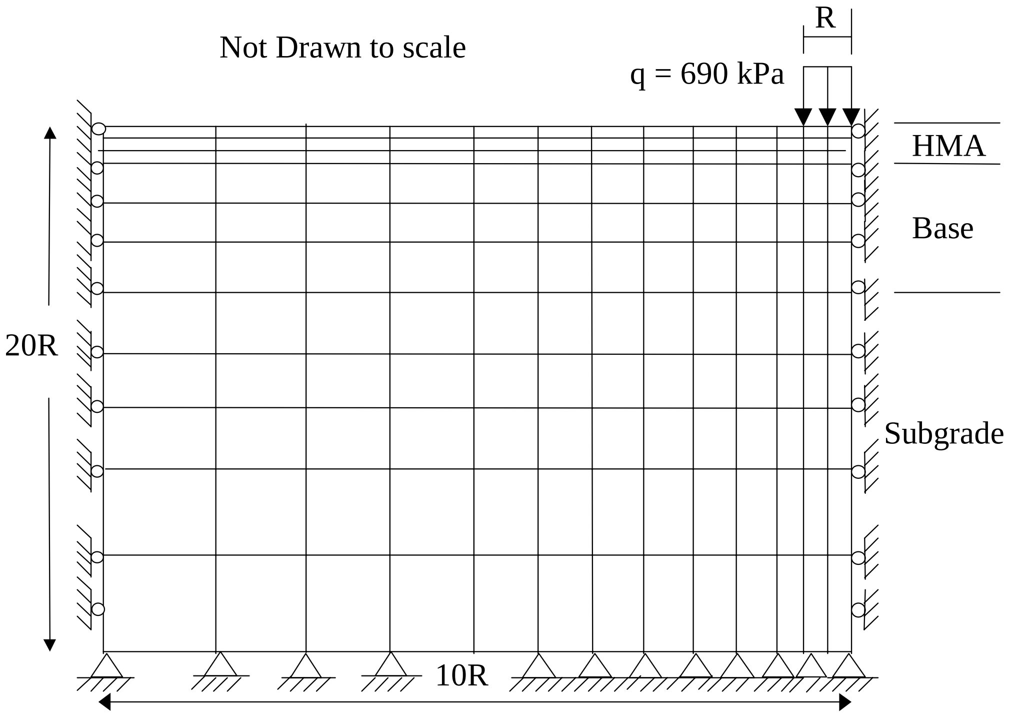

FIGURE 6.2 Finite Element Mesh

Figure 6.3 through 6.6 show the vertical and horizontal stress distribution in unbound aggregate base and significant differences occur among the constitutive models (i.e. tension is positive and compression is negative). The vertical stress distributions within the base layer do not have specific trend with respect to the constitutive models except the observation that linear anisotropic model generally gives lower vertical compressive stress. Pavement profiles and subgrade moduli rather than constitutive models have a significant effect on the vertical stress distributions (2). Modeling the unbound granular base layer as linear isotropic, nonlinear isotropic, linear anisotropic and nonlinear anisotropic in that order, gradually shifts the horizontal stresses from a tension to a compression. Also, increased HMA thickness for a given base layer thickness and subgrade modulus gives less magnitude of stresses in both horizontal and vertical directions.

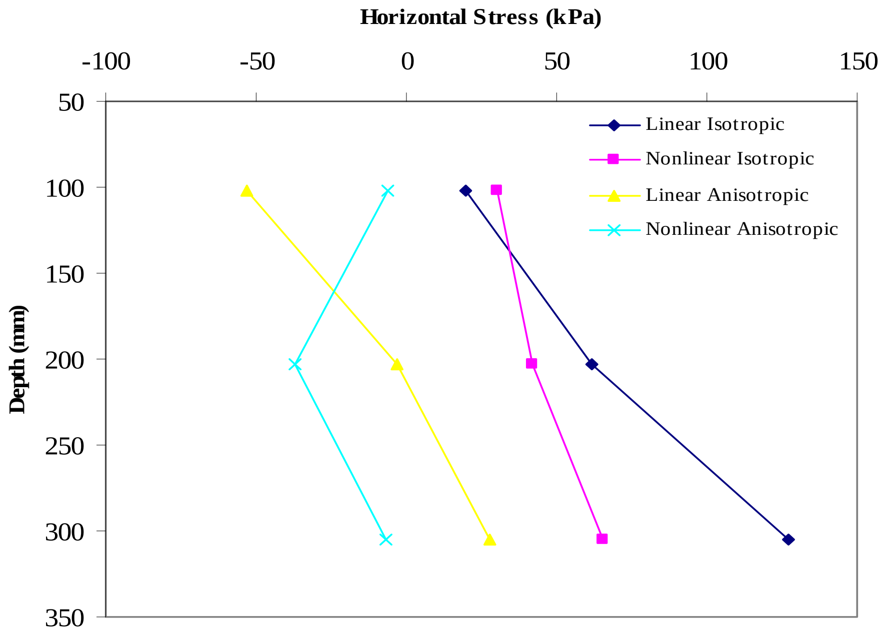

FIGURE 6.3 Horizontal Stress for 50mm HMA, 300mm Base and 20.7 MPa subgrade

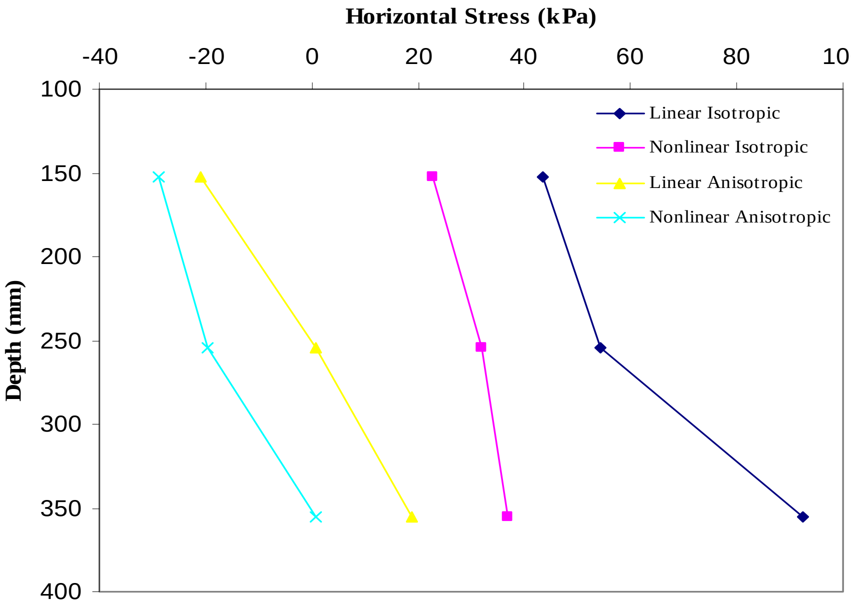

FIGURE 6.4 Horizontal Stress for 100mm HMA, 300mm Base and 20.7 MPa subgrade

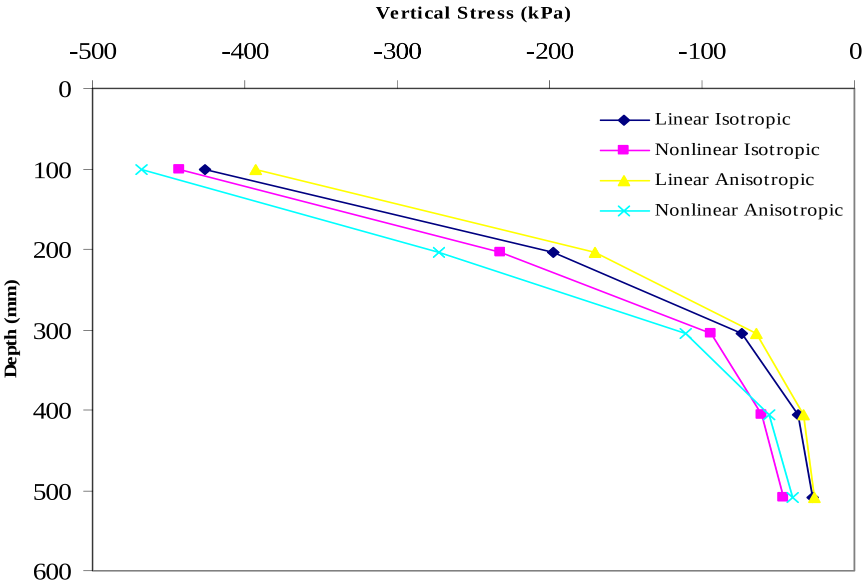

FIGURE 6.5 Vertical Stress for 50mm HMA, 300mm Base and 20.7 MPa subgrade

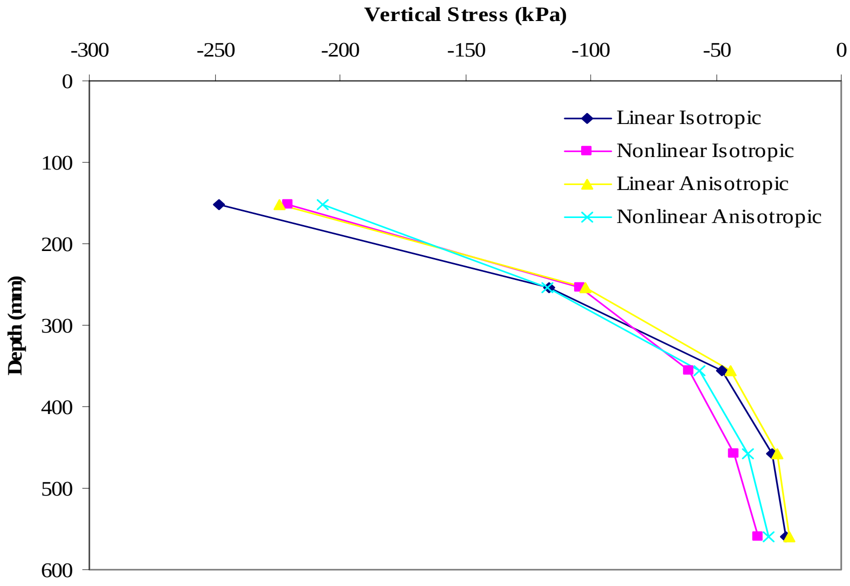

FIGURE 6.6 Vertical Stress for 100mm HMA, 300mm Base and 20.7 MPa subgrade

The nonlinear cross-anisotropic model gave much more realistic stress distribution as shown in the compressive horizontal stresses at the bottom of the base layer while the significant tensile stresses were computed using the other models. Thus, it would not be correct or desirable way to design pavement thicknesses by increasing the thickness of unbound aggregate base until the tensile stress that is obtained by linear isotropic model are diminished.

EFFECT OF GRADATION AND PARTICLE SHAPE ON PAVEMENT PERFORMANCE

A parametric study was conducted to demonstrate the influence of aggregate physical properties on the cross-anisotropic moduli and pavement response. It is not possible to hold some parameters constant and arbitrarily change others because the parameters are not totally independent. For example, fines content and gradation will have some effect on density and optimum moisture content. Furthermore, changes in these parameters can affect the vertical modulus (k_1 through k_3). The parametric study involved four different cases. The first case depicted aggregate #2 with well-aggregate gradation. Case 2 represented a coarse-graded aggregate #2, while case 3 and case 4 had the same parameters as the first case except for the form, angularity, and texture indices. The form parameters for case 3 were obtained from the aggregate # 4 which has more elongated particles. Thus, the form index in case 3 represented that aggregate mixture consists of more elongated aggregates than case 1. The angularity and texture parameters for case 4 were obtained from the aggregate #3, which has similar angularity and more rough texture.

Table 6.2 illustrates the effect of the physical parameters (gradation constants, g_a, g_n, and g_m, and aggregate shape indices) on k-ratios and modular ratios. Equation 5.3 was used to determine horizontal and shear constant terms based on the k_1 through k_3 values and the physical parameters. It can be seen that change in the physical properties had significant influence on the calculated modular ratios. From the comparison of case 1 and case 3, using more elongated particles has led to a lower value for k4/k1 indicating a higher level of anisotropy. Since the particle orientation occurs with maximum dimension aligned in horizontal direction, the number of contact for vertical direction are larger than the horizontal direction. This may result in the lower horizontal modulus and higher vertical modulus, which gives higher level of anisotropy. From the comparison of case 1 and case 2, higher values of horizontal and shear modular ratios (k4/k1 and k7/k1) were obtained for case 1. This indicates that well graded material exhibits less level of anisotropy than poor graded materials. Tutumluer and Thompson (5) also found that the level of anisotropy increases as the amount of fine material increases. From the comparison of case 1 and case 4, higher values of horizontal and shear modular ratios were observed when aggregates have similar angularity and more rough texture. From above observations, it can be ascertain that higher values of modular ratios, which support better load-carrying capacity are obtained when aggregate particles have well-gradation, less elongation, more angularity and, more rough texture.

The influence of the physical properties, and consequently, the cross-anisotropic moduli on pavement response was investigated using finite element analysis of a pavement section. The pavement section consisted of 4-inches of HMA (resilient modulus of 400,000 psi, Poisson's ratio of 0.35), 8-inches of unbound aggregate base over a subgrade with a resilient modulus of 3,000 psi, and a Poisson's ratio of 0.45. The model was subjected to a 9,000 pound wheel load. Two constitutive models were used to represent the base layer, namely linear isotropic and non-linear cross-anisotropic. The results of this analysis are shown in Table 6.3. It has been ascertained that the cross-anisotropy model gave more realistic stress distribution as shown in the compressive horizontal stresses at the bottom of the base layer rather than the significant tensile stresses computed using the other two isotropic models. Also, the change in the aggregate shape indices and gradation affected the stress distribution in the pavement section due to the change in the base layer anisotropy. When the nonlinear anisotropic model was used instead of the linear isotropic model for case 1, the horizontal strain at the bottom of HMA (ε_{tHMA}) and the vertical deviatoric stress at the top of subgrade (σ_v) increased by 51% and 46%, respectively. For the case 2 which represents poor-graded material, the percent increase of ε_{tHMA} and σ_v were 92% and 89%, respectively, when the nonlinear anisotropic model was used instead of the linear isotropic model. When more elongated particles were used such as case 3, the percent increases of ε_{tHMA} and σ_v were 72% and 46%, respectively, when the nonlinear anisotropic model was used instead of linear isotropic model. For the case 4, ε_{tHMA} and σ_v increased by 49% and 46% compared to linear isotropic case 1. These results demonstrate clearly that the aggregate physical properties such as gradation and shape influence the level of cross-anisotropy, which has a substantial effect on the stress distribution and pavement design.

TABLE 6.2. Calculated Material Coefficients of Aggregate #2 Varying the Gradation Parameters and Shape Index

	case1	case2	case3	case4
k1	6060	6060	6060	6060
k2	0.397	0.397	0.397	0.397
k3	0.204	0.204	0.204	0.204
k4/k1	0.456	0.365	0.203	0.485
k7/k1	0.226	0.209	0.222	0.240
k5-k2	0.049	0.150	0.266	0.036
k6-k3	-0.299	-0.392	-0.572	-0.376
k8-k2	0.183	0.209	0.140	0.154
k9-k3	-0.270	-0.286	-0.239	-0.285
ga	11.997	13.272	11.997	11.997
gn	1.544	2.416	1.544	1.544
fa	6.9398	6.9398	6.8045	6.9398
fn	7.5816	7.5816	6.5241	7.5816
Aa	622.1465	622.1465	622.1465	165.0481
Ta	229.6287	229.6287	229.6287	242.955
Tn	4.3603	4.3603	4.3603	7

TABLE 6.3. Predicted Stress/ Strain in the Pavement

	Model	Bottom AC		Bottom Base		Top Subgrade
		Vertical Strain (10^{-6})	Horizontal Strain (10^{-6})	Vertical Stress (psi)	Horizontal Stress (psi)	Vertical Stress (psi)
case 1	Linear Isotropy	-371	211	-4.5	22.3	-4.6
	Nonlinear Anisotropy	-583	319	-6.4	-1.9	-6.7
case 2	Nonlinear Anisotropy	-678	405	-10.1	-1.9	-8.7
case 3	Nonlinear Anisotropy	-636	363	-5.3	-1.0	-5.8
case 4	Nonlinear Anisotropy	-573	314	-6.4	-1.0	-6.7

Note: Negative for Compressive and Positive for Tensile

EFFECTS OF AGGREGATE TYPES AND LEVEL OF ANISOTROPY

Within a specific type of aggregate (mineralogy and classification) texture and aggregate shape significantly influence the isotropic and anisotropic resilient response of the granular material. Rough-textured and angular aggregates develop a stronger and stiffer mass by locking together while smooth-textured and rounded aggregate particles tend to slide past one another. Accordingly, rough-textured and angular aggregates have better load carrying capacity and a higher resilient modulus than smooth-textured and rounded aggregate particles. A granular material with high shear and horizontal resilient moduli would have a less tendency to spread in lateral direction under the loads and this material results in the higher value of modular ratio. Therefore, the higher modular ratios are expected to be found in the rough-textured and angular aggregates.

Figures 6.7 and 6.8 show the distribution of horizontal and shear modular ratios. The group of data points for each aggregate source are scattered in the lower, intermediate and high modular ratio areas, respectively. The lowest horizontal and shear modular ratios were observed for aggregate #3 and #4 while the highest horizontal and shear modular ratios were obtained for aggregate #1 and #2.

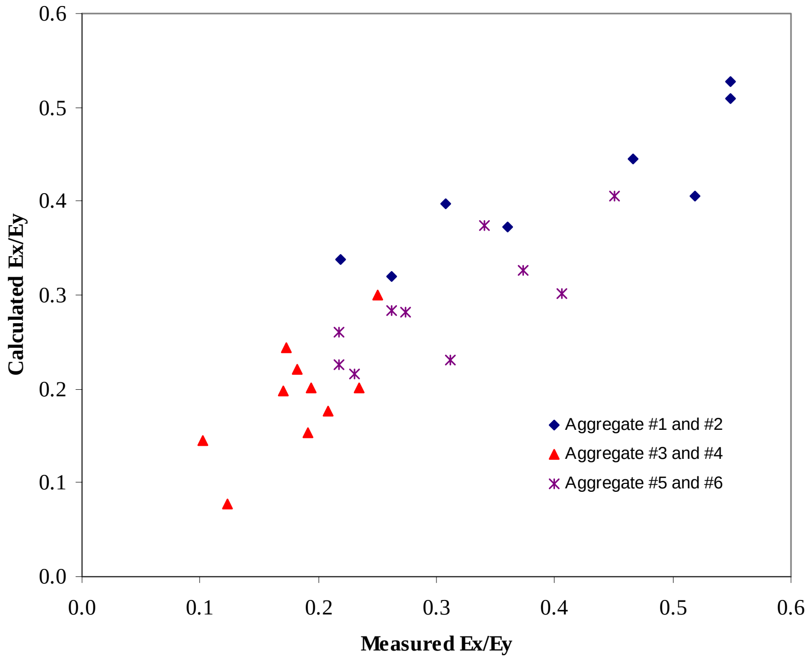

FIGURE 6.7. Distribution of Horizontal Modular Ratio with Different Aggregate Types

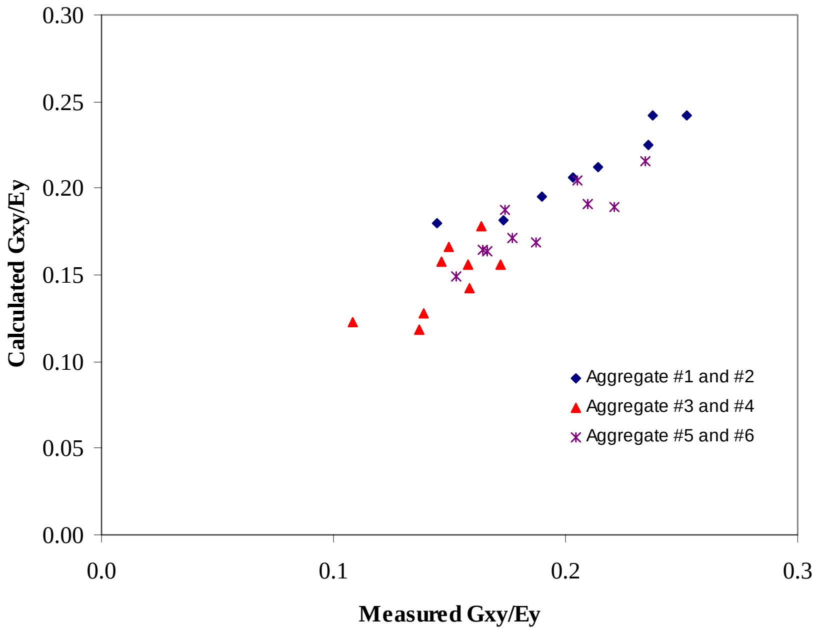

FIGURE 6.8. Distribution of Shear Modular Ratio with Different Aggregate Types

The vertical resilient modulus of aggregate #3 which gives lower horizontal modular ratio and that of aggregate #1 that has higher horizontal modular ratio were plotted along the stress states in Figure 6.9.

The resilient moduli for aggregate #1 and #3 were 350-MPa and 150-MPa at the bulk stress of 150 kPa. The influence of the aggregate sources, physical properties, and consequently, anisotropic level on pavement response was investigated using CIRCLY program. The pavement section consisted of 4-inches of HMA (resilient modulus of 2760-MPa, Poisson's ratio of 0.35), 12-inches of unbound aggregate base over a subgrade with a resilient modulus of 3,000 psi, and a Poisson's ratio of 0.45. The model was subjected to a 136-mm radius and 9,000 lbs wheel load. The results of this analysis are shown in Table 6.4. The tensile strain at the bottom of HMA and compressive strain at the top of subgrade were calculated and the allowable number of load repetitions for fatigue cracking and rutting were obtained based on the Asphalt Institute transfer functions. It was found that different aggregate physical properties, which result in different anisotropic level, substantially affect the pavement critical responses and ultimately, allowable number of load repetitions. These results clearly demonstrate that the aggregate physical properties such as grading and shape influence the level of cross-anisotropy, which has a substantial effect on the pavement responses and therefore, affects mechanistic-empirical pavement design.

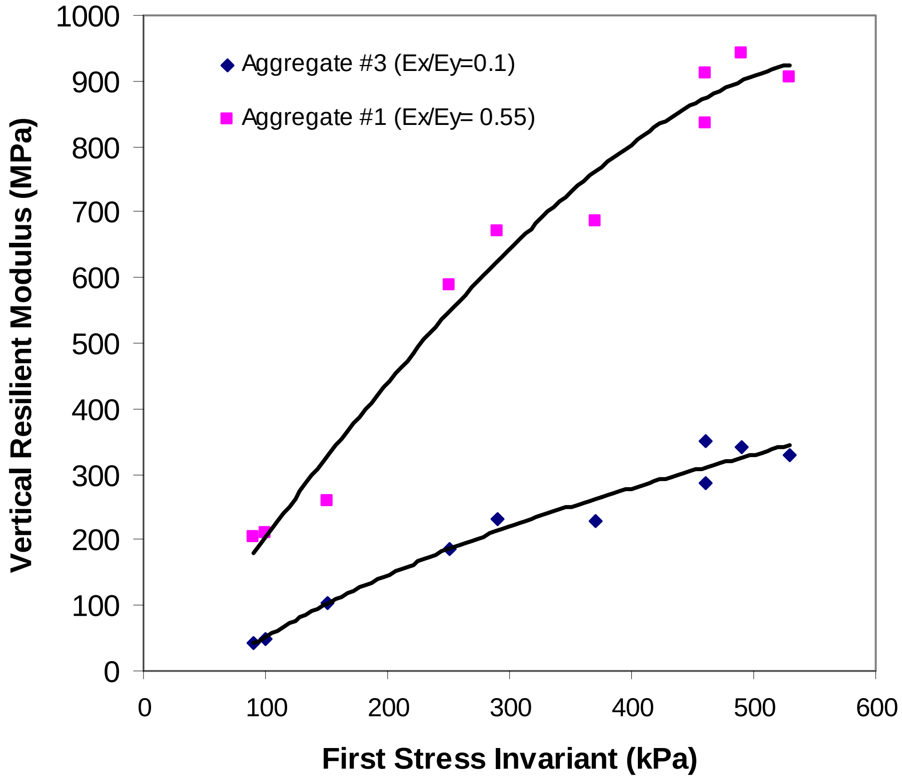

FIGURE 6.9. Distribution of Resilient Modulus Along First Stress Invariant

TABLE 6.4. Comparisons of Pavement Critical Responses for Different Aggregate Sources

Pavement Critical Responses	Resilient Modulus for Unbound Aggregate Base	
	Aggregate #1 (350 MPa)	Aggregate #5 (350 MPa)
Tensile Strain at the bottom of HMA(10^{-6})	267	437
Compressive Strain at the Top of Subgrade (10^{-6})	791	1176
Number of allowable load repetitions to cause fatigue cracking, Nf	753538	148912
Number of allowable load repetitions to limit rutting, Nd	105195	17820

Two different materials, which have similar resilient moduli along the stress state and different anisotropic levels were compared to investigate the significant effect of anisotropic behavior of granular material. The resilient modulus distributions of aggregate #5 and aggregate #1, compacted with different gradations and moisture contents were measured from the repeated load triaxial test. Figure 6.10 shows that the resilient moduli of those materials are reasonably same all over the stress states. Although gravel and limestone have the similar resilient modulus distribution along the stress state, they have different level of anisotropy. Table 6.5 shows the triaxial test results for horizontal, vertical, and shear resilient moduli and the level of anisotropy when the bulk stress is 170 kPa (25 psi).

TABLE 6.5. Measured Moduli and Level of Anisotropy

	Ey (psi)	Ex (psi)	Gxy (psi)	Ex/Ey	Gxy/Ey
Aggregate #5	25968	5476	3815	0.2	0.15
Aggregate #1	23088	8657	4351	0.4	0.20

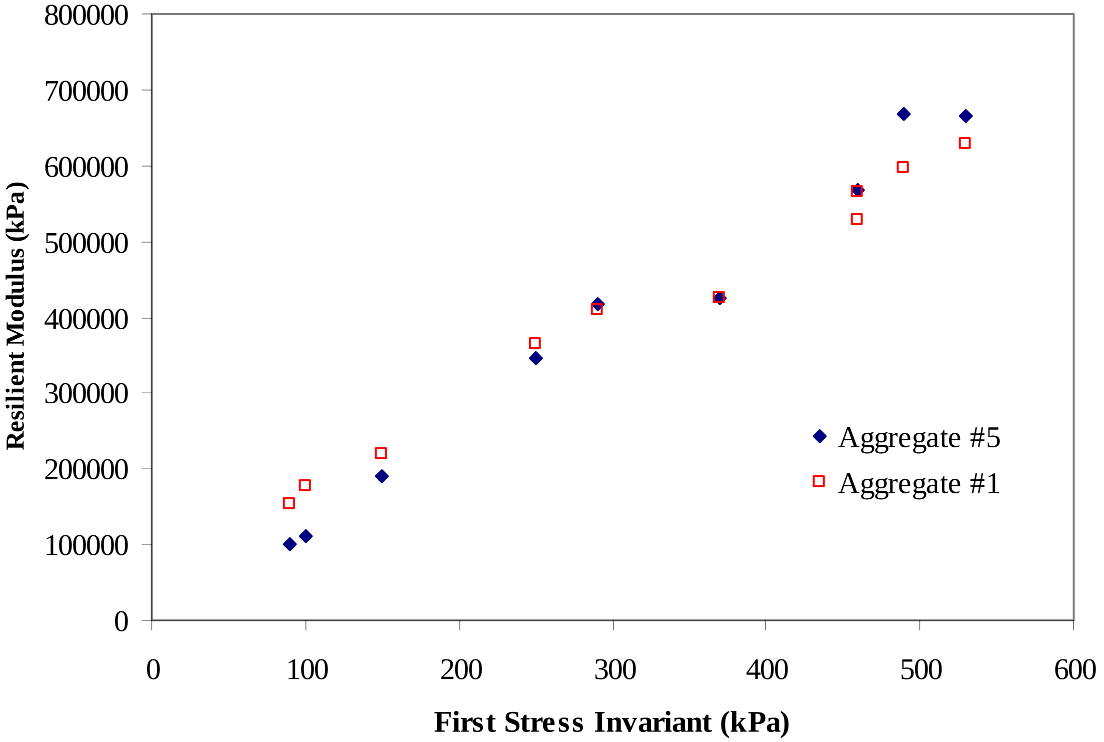

FIGURE 6.10. Sample Distribution of Resilient Moduli for Aggregates #1 and #5

The data in Table 6.5 were inputted in CIRCLY program and the pavement critical strains were calculated with nonlinear anisotropic model. The pavement section consisted of 4-inches of HMA (resilient modulus of 2760-MPa, Poisson's ratio of 0.35), 12-inches of unbound aggregate base over a subgrade with a resilient modulus of 3,000 psi, and a Poisson's ratio of 0.45. The model was subjected to a 136-mm radius and 9,000 lbs wheel load. Table 6.6 shows the calculated critical strains by TTIPAVE and the number of allowable load repetitions by AI equations. Although Aggregate #1 and #5 have similar vertical resilient moduli, the calculated critical strains for those materials are quite different due to the effect of the level of anisotropy. For aggregate #5 which has higher anisotropic level, the allowable load repetitions for fatigue cracking and rutting decreased 16% and 35 % than those for aggregate #1, which has lower anisotropic level. This results illustrates the anisotropic analysis must be considered in the pavement design to better estimate the pavement responses.

TABLE 6.6 Pavement Critical Strains and Allowable Load Repetitions

	Aggregate #5	Aggregate #1
Tensile Strain at the bottom of HMA (10^{-6})	640	608
Compressive Strain at the Top of Subgrade (10^{-6})	1753	1597
Number of allowable load repetitions to cause fatigue cracking	42424	50226
Number of allowable load repetitions to limit rutting	2983	4528

DISTRESS MODELS FOR ANISOTROPIC RESPONSES AND PAVEMENT DESIGN LIFE

In this section, design criteria and design charts have been made in terms of maximum allowable load repetitions and used as the indicator of selecting the thickness of unbound aggregate base. The design charts are based on multi-layered elastic anisotropic system in cylindrical coordinates under axial symmetry. The materials in each layer are characterized by a resilient modulus and Poisson's ratio and traffic is expressed as repetitions of an 18-kips single axial load. The single tire is approximated by one circular plates with radius = 152 mm (6 in.) corresponding to an 18-kips axle load and a 80 psi contact pressure.

The multi-layered elastic system assumes that the surface traffic loading produces two critical pavement responses which are horizontal tensile strain, ε_t, at the bottom of the HMA layer, and vertical compressive strain, ε_c, at the top of the subgrade layer as shown in Figure 6.11. Excessive horizontal strains at the bottom of the HMA layer result in the fatigue cracking while excess compressive strains at the top of subgrade layer result in the permanent deformation.

The empirical part of Mechanistic-Empirical (M-E) design is the pavement life equations, which is transfer function. The transfer functions (or distress models) relate the computed pavement responses to pavement performance as measured by the type, severity, and extent of distress (e.g., rutting, cracking, etc). The most commonly used transfer functions relate pavement life to asphalt flexural strains (fatigue cracking) and to subgrade stresses and deflections (rutting).

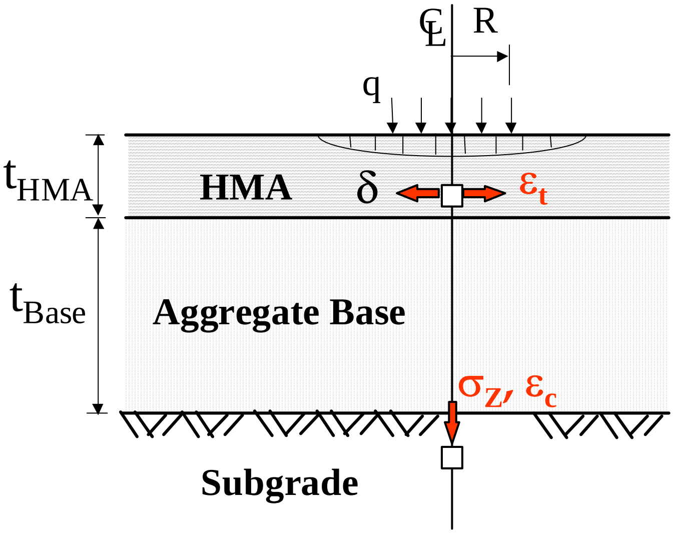

FIGURE 6.11. Critical Pavement Responses of Conventional Flexible Pavement

The transfer function determines the allowable number of load applications before the pavement failure and the amount of damage done to the pavement can be expressed as the ratio of applied (n_{ij}) to allowable (N_{ij}) loads. NCHRP 1-26 researchers concluded that the transfer functions are the weak links in the mechanistic-empirical design approach. To match predicted and observed pavement distress and performance, extensive field calibration and verification are often required to establish reliable distress prediction models (71). This will have to be done locally to account for differences in material properties and climate that are not explicitly modeled.

Typical fatigue algorithms are of the form

$$N_f = f_1 \left(\frac{1}{\varepsilon_t} \right)^{f_2} \left(\frac{1}{E_{mix}} \right)^{f_3} \tag{6.4}$$

Where,

N_f = allowable number of 80 kN equivalent single axle load (ESAL) applications based on fatigue cracking,

E_{mix} = stiffness of the asphalt concrete mix in psi.,

f_1, f_2 and f_3 = fitting coefficients, and

ε_t = predicted tensile strain at the bottom of the asphalt surface layer

The rutting algorithms are of the form:

$$N_d = f_4 \left(\frac{1}{\varepsilon_c} \right)^{f_5} \tag{6.5}$$

Where,

N_d = allowable number of 80 kN equivalent single axle load (ESAL) applications based on rutting,

f_4 and f_5 = fitting coefficients, and

ε_c = predicted compressive strain at the top of subgrade

As previously mentioned, the stress distributions predicted by nonlinear cross-anisotropic finite element program are realistic by eliminating excessive tensile stress at the bottom of the base layer and critical pavement responses predicted by nonlinear cross-anisotropic model are higher than those predicted by linear or nonlinear isotropic models. Because the previously developed transfer functions (Asphalt Institute, Chevron, and Nottingham models, etc.) were based on the critical responses obtained from linear isotropic model, those equations are not appropriate for responses obtained from nonlinear cross-anisotropic model. Therefore, the development of usable transfer functions for nonlinear cross-anisotropic model is ever more important.

For the transfer function development AASHO Road Test data were used. Fatigue and rutting characteristics of the flexible pavement are represented by the equation:

$$N_f = 8.148 \times 10^{-6} \varepsilon_t^{-3.376} E_{mix}^{-0.199} \quad \text{(R-square: 72 \%)} \qquad (6.6)$$

$$N_d = 1.5 \times 10^{-8} \varepsilon_c^{-4.35} \quad \text{(R-square: 84 \%)} \qquad (6.7)$$

Where,

N_f = allowable number of 80 kN equivalent single axle load (ESAL) applications based on fatigue cracking,

N_d = allowable number of 80 kN equivalent single axle load (ESAL) applications based on rutting,

ε_t = predicted tensile strain at the bottom of the asphalt surface layer, and

ε_c = predicted compressive strain at the top of the subgrade

Equation (6.6) and (6.7) show that reduced strain corresponds to increased pavement life. Once the allowable and applied numbers of load applications are obtained, Miner's hypothesis is used to obtain the accumulating damage. When damage exceeds 1, the pavement thicknesses need to be increased while the pavement thicknesses need to be decreased when damage is much less than 1. When damage is near, but not exceeding 1, a desirable pavement design can be obtained.

$$\boldsymbol{D} = \sum_{\boldsymbol{j}=1}^{\boldsymbol{n}} \sum_{\boldsymbol{i}=1}^{\boldsymbol{m}} \frac{\boldsymbol{n_{ij}}}{\boldsymbol{N_{ij}}} = 1 \qquad (6.8)$$

where,

nij = expected number of load applications

Nij = predicted number of load applications

m = number of axle load intervals, and

n = number of seasons or time periods.

The CIRCLY program was used to determine the thickness of required unbound aggregate base layer based on both fatigue cracking and rutting criteria. Material properties for HMA and subgrade layer were shown in Table 6.7. The resilient modulus for unbound aggregate base were 30,000, 50,000, and 80,000 psi for vertical direction and the 50% and 40% of the vertical resilient modulus was assigned for horizontal modulus and shear modulus, separately. Figure 6.12 through 6.23 are the design charts for given material properties.

TABLE 6.7. Pavement Material Parameters

	Modulus (psi)	Poisson's ratio
HMA	400,000	0.3
UAB	30,000 / 50,000 / 80,000	0.4
Subgrade	3,000 / 7,500 / 15,000	0.45

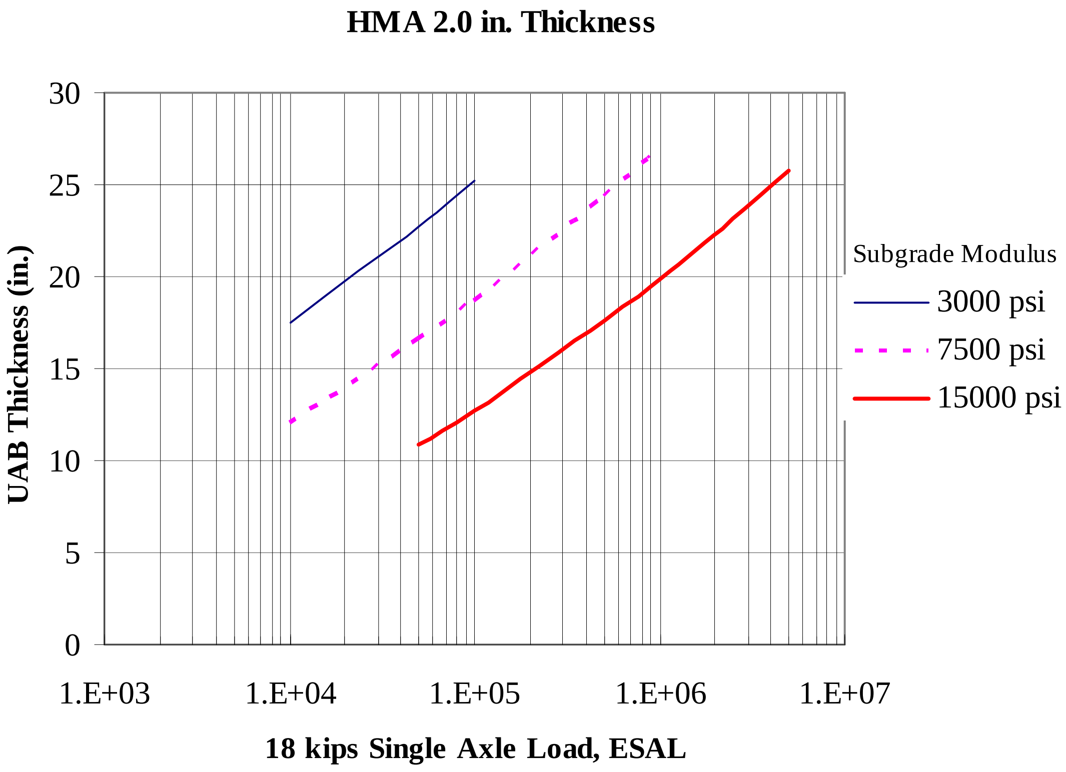

FIGURE 6.12. Design Chart for UAB with HMA 2-in (UAB Modulus = 30,000 psi)
(1 psi=6.9 kPa, 1 in. = 25.4 mm)

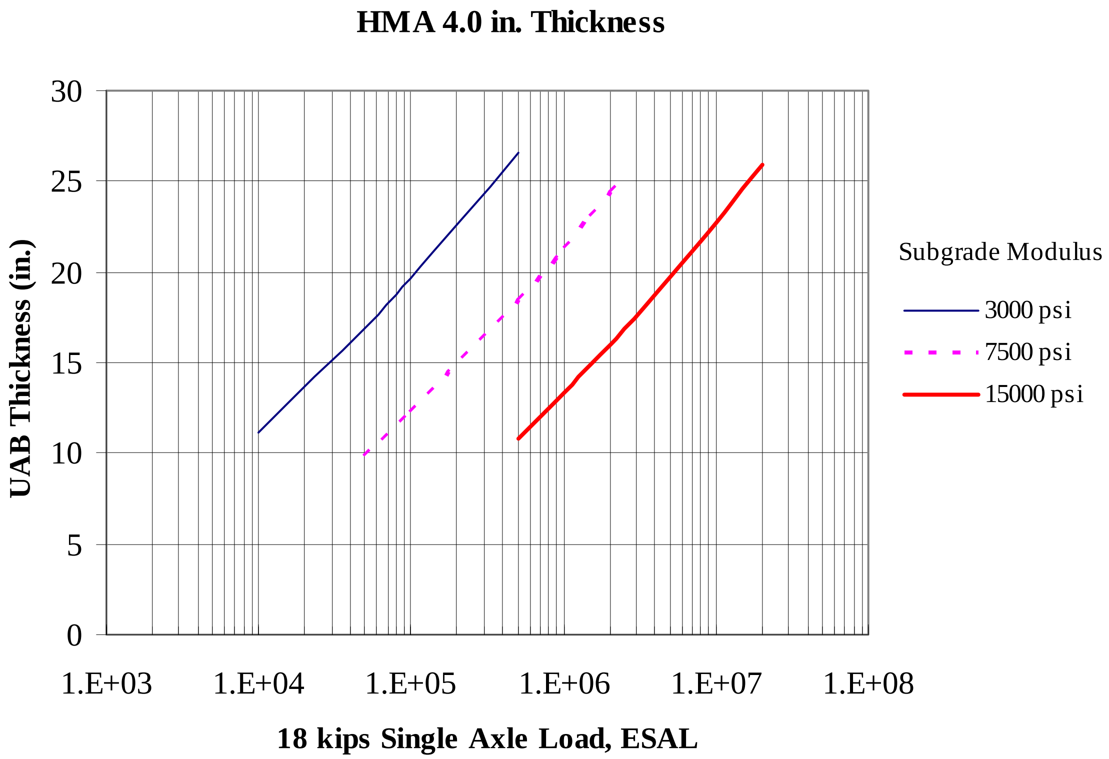

FIGURE 6.13. Design Chart for UAB with HMA 4-in. (UAB Modulus = 30,000 psi) (1 psi=6.9 kPa, 1 in. = 25.4 mm)

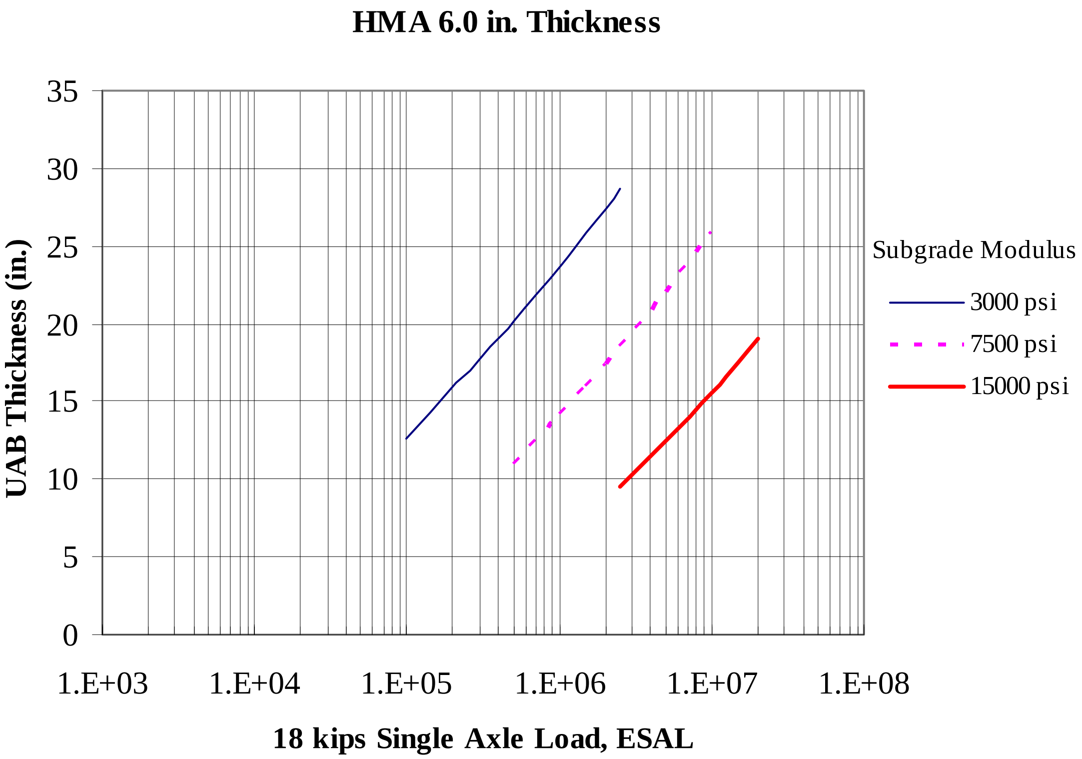

FIGURE 6.14. Design Chart for UAB with HMA 6-in (UAB Modulus = 30,000 psi) (1 psi=6.9 kPa, 1 in. = 25.4 mm)

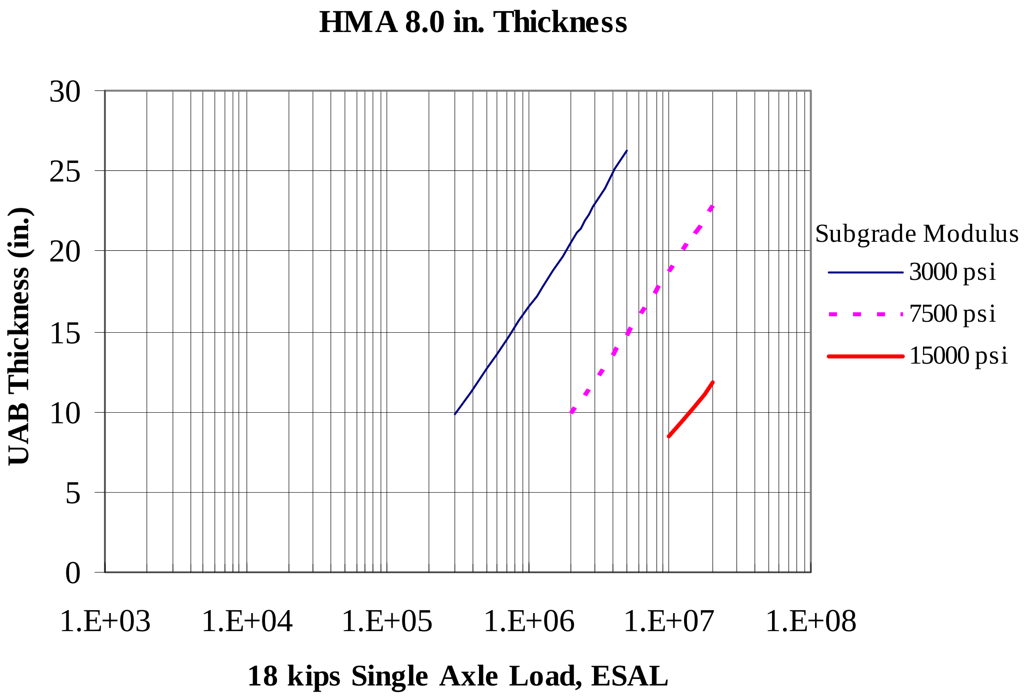

FIGURE 6.15. Design Chart for UAB with HMA 8-in. (UAB Modulus = 30,000 psi) (1 psi=6.9 kPa, 1 in. = 25.4 mm)

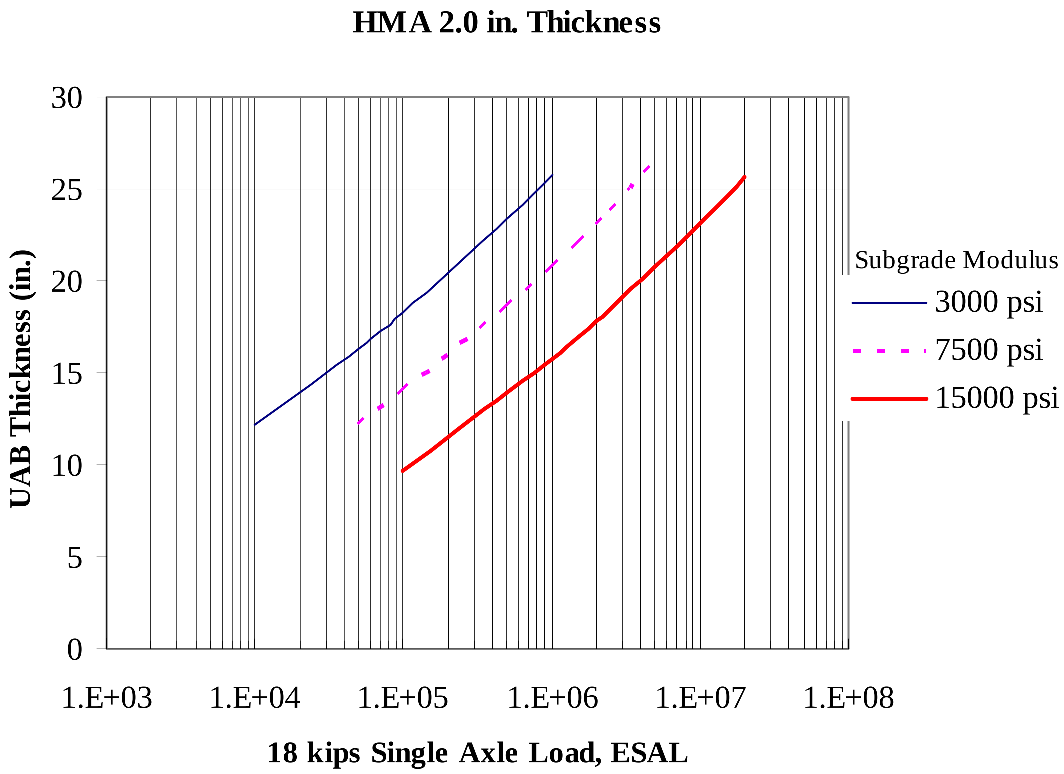

FIGURE 6.16. Design Chart for UAB with HMA 2-in. (UAB Modulus = 50,000 psi) (1 psi=6.9 kPa, 1 in. = 25.4 mm)

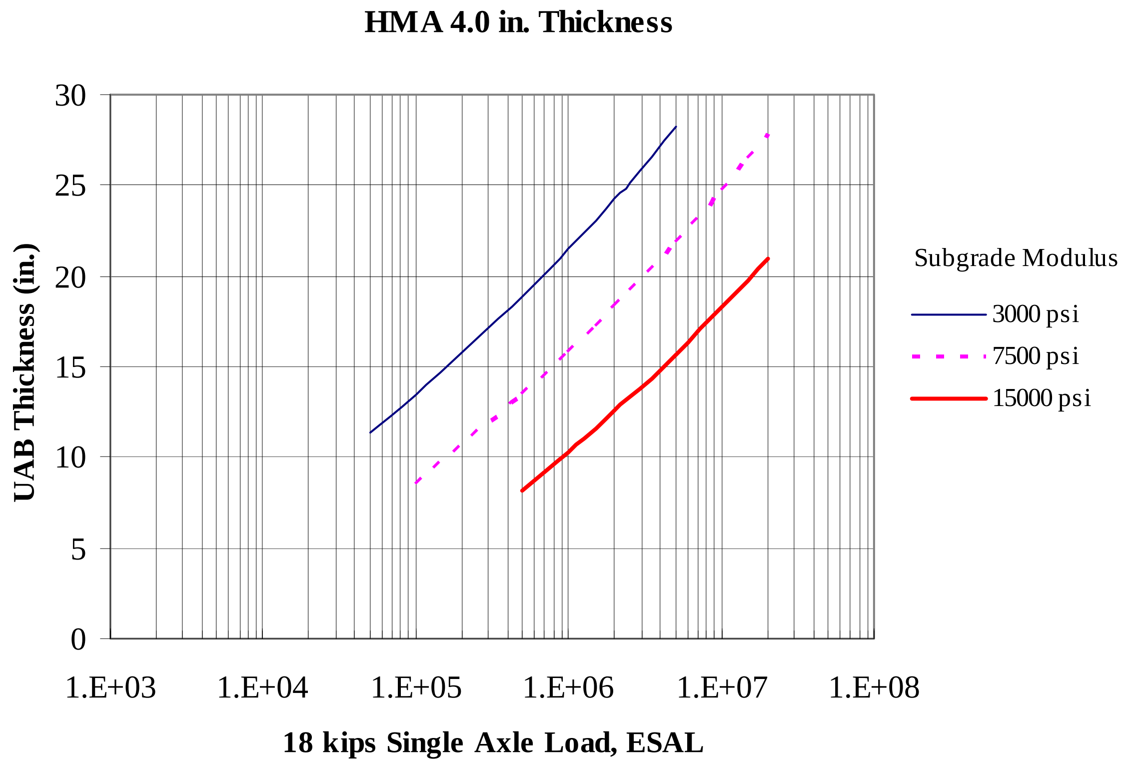

FIGURE 6.17. Design Chart for UAB with HMA 4-in. (UAB Modulus = 50,000 psi) (1 psi=6.9 kPa, 1 in. = 25.4 mm)

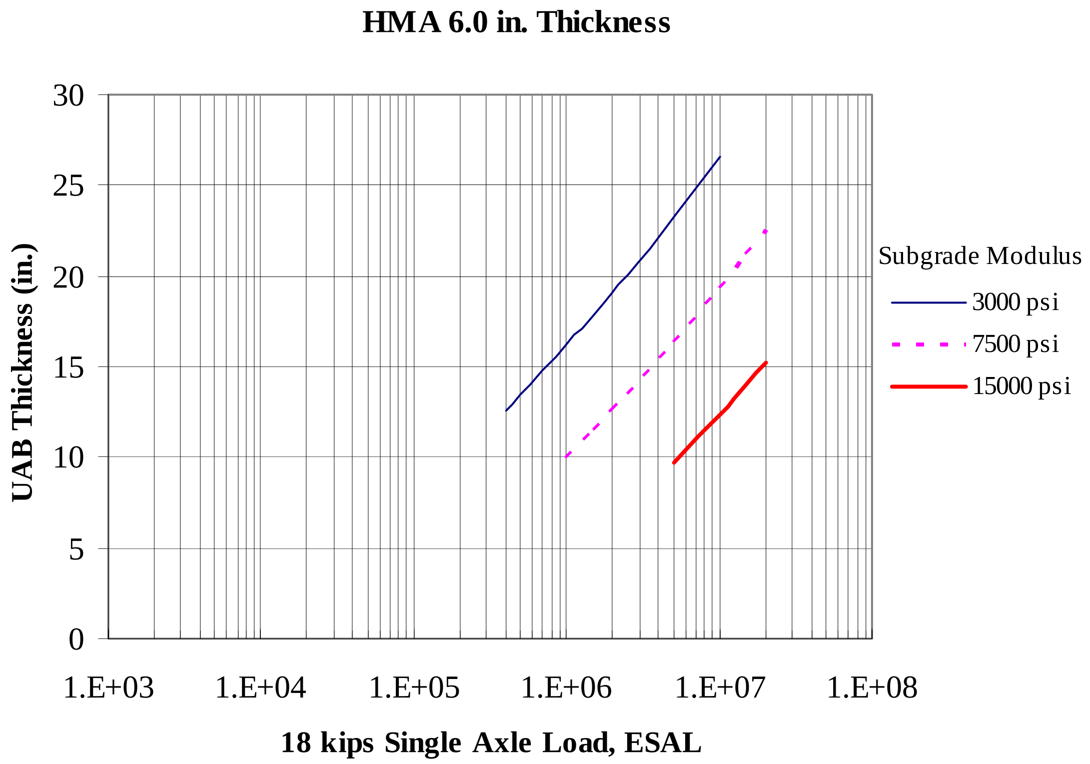

FIGURE 6.18. Design Chart for UAB with HMA 6-in. (UAB Modulus = 50,000 psi) (1 psi=6.9 kPa, 1 in. = 25.4 mm)

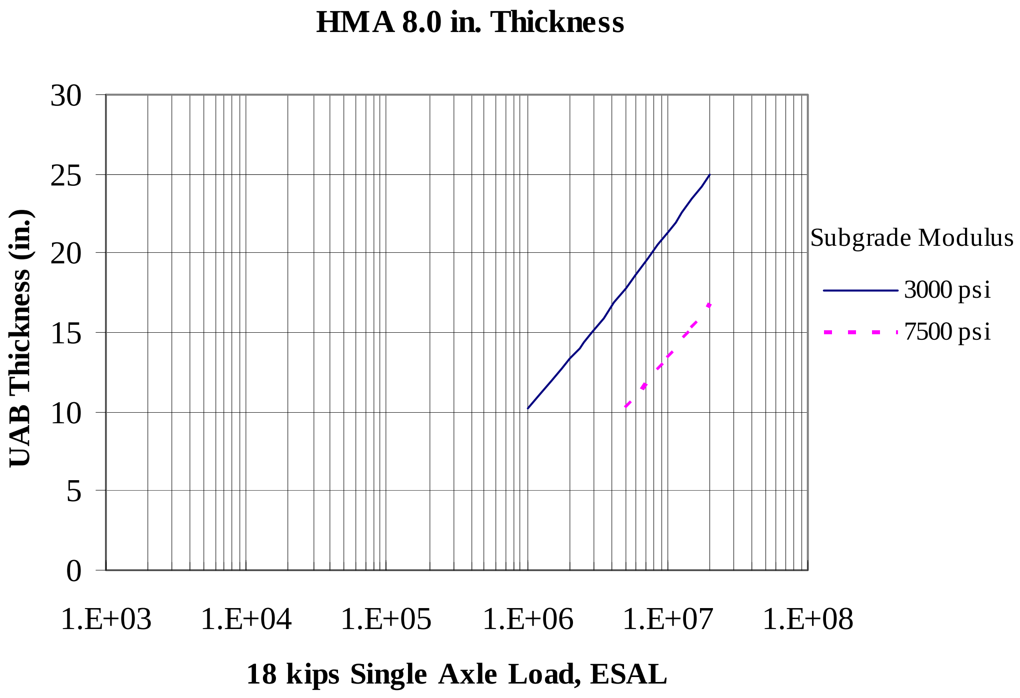

FIGURE 6.19. Design Chart for UAB with HMA 8-in. (UAB Modulus = 50,000 psi) (1 psi=6.9 kPa, 1 in. = 25.4 mm)

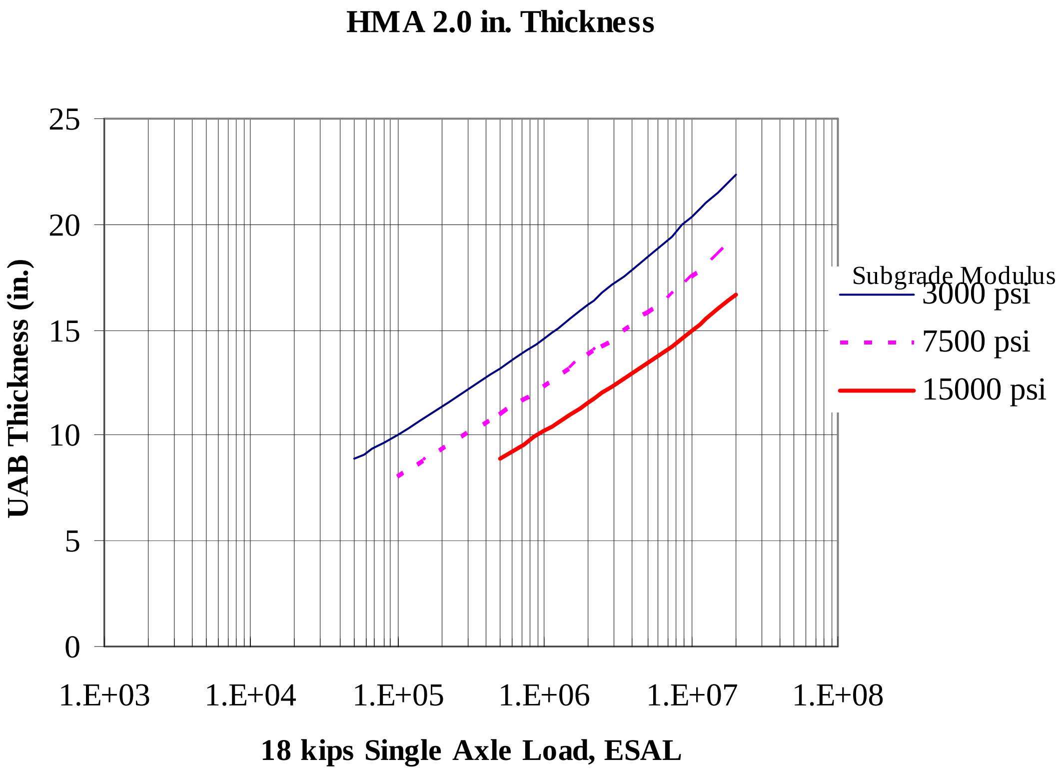

FIGURE 6.20. Design Chart for UAB with HMA 2-in. (UAB Modulus = 80,000 psi)
(1 psi=6.9 kPa, 1 in. = 25.4 mm)

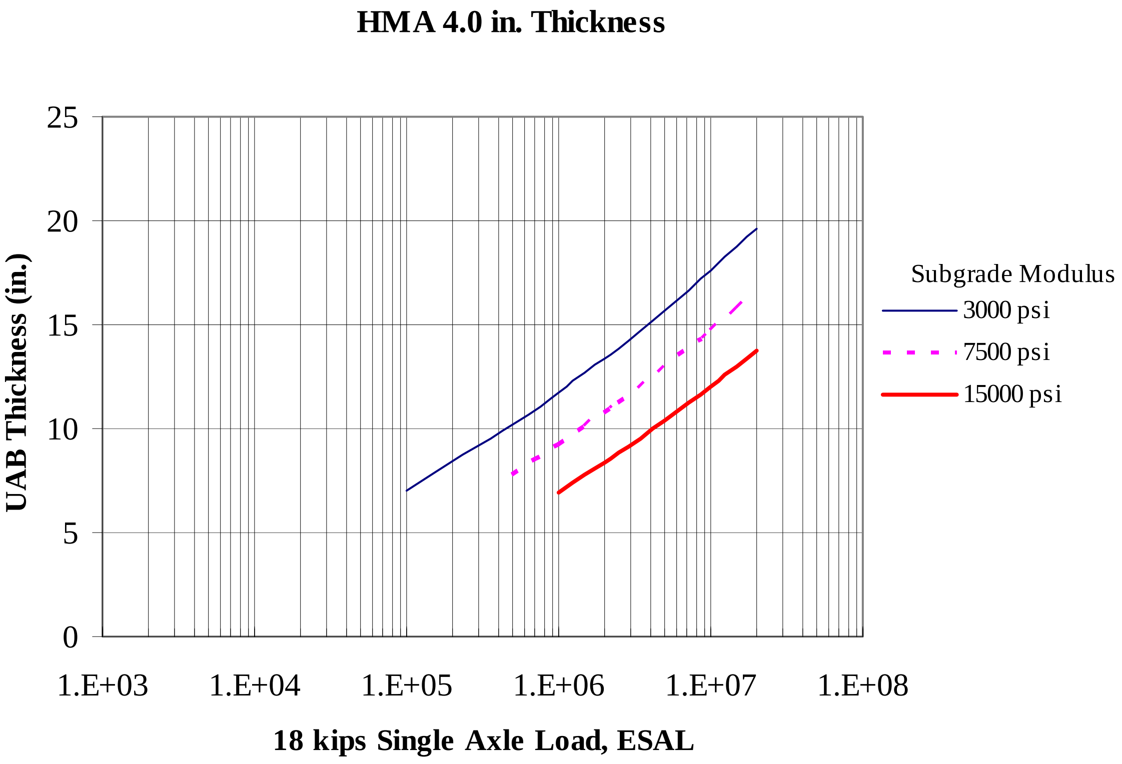

FIGURE 6.21. Design Chart for UAB with HMA 4-in. (UAB Modulus = 80,000 psi) (1 psi=6.9 kPa, 1 in. = 25.4 mm)

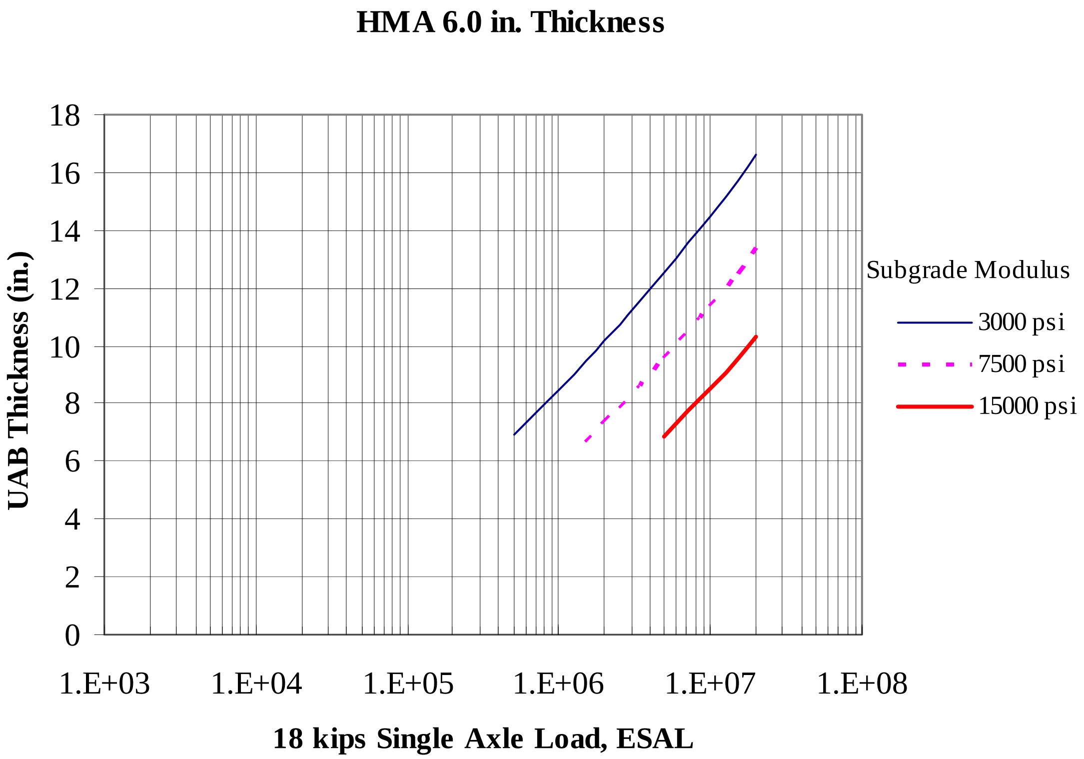

FIGURE 6.22. Design Chart for UAB with HMA 6-in. (UAB Modulus = 80,000 psi) (1 psi=6.9 kPa, 1 in. = 25.4 mm)

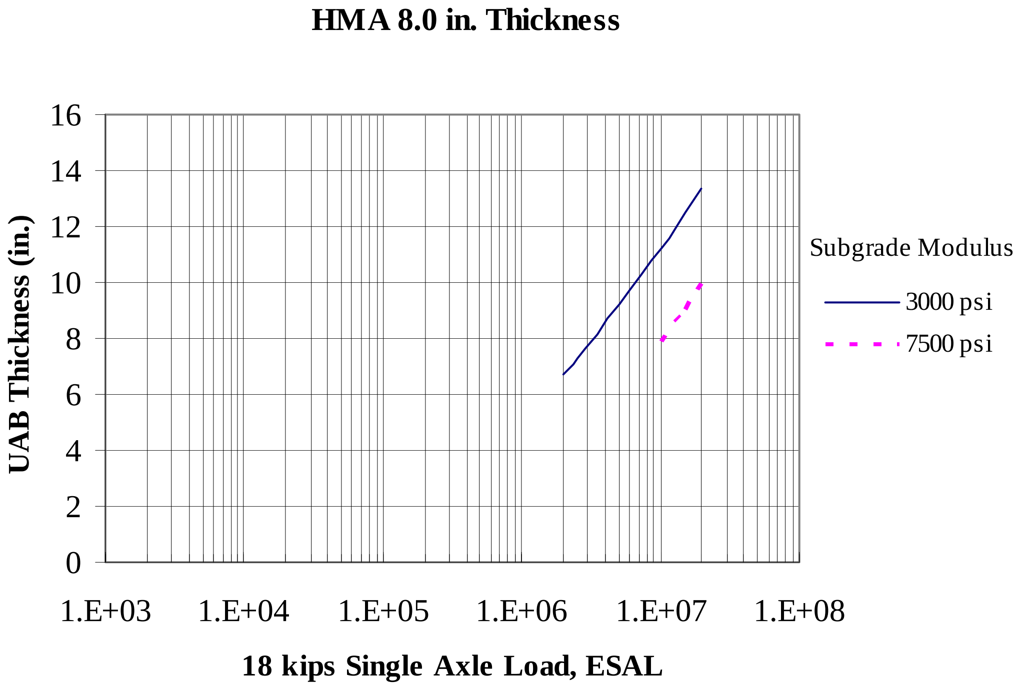

FIGURE 6.23. Design Chart for UAB with HMA 8-in. (UAB Modulus = 80,000 psi) (1 psi=6.9 kPa, 1 in. = 25.4 mm)

The minimum recommended aggregate base thickness is 4 inches when the traffics are less than 500,000. If the traffics are more than 500,000, the minimum 6 inches thickness is recommended. Although aggregate layers less than 4 inches thick are possible, it is not recommended because of following reasons:

- The base layer thickness less than 4 inches doesn't give much strength to the overall pavement structure
- Difficult to compact and construct
- Fines from the underlying subgrade may contaminate a substantial portion of the layer and inhibit drainage.

DESIGN AND EVALUATION EXAMPLES

The design case studies for 3,000 psi subgrade are developed with ICAR design method and compared with AASHTO and AI methods in Table 6.8.

TABLE 6.8. Comparison of Thickness Design of Various Design Methods

Design Method	UAB Resilient Modulus (psi)	HMA thickness (in.)	UAB thickness (in.)
AASHTO	30000	5	31.4
AI	Not Applicable		
ICAR	30000	5	30.5
	50000	5	22
	80000	5	12

Given subgrade modulus of 3,000 psi, ESAL = $2*10^6$, and an unbound aggregate base of 30,000 psi, AASHTO design guide determines the thicknesses of HMA and UAB as 5 and 31.4 inches, respectively. Asphalt Institute method is not applicable because the maximum base thickness is 18 inches. In ICAR design method, several combinations of thickness designs are determined as following: (4 in HMA, 33.5 in UAB) / (6 in HMA, 27.5 in UAB). In ICAR method, 2 inches thinner HMA layer makes average 6 inches thicker UAB. Compared with the thickness design by AASHTO method, ICAR method produces 5 in HMA and 30.5 in UAB thickness, which is approximately 1-inch reduced UAB thickness in AASHTO thickness design.

The high quality unbound granular material, which has less elongation, more angularity, and rough texture has better ability to spread a surface loading and higher resilient modulus. The increase of resilient modulus of granular material affects the pavement thickness design (72-77). Table 4 shows the comparison of thickness design when the resilient modulus of unbound granular base is varied in ICAR method. It is observed that the 60% increase of UAB resilient modulus generates the 45% decrease of unbound aggregate base thickness.

CHAPTER VII

VERIFICATION STUDY

A parametric study was conducted to demonstrate the influence of level of anisotropy on the resilient modulus and pavement response through measurements made in the Georgia Tech Test sections with back-calculations. The effect of the granular material physical parameters on k-values in Uzan model and modular ratios were investigated in this chapter. The influence of the physical properties, and consequently, the cross-anisotropic moduli on pavement response was investigated using the finite element program of certain pavement section by varying the pavement profiles and input material properties. Four constitutive models were used to represent the base layer, namely linear isotropic, non-linear isotropic, linear cross-anisotropic, and non-linear cross-anistropic. Horizontal and shear modulus were calculated from the simplified procedure in chapter III that uses AASHTO T307-99 resilient modulus test results.

GEORGIA TECH TEST SECTIONS

Georgia Tech pavement test sections were constructed with installation of pressure cells and bison type strain coils instruments for measuring the load-induced pavement behavior (4). Pavement test sections consisted of two inverted sections, five conventional sections having crushed stone bases, and five full-depth asphalt concrete sections. Table 7.1 shows geometry, performance, and resilient response summary of conventional pavement test sections from the total pavement test sections. 6,500-lbs uniform circular load with 9.1 inches diameters was applied to the test sections to test a rutting or fatigue failure. Table 7.2 describes the aggregate gradations and material properties used in the test sections. Unbound aggregate consisted of crushed granitic gneiss obtained from the Norcross Quarry of Vulcan Materials Co. and prepared by blending 20 percent by weight of No. 5 size aggregate, 25 percent of No. 57, and 55 percent of No. 810 stone sizes. The gradation parameters were calculated from Table 7.2 and the ga, gm, and gn were 15.342, 0.892, and 2.328, respectively with 98% R-square. Figure 7.1 indicates how good the predictions fit with used gradation.

TABLE 7.1 The Geometry, Performance, and Resilient Response Summary of Conventional Pavement Test Sections (6)

Geometry and Performance					
Sec. No.	HMA Thickness (in.)	UAB Thickness (in.)	Repetitions to Failure	Failure Mode	Comments
8	3.5	8.0	550,000	Rutting	
9	3.5	8.0	2,400,000	Fatigue	Permanent Deformation: 0.28 in.
10	3.5	8.0	2,900,000	Fatigue	Permanent Deformation: 0.34 in.

Resilient Response										
Sec. No.	Horizontal Tensile Strain (10^{-6})		Vertical Stress (psi)		Vertical Strain (10^{-6})				Surface Deflection (in.)	
	Bottom AC	Bottom Base	Top Base	Top Subgrade	AC	Top Base	Bottom Base	Top Subgrade	10” from Centerline	14.5” from Centerline
8	300	375	-	11.9	-	560	110	1850	0.02	0.013
9	280	1080	62	11.1	-	560	340	1750	0.022	0.013
10	400	1025	54	6.8	-	620	400	2500	0.017	0.01

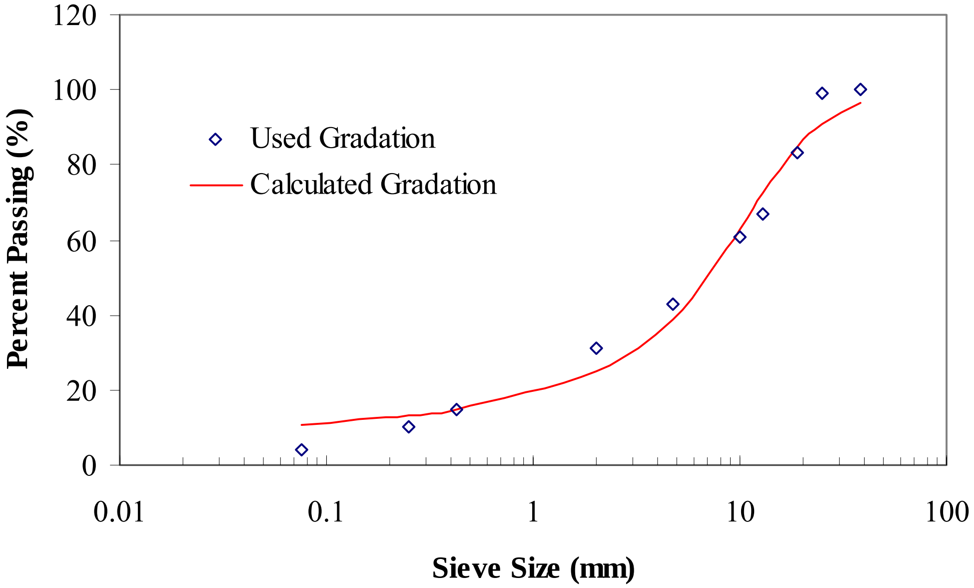

FIGURE 7.1 Used and Calculated Gradation

TABLE 7.2 Aggregate Gradations and Material Properties Used in Flexible Pavement Test Sections (21)

SIEVES	Cumulative % Passing By Weight										Maximum Density (pcf)	Opt. Water Content (%)
	1.5 in. (38 mm)	1 in. (25 mm)	3/4 in. (19 mm)	1/2 in. (13 mm)	3/8 in. (10 mm)	No. 4 (4.75 mm)	No. 10 (2.00 mm)	No.40 (.425 mm)	No. 60 (0.25 mm)	No. 200 (.075 mm)		
AC Aggregate Gradation:(2)	100	100	100	86	75	51	36	18	14	7	147	-
Base Aggregate Gradations:												
No. 5	100	96	37	5	2	-	-	-	-	-	-	-
No. 57	100	98	82	43	20	3	-	-	-	-	-	-
No. 810	100	100	100	100	100	77	56	27	19	8	-	-
Combined	100	99	83	67	61	43	31	15	10	4	137 (5)	5.7
Subgrade Gradation:(3)	100	100	100	100	100	100	99	85	70	39	105 (4)	18.5
CEMENT STABILIZED SUBBASE PROPERTIES : A. Soil - Cement Subbase: 5% by weight of Type I Portland cement added to the silty sand subgrade. (Section 11) Average 28-day unconfined compressive strength = 214 psi.											107 (5)	18.0
B. Aggregate - Cement Subbase: 4.5% by weight of Type I Portland cement added to the Combined base. (Section 12) Average 28-day unconfined compressive strength = 1146 psi.											138 (5)	6.0

Notes:
1. 1 in. = 25.4 mm; 1 psi = 6.895 kPa; 1 lb = 4.448 kN; 1 pcf = 0.157 kN/m^3
2. The B-binder AC had a 5.2% optimum asphalt content, 4 % voids in the total mix, Marshall mix stability of 2300 lb. (10.2 kN), and a flow value of 9.0/100.0 in. (2.3 mm).
3. Maximum aggregate size = 1.5 in. (38 mm)
4. Determined by AASHTO T-99 test method
5. Determined by AASHTO T-180 test method

Laboratory testing of the aggregate samples was conducted at the University of Illinois following TAASHTO T 307-99 (6). Preliminary test to obtain the maximum dry density and optimum moisture content were conducted and 2,302 kg/m3 and 4.7 % were obtained for maximum dry density and optimum moisture content, respectively. Table 7.3 summarizes the resilient modulus test results and the Poisson's ratios of the conventional pavement test sections. Aggregate form index parameters which are fa, fm, and fn were measured as 2.36, 3.8, and 4.2, respectively. Calculated material coefficients for horizontal and shear resilient modulus by simplified procedure in Chapter III. It was obtained that the horizontal and shear modular ratios were 0.6 and 0.17, respectively. Table 7.4 summarizes the material properties input properties of the finite element program.

TABLE 7.3 Predicted Material Properties from AASHTO T-307-99

Test Type	Parameters for Ey			Parameters for Ex			Parameters for G_{xy}			Level of Anisotropy
	K1	K2	K3	K4	K5	K6	K7	K8	K9	
AASHTO T307-99 (6”×12” specimen)	6607	0.5	-0.08	3048	0.25	-0.1	1248	0.7	-0.2	Ex/Ey = 0.6 Gxy/Ey = 0.17 $\nu_{xx}/\nu_{xy} = 1.5$

Note: 1 psi = 6.895 kPa

TABLE 7.4 Pavement Material Input Properties for Georgia Tech Pavement Test Section

<table>
<tr><th colspan="4">HMA Layer (Nonlinear Isotropic Model)</th></tr>
<tr><td colspan="4">k_1 = 250,000 k_2 = 0.100 k_3 = 0.001 n = 1.00 m = 0.38 ν_{xy} = 0.35 μ = 1.00</td></tr>
<tr><th colspan="4">Base Course</th></tr>
<tr><th>Linear Isotropic</th><th>Non-Linear Isotropic</th><th>Linear Anisotropic</th><th>Non-Linear Cross-Anisotropic</th></tr>
<tr><td>k_1 = 6,607
k_2 =0.0, k_3=0.0
n =1.0, m=0.38
ν_{xy} =0.2, μ = 1.5</td><td>k_1=6,607
k_2=0.0.498, k_3= -0.079
n=1.0, m=0.38
ν_{xy} =0.2, μ = 1.5</td><td>k_1 = 6,607
k_2 =0.0, k_3=0.0
n=0.6, m=0.17
ν_{xy} =0.2, μ = 1.5</td><td>k_1=6,607
k_2=0.0.498, k_3= -0.079
n=0.6, m=0.17
ν_{xy} =0.2, μ = 1.5</td></tr>
<tr><th colspan="4">Sub-grade (Non-linear Isotropic Model)</th></tr>
<tr><td colspan="4">k1 = 345 k2 = 0.001 k3 = -0.300
n = 1.00 m = 0.38 ν_{xy} = 0.35 μ = 1.00</td></tr>
</table>

MODELING OF PAVEMENT TEST SECTIONS

Table 7.3 was used for input of nonlinear finite element program, TTI-PAVE. Figure 7.2 shows the cross sections used for the pavement analysis. The thickness of HMA was 3.5 inches (89 mm) and the base course had 8 inches (203-mm). The thickness of subgrade was assumed as semi-infinite. To model the test sections, the wheel load was applied as a uniform pressure of 689 kPa (100 psi) over a circular area of radius 231-mm (9.1 in.).

The HMA layer and subgrade were assumed to be nonlinear. Two constitutive models were used to represent the base layer, namely linear isotropic and non-linear cross-anistropic in the finite element program. Table 7.5 shows comparisons of predicted and measured critical pavement responses. The critical responses of vertical strain/stress on the subgrade, and radial strain at the bottom of HMA layer match well the measured responses when nonlinear anisotropic model was used. The NCHRP research team for project 1-37A has selected a layered elastic model of the pavement to be used in the proposed 2002 AASHTO Pavement Design Guide. This fact alone emphasizes the importance of being able to assess anisotropic effects using elastic layered systems instead of using solution methodologies based on finite element analysis.

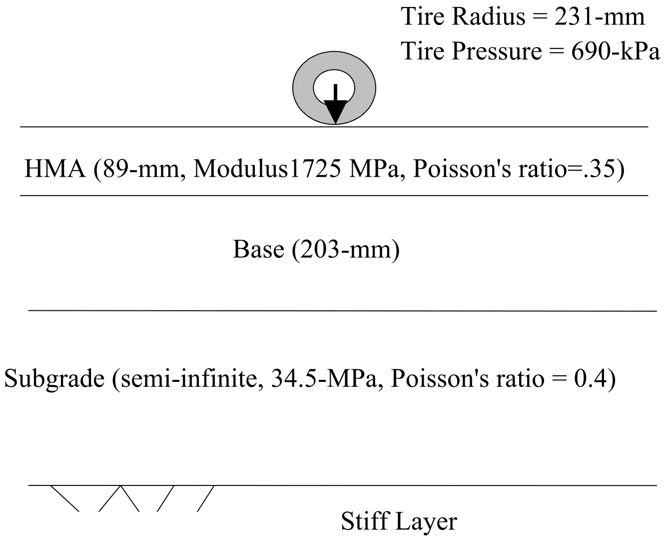

FIGURE 7.2 Cross Section for Pavement Analysis

TABLE 7.5 Comparisons of TTI-PAVE Predictions and Measured Pavement Response for Conventional Pavement Sections

Response	Top Subgrade		Bottom AC	
	σ_Z (psi)	ε_Z (10^{-6})	ε_R (10^{-6})	ε_Z (10^{-6})
Section 8	11.9	1850	300	-
Section 9	11.1	1750	280	-
Section 10	6.8	2500	400	-
Ave. Measured (Conventional)	9.9	2000	330	-
TTI-PAVE Prediction				
Linear Isotropy	8.7	1440	252	
Nonlinear Anisotropy	12.3	1932	392	-
CIRCLY Prediction				
Linear Anisotropy	7.0	2110	-628	-

CHAPTER VIII

CONCLUSIONS AND RECOMMENDATIONS

CONCLUSIONS

Anisotropy in granular materials is inherent even before the aggregate base is subjected to traffic due to the effects of compaction and gravity. Stresses due to construction operations and traffic are anisotropic and new particle contacts are formed due to breakage and slippage of particles, which induces further anisotropy. Recent studies by several researchers have mainly indicated that the unbound aggregate base material should be modeled as nonlinear and anisotropic to account for stress sensitivity and the significant differences between vertical and horizontal moduli and Poisson's ratios. The advantage of the use of cross-anisotropy for the analysis of unbound granular bases is the drastic reduction of bottom tensile stresses predicted by linear elastic analysis based on the assumptions of isotropy.

Although it has been shown that the nonlinear cross-anisotropic model is a superior model to characterize unbound granular materials, the determination of anisotropic material properties from conventional triaxial tests has been difficult. Recently, researchers at the International Center for Aggregates Research (ICAR) focused on determining an efficient way to characterize unbound aggregate bases and developed a method to fully characterize the required gamut of stress-sensitive and cross-anisotropic properties of the unbound aggregate base. Repeated triaxial tests using the Rapid Triaxial Tester (RaTT) were performed following the ICAR testing protocol on three aggregate types with three different gradations (coarse, well, and fine) and three different moisture contents (wet, optimum, and dry). Experimental results were analyzed using the ICAR cross-anisotropic model and system identification method. The ICAR model requires nine coefficients to account for the stress-sensitivity and anisotropy of unbound layers. Full-scale resilient modulus tests were performed on all combinations and the nine factors (k_1 through k_9) were determined. This testing provided information to establish an extensive database and offered the opportunity to ascertain whether k-values could be predicted from basic physical properties of the aggregates, including gradation, moisture content, density, and even perhaps particle shape, etc.

Aggregate particle shape properties such as form, angularity, and texture were measured using the image analysis techniques. Fifty particles passing # 4 sieve size were randomly selected for each aggregate source and their shape properties were measured. A general equation was used to describe the distribution curves for gradation and shape properties. The parameters of the equation can be used in regression analysis together to predict resilient modulus behavior and account for both stress-sensitivity and the degree of cross-anisotropy.

The regression equations shown in Equation (5.3) can be used to determine the level or degree of cross-anisotropy based on physical properties: gradation and particle shape. It was found that the aggregate shape has substantial effects on the unbound aggregate behavior and significantly affects the level of anisotropy. From the repeated load triaxial test, it was observed that aggregate mixture which contains more elongated particles has the higher level of anisotropy. Also, the anisotropy level decreases as the aggregate becomes more angular and texture. The effect of level of anisotropy on pavement response was investigated by running the finite element program and it was found that the degree of cross-anisotropy has a substantial effect on the stress distribution and will therefore affect pavement design. It has also found that the gradation has significant impact on the anisotropic behavior. Anisotropy was found to decrease as the aggregate gradation became coarser and well graded.

RECOMMENDATIONS

An unbound aggregate generates its own lateral confining pressure and becomes very stiff almost as if it were forming a moving vertical column that travels along immediately beneath the load (44). This self lateral confining pressure can be explained by the development of self-confinement in the granular base layer, which is the result of dilation effect. Since the dilation occurs when the Poisson’s ratio is higher than 0.5, higher Poisson’s ratio is needed to be inputted. However, elastic theory doesn’t allow to input the Poisson’s ratio higher than 0.5 and thus, it is recommended to develop a rational method to account for the directional Poisson’s effect and the higher levels of Poisson’s ratio, up to a Poisson’s ratio of about 1.0 by simply inputting a residual confining pressure to realistically simulate various levels of Poisson’s ratio.

REFERENCES

1. American Association of State and Highway Officials (AASHTO). *AASHTO Guide for Design of Pavement Structures*. American Association of State and Highway Officials, Washington, DC, 1993.
2. Adu-Osei, A. *Characterization of Unbound Granular Base*. Ph.D. Dissertation, Texas A&M University, College Station, TX, 2000.
3. Masad, E., Dallas N. Little, and Lytton, R.L. Unbound Granular Bases Using Microstructure Distribution Tensors. Accepted in Journal of Geomechanics, ASCE, 2004.
4. Tutumluer, E. *Predicting Behavior of Flexible Pavements with Granular Bases*. Ph.D. Dissertation, School of Civil Environmental Engineering, Georgia Institute of Technology, Atlanta, 1995.
5. Tutumluer, E. and Thompson, M. R. Anisotropic Modelling of Granular Bases in Flexible Pavements. In *Transportation Research Record 1577*. TRB, National Research Council, Washington, DC, 1997, pp.18-26.
6. Tutumluer, E., Little, D.N., and Kim, S.H. A Validated Model for Predicting Field Performance of Aggregate Base Courses. In *Transportation Research Record* 1837, TRB, National Research Council, Washington, DC, 2003, pp. 41-49.
7. Chan, F. K. and Brown, S. F. Significance of Principal Stress Rotation in Pavements. In *Proc., 13th International Conference on Soil Mechanics and Foundation Engineering,* Delhi, Vol. 4, 1994, pp. 1823-1826.
8. Hicks, R. G. and Monismith, C. L. Factors Influencing the Resilient Properties of Granular Materials. In *Transportation Research Record 345,* Transportation Research Board, National Research Council, Washington, DC, 1971, pp. 15-31.
9. Uzan, J. Characterization of Granular Material. In *Transportation Research Record 1022*, TRB, National Research Council, Washington, DC, 1985, pp. 52-59.
10. Uzan, J. Resilient Characterization of Pavement Materials. *International Journal for Numerical and Analytical Methods in Geomechanics,* Vol. 16, No. 6, 1992, pp. 435-459.

11. Lekarp, F., Isacsson. U., and Dawson, A. Resilient Response of Unbound Aggregates, *Journal of Transportation Engineering*, Vol. 126, No.1, ASCE, 2000, pp.66-83.
12. Huang, Y. H. *Pavement Analysis and Design*. 1st Edition, Prentice Hall, Englewood Cliffs, NJ, 1993.
13. Lytton, R. L., Uzan, J., Fernando, E., Roque, R., Hiltunen, D., and Stoffels, S. M. *Development and Validation of Performance Prediction Models and Specifications for Asphalt Binders and Paving Mixes*. Strategic Highway Research Program, SHRP A-357, National Research Council, Washington, DC, 1993.
14. Adu-Osei, A., R.L.Lytton, and D.N.Little, System Identification Method for Determining the Anisotropic Resilient Properties of Unbound Aggregates. *Symposium Unbound Aggregates in Roads (UNBAR5),* University of Nottingham, Nottingham, England, June 21-23, 2000.
15. Adu-Osei, A. and D.N.Little. *Structural Characteristics of Unbound Aggregate Bases to Meet AASHTO 2002 Design Requirements.* Interim Report, International Center for Aggregates Research (ICAR) Project 502, Texas Transportation Institute, Texas A&M University, College Station, TX, 2000.
16. Chen, W. F. and Mizuno, E. *Nonlinear Analysis in Soil Mechanics*. Developments in Geotechnical Engineering, Vol. 53, Elsevier, New York, 1990.
17. Hwang, D. and Witczak, M. W. *Program DAMA (Chevron) User’s Manual*. Department of Civil Engineering, University of Maryland, Silver Spring, 1979.
18. Brown, S. F., O’Reilly, M. P., and Pappin, J. W. A Repeated Load Triaxial Apparatus for Granular Materials. In *Unbound Aggregates in Roads*, R.H.Jones and A.R. Dawson (Eds), Butterworths, London, 1989, pp. 143-158.
19. Boyce, J. R., Brown, S. F. and Pell, P. S. The Resilient Behaviour of a Granular Material Under Repeated Loading. In *Australia Road Research Board,* Vol. 28, 1976, pp. 8-19.
20. Lytton, R. L. Foundations and Pavements on Unsaturated Soils. In *Proc. 1st International Conference on Unsaturated Soils*. Paris, 1995, pp. 1201-1210.

21. Barksdale, R. D., and Itani, S. Y. Influence of Aggregate Shape on Base Behaviour. In *Transportation Research Record* 1227, TRB, National Research Council, Washington, DC, 1989, pp. 173-182.
22. Haynes, J. G., and Yoder, E. J. Effects of Repeated Loading on Gravel and Crushed Stone Base Course Materials Used in the AASHO Road Test. In *Highway Research Record 39*, National Research Council, HRB, 1963. PP. 82-86.
23. Smith, W. S., and Nair, K. *Development of Procedures for Characterization of Untreated Granular Base Coarse and Asphalt-Treated Base Course Materials*. Report No. FHWA-RD-74-61, Federal Highway Administration, Washington, DC, 1973.
24. Dawson, A. R. *Unbound Aggregates in Road.* Balkema, Rotterdam, London, 2000.
25. Rada, G., and Witczak, M. W. Comprehensive Evaluation of Laboratory Resilient Moduli Results for Granular Material. In *Transportation Research Record 810*, TRB, National Research Council, Washington, DC, 1981, pp. 23-33.
26. Raad, L., Weichert, D. and Haidar, A. Shakedown and Fatigue of Pavements with Granular Bases." In *Transportation Research Record 1227*, TRB, National Research Council, Washington DC, 1989, pp. 159-172.
27. Raad, L., Minassian, G., and Gartin, S. Characterization of Saturated Granular Bases under Repeated Loads. In *Transportation Research Record 1369*, TRB, National Research Council, Washington, DC, 1992, pp. 73-82.
28. Thom, N. H., and Brown, S. F. Effect of Moisture on the Structural Performance of a Crushed-Limestone Road Base. In *Transportation Research Record 1121*, TRB, National Research Council, Washington, DC, 1987, pp. 50-56.
29. Tian, P., Zaman, M. M., and Laguros, J. G. Variation of Resilient Modulus of Aggreagte Base and Its Influence on Pavement Performance, *Journal of Testing and Evaluation*, Vol. 26, No. 4, July 1998, pp. 329-335.
30. Hicks, R. G. *Factors Influencing the Resilient Properties of Granular Materials*, PhD Dissertation, University of California, Berkeley, 1970.
31. Allen, J. J. and Thompson, M. R. Resilient Response of Granular Materials Subjected to Time Dependent Lateral Stresses. In *Transportation Research*

Record 510, TRB, National Research Council, Washington, DC, 1974, pp. 173-182.

32. Kolisoja, P. *Resilient Deformation Characteristics of Granular Materials*. PhD Dissertation, Tampere University of Technology, Tampere, Finland, 1997.
33. Brown, S. F. Soil Mechanics in Pavement Engineering. *Geotechnique* Vol. 46, No. 3, 1996, pp. 383-426.
34. Lekarp, F., Isaacson, U. and Dawson, A. State of the Art. I: Resilient Response of Unbound Aggregates; State of the Art. II: Permanent Strain Response of Unbound Aggregates. *Journal of Transportation Engineering*, ASCE, Vol. 126, No. 1, 2000, pp. 66-83.
35. Lekarp, F., Richardson, I. R., and Dawson, A. Influence on Permanent Deformation Behavior of Unbound Granular Materials. In *Transportation Research Record 1547,* TRB, National Research Council, Washington, DC, 1996, pp. 68-75.
36. Clough, R. W. The Finite Element Method in Plane Stress Analysis. In *Proc., 2nd ASCE Conference on Electronic Computation*, Pittsburgh, PA, 1960, pp 2-345.
37. Tutumluer, E. Anisotropic Behavior of Unbound Aggregate Bases. In *Proc., 6th Annual Symposium, International Center for Aggregate Research*, St. Louis, MO, 1998, pp.11-33.
38. Tutumluer, E. Directional Dependency of Aggregate Stiffnesses: An Indicator of Granular Base Performance. In *Proc, 8th Annual Symposium of International Center for Aggregate Research*, Denver, CO, April 2000, pp. 12-14.
39. Yandell, T. Some Effects of Repeated Loads. In *Proc., Australian Road Research Board Conference,* Vol. 3, No. 2, 1966, pp. 1100–1118.
40. Dong, J.J and Pan, Y.W. Micromechanics Model for Elastic Stiffness of Non-Spherical Granular Assembly. *International J. Numer. Anal. Meth. Geomech,* Vol. 23, 1999, pp. 1075-1100.
41. Oda, M., Nemat-Nasser, S., and Konish, J. Stress-Induced Anisotropy in Granular Masses, *Soils and Foundations*, Vol. 25, 1985, pp. 85-97.

42. Oda, M., and Nakayama, N. Yield Function for Soil with Anisotropic Fabric, *Journal of Engineering Mechanics*, ASCE, Vol. 15, 1989, pp. 89-104.
43. Barksdale, R. D., S.F.Brown, and F.Chan. *NCHRP Report 315: Potential Benefts of Geosynthetics in Flexible Pavements Systems,* TRB, National Research Council, Washington, DC, 1989.
44. Lytton, R. L. Characterizing Asphalt Pavements for Performance. In *Transportation Research Record 1723*, TRB, National Research Council, Washington DC, 2000, pp125-132.
45. Wang, F. & Lytton R. L. System Identification Method for Back Calculating Pavement Layer Properties. In *Transportation Research Record 1384*, TRB, National Research Council, Washington, DC, 1993, pp. 1-7.
46. Seyhan, U., *Characterization of Anisotropic Granular Layer Behavior in Flexible Pavements*. Ph.D. Dissertation, University of Illinois at Urbana-Champaign, 2002.
47. Tseng, K. H., and Lytton, R. L. Prediction of permanent deformation in flexible pavement materials. In *J. Assoc. Asphalt Paving Technol.*, Vol. 58, 1989, pp. 155–156.
48. Thompson, M. R., and Nauman D. Rutting Rate Analyses of the AASHO Road Test Flexible Pavements. In *Transportation Research Record 1384*, TRB, National Research Council, Washington, DC, 1993.
49. Thompson, M.R. State-of-the-Art: Unbound Base Performance. In *Proc. 6th Annual Symposium, International Center for Aggregates Research*. St. Louis, MO, 1998. pp. 934-975.
50. Masad, E. and Button, J. Unified Imaging Approach for Measuring Aggregate Angularity and Texture, *Computer-Aided Civil and Infrastructure Engineering,* Vol. 15, 2000, pp. 273-280.
51. Masad, E., Olcott, D., White, D., and Tashman, L. Correlation of Fine Aggregate Imaging Shape Indices with Asphalt Mixture Performance, In *Transportation Research Record 1757*, Transportation Research Board, National Research Council, Washington, DC, 2000, pp. 148-156.

52. Masad, E. Correlation of Fine Aggregate Imaging Shape Indices with Asphalt Mixture Performance, In *Transportation Research Record 1757*, TRB, National Research Council, Washington, DC, 2000, pp. 148-156.
53. Masad, E. *The Development of A Computer Controlled Image Analysis System for Measuring Aggregate Shape Properties*, NCHOP-IDEA Project 77, Final Report, TRB, Washington, DC, 2003.
54. Fredlund, D. G. and Xing, A. Equations for the Soil-Water Characteristic Curve. *Canadian Geotechnical Journal*, Vol. 31, 1994, pp. 521-532.
55. Owen, D. R. J. and Hinton, E. *Finite Elements in Plasticity: Theory and Practice*. Pineridge Press, Swansea, U.K., 1980.
56. Park, S. W. *Evaluation of Accelerated Rut Development in Unbound Pavement Foundations and Load Limits on Load-Zoned Pavements*. Ph.D. Dissertation, Texas A&M University, College Station, TX, 2000.
57. Wardle, L. J. *Computer Program CIRCLY, User's Manual*. MINCAD Systems Pty Ltd., Richmond, Australia, 1986.
58. Porter, D. W. *Technical Basis of the 1992 Austroads Pavement Design Guide (Flexible Pavements)*. ARRB Transport Research No. RC7095-2, Sydney, Australia, 1999.
59. Allen, J. J. The *Effects of Non-Constant Lateral Pressures on Resilient Response of Granular Materials*. Ph.D. Dissertation, University of Illinois at Urbana-Champaign, 1973.
60. Barksdale, R. D. Compressive Stress Pulse Times in Flexible Pavements for Use in Dynamic Testing. In *Highway Research Record 345*, Highway Research Board, 1971, pp. 32-44.
61. Barksdale, R. D. Laboratory Evaluation of Rutting in Base Course Materials. In *Proc., 3rd International Conference on the Structural Design of Asphalt Pavements*, Vol. 1, Ann Arbor, MI, 1972, pp. 161-174.
62. Barrett, P. J., The Shape of Rock Particles, A Critical Review, *Sedimentology* Vol. 27, 1980, pp. 291-303.

63. Bishop, A. W. and Green, G. E. The Influence of End Restraint on the Compression Strength of a Cohesionless Soil. *Geotechnique*, Vol. 15, No. 3, 1965, pp. 243-265.
64. Boyce, J. R. *The Behavior of a Granular Material Under Repeated Load*. Ph.D. Dissertation, Department of Civil Engineering, University of Nottingham, England, 1976.
65. Crockford, W. W., Bendana, L. J., Yang, W. S., Rhee, S. K. and Senadheera, S. P. *Modeling Stress and Strain States in Pavement Structures Incorporating Thick Granular Layers*. Final Report, Texas Transportation Institute, College Station, TX, 1990.
66. Duncan, J. M., Monismith C. L. and Wilson, E. L. Finite Element Analysis of Pavements. In *Highway Research Record 228*, HRB, National Research Council, Washington, DC, 1998, pp. 18-33.
67. FHWA, Highway Statistics. *Federal Highway Administration, Superintendent of Documents*, U.S. Government Printing Office, Washington, DC, 1990.
68. Hornych, P., Kazai, A. and Piau, J. M. Study of the Resilient Behaviour of Unbound Granular Materials. In *Proc., 5th International Conference on the Bearing Capacity of Roads and Airfields*, Vol. 3, 1998, pp. 1277-1287.
69. Industrial Process Control (IPC). *Universal Testing Machine Manual*. Boronia, Australia, 1998.
70. Moore, W. M. and Milberger, L. J. *Evaluation of the TTI Gyratory Compactor*. Texas Transportation Institute Report No. 99-3, 1968.
71. National Association of Australian State Road Authorities. *A Guide to the Structural Design of Road Pavements*. Melbourne, Australia, 1987.
72. Pappin, J. W., Brown, S. F., and O'Reilly, M. P. Effective Stress Behaviour of Saturated and Partially Saturated Granular Material Subjected to Repeated Loading. *Geotecchnique* Vol. 42, No.3, 1992, pp. 485-497.
73. Pickering, D. J. Anisotropic Elastic Parameters for Soil. *Geotechnique* Vol. 20, No. 3, 1970, pp. 271-276.

74. Warren, H. and Dieckman, W. L. *Numerical Computation of Stresses and Strains in a Multiple-Layer Asphalt Pavement System*. International Report, Chevron Research Corporation, Richmond, CA, 1998.

75. Witczak, M. W. & Uzan, J. *Granular Material Characterization.* The Universal Airport Pavement Design System Report I of V, University of Maryland, Department of Civil Engineering, Silver Spring, MD, 1998.

76. Zaman, M.M., Chen, D.H., and Laguros, J.G. Resilient Moduli of Granular Materials. *Journal of Transportation Engineering ASCE*, Vol. 120, No. 6, 1994, pp. 967-988.

77. Zienkiewicz, O. C., Cheung, Y. K. and Stagg, K. G. Particular Reference to Problems of Rock Mechanics. *Journal of Strain Analysis*, Vol. 1, No.2. 1966. pp. 172-182.

APPENDIX A

TABLES OF AVERAGE RESILIENT STRAIN

TABLE A1 Average Resilient Strains for Well Graded Aggregate #1 at Wet of Optimum Moisture Content

Stress State		Triaxial Compression		Triaxial Shear		Triaxial Extension	
Stress (kPa)		Strain (με)		Strain (με)		Strain (με)	
Axial	Radial	Axial	Radial	Axial	Radial	Axial	Radial
40.0	25.0	28.8	-6.0	285.6	-125.5	-152.9	48.0
50.0	25.0	60.7	-18.2	187.1	-125.2	-246.0	85.8
70.0	40.0	28.0	-5.3	65.8	-38.2	-149.4	69.9
130.0	60.0	33.8	-8.0	73.1	-55.0	-55.3	41.8
150.0	70.0	29.2	-7.5	57.0	-39.4	-41.6	31.8
170.0	100.0	27.6	-8.7	47.3	-26.4	-90.5	55.5
220.0	120.0	33.7	-10.4	61.8	-37.1	-58.9	46.1
250.0	140.0	28.1	-9.2	47.4	-30.5	-46.7	41.7
250.0	120.0	28.6	-7.1	51.4	-33.5	-48.2	43.9
250.0	105.0	28.5	-7.2	53.2	-37.9	-52.6	47.1

TABLE A2 Average Resilient Strains for Well Graded Aggregate #1 at Optimum Moisture Content

Stress State		Triaxial Compression		Triaxial Shear		Triaxial Extension	
Stress (kPa)		Strain (με)		Strain (με)		Strain (με)	
Axial	Radial	Axial	Radial	Axial	Radial	Axial	Radial
40.0	25.0	17.5	-4.1	108.0	-69.8	-55.6	30.3
50.0	25.0	32.4	-9.1	72.8	-57.9	-74.2	38.6
70.0	40.0	21.0	-4.2	36.4	-27.5	-73.4	46.1
130.0	60.0	29.8	-6.8	52.6	-45.1	-33.4	31.9
150.0	70.0	26.2	-4.7	43.9	-37.4	-27.7	27.3
170.0	100.0	25.3	-4.9	37.3	-27.1	-61.7	47.8
220.0	120.0	33.1	-6.0	48.5	-37.4	-43.5	41.0
250.0	140.0	30.0	-5.1	41.0	-32.8	-36.0	36.8
250.0	120.0	29.9	-6.6	43.3	-36.9	-37.8	40.6
250.0	105.0	28.7	-5.8	45.3	-40.9	-40.3	43.7

TABLE A3 Average Resilient Strains for Well Graded Aggregate #1 at Dry of Optimum Moisture Content

Stress State		Triaxial Compression		Triaxial Shear		Triaxial Extension	
Stress (kPa)		Strain (με)		Strain (με)		Strain (με)	
Axial	Radial	Axial	Radial	Axial	Radial	Axial	Radial
40.0	25.0	13.8	-2.8	64.1	-32.2	-36.2	18.4
50.0	25.0	29.1	-3.8	55.9	-32.2	-54.6	22.1
70.0	40.0	26.7	-4.5	39.9	-19.5	-58.0	27.2
130.0	60.0	37.1	-7.2	56.7	-34.5	-33.6	19.8
150.0	70.0	30.1	-5.1	47.6	-28.7	-30.0	21.2
170.0	100.0	28.2	-5.5	39.0	-22.4	-63.9	42.6
220.0	120.0	36.8	-6.1	51.4	-34.2	-45.8	36.7
250.0	140.0	32.6	-4.9	42.5	-30.2	-39.7	32.7
250.0	120.0	32.2	-5.6	44.9	-33.0	-39.4	36.2
250.0	105.0	31.1	-6.1	49.2	-37.0	-42.3	39.1

TABLE A4 Average Resilient Strains for Fine Graded Aggregate #1 at Wet of Optimum Moisture Content

Stress State		Triaxial Compression		Triaxial Shear		Triaxial Extension	
Stress (kPa)		Strain (με)		Strain (με)		Strain (με)	
Axial	Radial	Axial	Radial	Axial	Radial	Axial	Radial
40.0	25.0	64.0	-18.8	875.3	-338.8	-301.3	67.0
50.0	25.0	234.4	-89.4	1409.2	-1000.3	-727.5	154.0
70.0	40.0	90.8	-28.6	213.3	-113.5	-435.1	143.7
130.0	60.0	70.6	-28.0	176.3	-172.8	-134.3	97.6
150.0	70.0	53.9	-18.0	110.9	-99.8	-78.9	62.0
170.0	100.0	52.7	-15.1	83.5	-53.5	-185.8	93.2
220.0	120.0	59.9	-16.3	97.9	-71.0	-105.8	70.1
250.0	140.0	52.1	-14.1	82.0	-56.3	-83.7	57.2
250.0	120.0	48.4	-15.3	77.6	-63.7	-80.0	65.1
250.0	105.0	44.2	-13.0	78.7	-74.3	-79.8	73.1

TABLE A5 Average Resilient Strains for Coarse Graded Aggregate #1 at Optimum Moisture Content

Stress State		Triaxial Compression		Triaxial Shear		Triaxial Extension	
Stress (kPa)		Strain (με)		Strain (με)		Strain (με)	
Axial	Radial	Axial	Radial	Axial	Radial	Axial	Radial
40.0	25.0	10.6	-2.0	43.5	-25.4	-23.0	15.5
50.0	25.0	22.9	-2.9	36.2	-23.1	-36.0	16.6
70.0	40.0	17.7	-2.1	27.6	-17.8	-44.4	30.1
130.0	60.0	29.7	-3.4	47.4	-31.0	-29.0	23.9
150.0	70.0	27.2	-3.1	42.1	-27.8	-25.3	21.4
170.0	100.0	26.8	-3.6	37.4	-23.4	-61.5	39.9
220.0	120.0	33.7	-4.1	51.5	-31.4	-43.9	34.0
250.0	140.0	30.9	-4.5	41.8	-27.8	-37.4	32.0
250.0	120.0	30.3	-4.4	45.6	-29.9	-37.6	34.5
250.0	105.0	29.6	-3.9	46.4	-33.9	-40.8	35.7

TABLE A6 Average Resilient Strains for Coarse Graded Aggregate #1 at Optimum Moisture Content

Stress State		Triaxial Compression		Triaxial Shear		Triaxial Extension	
Stress (kPa)		Strain (με)		Strain (με)		Strain (με)	
Axial	Radial	Axial	Radial	Axial	Radial	Axial	Radial
40.0	25.0	18.2	-4.6	88.7	-52.3	-55.0	29.5
50.0	25.0	35.9	-8.8	67.5	-46.3	-77.8	36.7
70.0	40.0	26.6	-4.5	41.2	-25.9	-77.2	46.0
130.0	60.0	36.1	-6.6	61.8	-45.0	-39.4	32.4
150.0	70.0	32.8	-5.7	53.6	-38.8	-33.6	28.0
170.0	100.0	32.7	-7.4	46.6	-27.8	-74.8	51.1
220.0	120.0	42.7	-7.9	62.5	-39.6	-54.9	44.4
250.0	140.0	38.1	-6.3	52.2	-35.8	-45.4	41.6
250.0	120.0	39.1	-8.6	56.4	-40.6	-49.4	44.8
250.0	105.0	38.3	-9.5	58.5	-44.9	-54.5	49.4

TABLE A7 Average Resilient Strains for Coarse Graded Aggregate #1 at Dry of Optimum Moisture Content

Stress State		Triaxial Compression		Triaxial Shear		Triaxial Extension	
Stress (kPa)		Strain (με)		Strain (με)		Strain (με)	
Axial	Radial	Axial	Radial	Axial	Radial	Axial	Radial
40.0	25.0	17.5	-3.6	93.5	-54.7	-55.3	29.7
50.0	25.0	39.0	-9.5	76.5	-53.5	-81.6	37.9
70.0	40.0	27.6	-4.4	50.6	-31.6	-83.0	47.7
130.0	60.0	38.6	-6.7	68.4	-49.9	-44.2	34.6
150.0	70.0	35.5	-5.4	59.0	-41.1	-37.7	29.2
170.0	100.0	33.9	-5.8	51.0	-29.3	-84.0	52.7
220.0	120.0	43.9	-7.0	67.2	-41.4	-59.1	46.4
250.0	140.0	39.2	-6.4	54.8	-37.3	-50.1	41.8
250.0	120.0	38.7	-6.6	60.7	-40.9	-52.6	45.9
250.0	105.0	37.8	-6.7	62.8	-46.5	-59.4	50.3

TABLE A8 Average Resilient Strains for Well Graded Aggregate #2 at Optimum Moisture Content

Stress State		Triaxial Compression		Triaxial Shear		Triaxial Extension	
Stress (kPa)		Strain (με)		Strain (με)		Strain (με)	
Axial	Radial	Axial	Radial	Axial	Radial	Axial	Radial
40.0	25.0	8.0	-2.9	33.4	-21.1	-34.2	16.7
50.0	25.0	16.4	-2.1	29.3	-23.5	-34.3	18.0
70.0	40.0	13.1	-2.1	19.4	-13.5	-39.5	29.0
130.0	60.0	22.8	-5.5	35.4	-28.1	-22.4	21.3
150.0	70.0	21.0	-4.7	29.6	-24.2	-20.5	19.9
170.0	100.0	18.7	-3.3	25.9	-21.6	-39.2	39.3
220.0	120.0	25.7	-4.3	34.5	-31.1	-29.6	35.6
250.0	140.0	23.7	-3.7	32.0	-28.0	-28.4	34.3
250.0	120.0	23.2	-3.4	31.5	-30.3	-25.8	36.0
250.0	105.0	22.9	-3.6	30.9	-31.3	-25.5	36.5

TABLE A9 Average Resilient Strains for Well Graded Aggregate #2 at Dry of Optimum Moisture Content

Stress State		Triaxial Compression		Triaxial Shear		Triaxial Extension	
Stress (kPa)		Strain (με)		Strain (με)		Strain (με)	
Axial	Radial	Axial	Radial	Axial	Radial	Axial	Radial
40.0	25.0	24.2	-3.7	36.0	-31.0	-29.0	36.2
50.0	25.0	17.9	-2.4	30.1	-19.4	-37.9	18.7
70.0	40.0	15.5	-3.1	23.6	-14.3	-43.3	29.2
130.0	60.0	26.0	-6.3	40.6	-30.0	-25.5	22.6
150.0	70.0	23.8	-5.2	33.5	-25.2	-22.1	20.6
170.0	100.0	21.0	-3.6	29.8	-21.9	-48.0	40.6
220.0	120.0	27.7	-5.1	40.0	-30.9	-33.4	37.5
250.0	140.0	25.2	-4.1	33.8	-28.8	-29.7	34.2
250.0	120.0	24.2	-3.7	36.0	-31.0	-29.0	36.2
250.0	105.0	23.8	-3.9	37.8	-33.1	-31.7	38.5

TABLE A10 Average Resilient Strains for Fine Graded Aggregate #2 at Wet of Optimum Moisture Content

Stress State		Triaxial Compression		Triaxial Shear		Triaxial Extension	
Stress (kPa)		Strain (με)		Strain (με)		Strain (με)	
Axial	Radial	Axial	Radial	Axial	Radial	Axial	Radial
40.0	25.0	102.7	-32.6	2168.4	-1317.7	-498.7	120.0
50.0	25.0	604.7	-353.3	4686.8	-5564.4	-1200.8	352.3
70.0	40.0	169.0	-69.9	644.4	-420.8	-701.4	228.6
130.0	60.0	150.4	-106.9	962.1	-1281.7	-538.7	356.0
150.0	70.0	94.4	-60.3	270.1	-323.4	-208.7	164.6
170.0	100.0	64.0	-23.5	118.9	-86.7	-286.3	140.3
220.0	120.0	66.1	-24.2	132.5	-113.3	-140.1	100.1
250.0	140.0	55.3	-16.9	96.9	-78.1	-98.6	75.4
250.0	120.0	51.3	-16.7	98.0	-92.4	-96.4	86.1
250.0	105.0	48.2	-17.7	102.3	-112.6	-103.0	104.0

TABLE A11 Average Resilient Strains for Fine Graded Aggregate #2 at Optimum Moisture Content

Stress State		Triaxial Compression		Triaxial Shear		Triaxial Extension	
Stress (kPa)		Strain (με)		Strain (με)		Strain (με)	
Axial	Radial	Axial	Radial	Axial	Radial	Axial	Radial
40.0	25.0	8.9	-2.2	33.7	-20.4	-21.4	15.0
50.0	25.0	19.5	-1.9	27.3	-17.5	-31.4	15.6
70.0	40.0	15.6	-2.6	23.1	-13.3	-39.1	28.1
130.0	60.0	28.3	-5.3	41.1	-28.8	-26.8	22.8
150.0	70.0	25.5	-4.5	36.5	-25.4	-22.0	20.6
170.0	100.0	23.5	-3.8	32.3	-23.0	-47.4	41.9
220.0	120.0	31.2	-4.8	41.5	-32.6	-35.3	37.7
250.0	140.0	28.3	-4.1	37.8	-31.2	-32.6	36.6
250.0	120.0	27.4	-3.8	36.8	-31.9	-30.3	36.7
250.0	105.0	27.1	-4.0	40.7	-34.3	-30.6	37.9

TABLE A12 Average Resilient Strains for Coarse Graded Aggregate #2 at Dry of Optimum Moisture Content

Stress State		Triaxial Compression		Triaxial Shear		Triaxial Extension	
Stress (kPa)		Strain (με)		Strain (με)		Strain (με)	
Axial	Radial	Axial	Radial	Axial	Radial	Axial	Radial
40.0	25.0	11.3	-2.5	52.7	-32.5	-35.5	20.6
50.0	25.0	22.6	-3.2	44.4	-32.7	-50.2	24.5
70.0	40.0	17.1	-2.5	28.2	-18.3	-60.4	37.0
130.0	60.0	29.4	-8.0	49.1	-39.1	-33.0	29.0
150.0	70.0	26.1	-6.8	41.9	-33.4	-28.4	25.9
170.0	100.0	24.0	-4.5	36.8	-26.7	-64.5	49.7
220.0	120.0	31.8	-5.7	49.2	-39.7	-48.3	45.7
250.0	140.0	28.5	-5.1	42.9	-35.0	-41.7	42.0
250.0	120.0	28.3	-5.1	44.3	-38.9	-41.8	44.8
250.0	105.0	28.3	-6.4	46.8	-42.9	-41.8	47.1

TABLE A13 Average Resilient Strains for Well Graded Aggregate #3 at Wet of Optimum Moisture Content

Stress State		Triaxial Compression		Triaxial Shear		Triaxial Extension	
Stress (kPa)		Strain (με)		Strain (με)		Strain (με)	
Axial	Radial	Axial	Radial	Axial	Radial	Axial	Radial
40.0	25.0	32.6	-6.5	191.6	-107.6	-148.8	67.0
50.0	25.0	67.6	-21.3	146.9	-109.5	-201.6	108.9
70.0	40.0	50.8	-13.0	95.5	-60.8	-188.8	98.7
130.0	60.0	66.6	-17.7	125.0	-91.0	-94.2	68.7
150.0	70.0	57.3	-9.8	101.5	-67.1	-75.0	53.5
170.0	100.0	51.0	-6.7	80.9	-43.7	-133.1	80.8
220.0	120.0	64.2	-12.6	102.5	-62.9	-98.7	68.9
250.0	140.0	55.3	-10.5	84.6	-51.8	-80.6	57.2
250.0	120.0	53.7	-11.2	88.0	-60.4	-85.2	66.3
250.0	105.0	53.0	-11.7	92.5	-68.9	-89.7	74.5

TABLE A14 Average Resilient Strains for Well Graded Aggregate #3 at Optimum Moisture Content

Stress State		Triaxial Compression		Triaxial Shear		Triaxial Extension	
Stress (kPa)		Strain (με)		Strain (με)		Strain (με)	
Axial	Radial	Axial	Radial	Axial	Radial	Axial	Radial
40.0	25.0	33.1	-6.8	202.1	-120.1	-123.0	61.0
50.0	25.0	65.5	-15.1	130.0	-88.0	-157.5	75.1
70.0	40.0	49.2	-7.4	82.2	-42.3	-169.5	85.3
130.0	60.0	70.1	-14.4	122.9	-83.1	-85.8	58.3
150.0	70.0	61.4	-11.6	101.3	-64.8	-68.6	48.6
170.0	100.0	56.4	-8.4	84.2	-46.8	-138.9	82.4
220.0	120.0	71.5	-11.0	107.9	-63.4	-103.4	71.2
250.0	140.0	61.9	-8.7	91.3	-54.5	-87.8	62.8
250.0	120.0	60.9	-9.7	93.8	-61.0	-88.9	68.7
250.0	105.0	60.1	-10.4	96.6	-68.7	-91.0	73.8

TABLE A15 Average Resilient Strains for Well Graded Aggregate #3 at Dry of Optimum Moisture Content

Stress State		Triaxial Compression		Triaxial Shear		Triaxial Extension	
Stress (kPa)		Strain (με)		Strain (με)		Strain (με)	
Axial	Radial	Axial	Radial	Axial	Radial	Axial	Radial
40.0	25.0	20.3	-2.8	90.9	-53.9	-65.8	39.5
50.0	25.0	45.0	-7.9	78.8	-56.8	-93.4	47.0
70.0	40.0	35.4	-4.7	54.1	-30.9	-104.3	66.7
130.0	60.0	53.1	-12.0	89.0	-65.6	-61.1	49.9
150.0	70.0	46.6	-9.1	75.5	-55.6	-49.3	44.3
170.0	100.0	44.8	-7.7	65.5	-42.4	-106.7	79.1
220.0	120.0	57.5	-10.7	87.8	-61.3	-84.2	71.3
250.0	140.0	51.5	-9.1	75.6	-54.1	-71.5	63.9
250.0	120.0	50.3	-9.7	77.0	-60.9	-72.0	70.4
250.0	105.0	50.0	-11.0	78.6	-67.8	-73.5	74.9

TABLE A16 Average Resilient Strains for Fine Graded Aggregate #3 at Wet of Optimum Moisture Content

Stress State		Triaxial Compression		Triaxial Shear		Triaxial Extension	
Stress (kPa)		Strain (με)		Strain (με)		Strain (με)	
Axial	Radial	Axial	Radial	Axial	Radial	Axial	Radial
40.0	25.0	47.0	-11.4	392.6	-255.3	-211.5	88.1
50.0	25.0	79.6	-25.7	207.7	-176.0	-223.6	111.8
70.0	40.0	52.3	-11.3	85.5	-51.6	-181.9	98.0
130.0	60.0	67.9	-17.8	121.0	-93.0	-80.3	61.1
150.0	70.0	58.9	-14.4	97.3	-71.0	-63.7	51.3
170.0	100.0	56.9	-11.3	83.4	-48.3	-143.8	88.0
220.0	120.0	74.0	-13.8	106.9	-69.2	-103.3	75.4
250.0	140.0	66.4	-11.6	94.8	-57.6	-87.9	65.4
250.0	120.0	63.0	-11.6	93.8	-63.7	-85.0	70.0
250.0	105.0	60.1	-11.9	94.6	-67.2	-85.1	73.4

TABLE A17 Average Resilient Strains for Fine Graded Aggregate #3 at Optimum Moisture Content

Stress State		Triaxial Compression		Triaxial Shear		Triaxial Extension	
Stress (kPa)		Strain (με)		Strain (με)		Strain (με)	
Axial	Radial	Axial	Radial	Axial	Radial	Axial	Radial
40.0	25.0	41.9	-9.1	364.6	-244.1	-230.0	97.6
50.0	25.0	84.9	-28.9	195.6	-167.2	-269.2	141.7
70.0	40.0	49.4	-10.9	101.0	-67.0	-192.2	108.1
130.0	60.0	68.3	-18.0	120.5	-93.2	-80.4	63.1
150.0	70.0	61.4	-17.7	98.9	-70.8	-65.5	51.1
170.0	100.0	54.0	-11.0	81.3	-46.8	-127.6	87.0
220.0	120.0	68.7	-13.4	102.0	-66.2	-94.0	74.0
250.0	140.0	60.9	-11.0	88.4	-57.0	-78.6	66.1
250.0	120.0	60.3	-11.7	90.6	-64.0	-80.7	72.3
250.0	105.0	58.3	-12.6	93.9	-69.6	-82.5	77.7

TABLE A18 Average Resilient Strains for Fine Graded Aggregate #3 at Dry of Optimum Moisture Content

Stress State		Triaxial Compression		Triaxial Shear		Triaxial Extension	
Stress (kPa)		Strain (με)		Strain (με)		Strain (με)	
Axial	Radial	Axial	Radial	Axial	Radial	Axial	Radial
40.0	25.0	20.3	-2.4	71.9	-35.1	-45.3	28.7
50.0	25.0	40.1	-3.3	66.2	-43.8	-269.2	141.7
70.0	40.0	33.1	-2.5	49.0	-25.8	-82.6	52.7
130.0	60.0	52.1	-7.0	80.5	-50.8	-50.7	40.3
150.0	70.0	49.4	-8.7	70.9	-43.3	-44.3	35.9
170.0	100.0	44.8	-5.3	63.1	-34.9	-96.3	66.9
220.0	120.0	59.0	-7.2	84.4	-50.2	-74.5	61.1
250.0	140.0	53.2	-6.3	75.4	-46.1	-64.9	57.2
250.0	120.0	52.6	-6.5	77.5	-50.8	-66.5	60.5
250.0	105.0	52.2	-7.5	78.6	-55.8	-69.5	63.9

TABLE A19 Average Resilient Strains for Coarse Graded Aggregate #3 at Wet of Optimum Moisture Content

Stress State		Triaxial Compression		Triaxial Shear		Triaxial Extension	
Stress (kPa)		Strain (με)		Strain (με)		Strain (με)	
Axial	Radial	Axial	Radial	Axial	Radial	Axial	Radial
40.0	25.0	26.9	-3.7	145.2	-88.0	-98.6	52.5
50.0	25.0	53.3	-12.5	113.5	-82.8	-124.3	62.8
70.0	40.0	40.5	-7.3	65.2	-40.1	-133.9	80.6
130.0	60.0	58.8	-14.1	100.7	-76.6	-71.7	58.3
150.0	70.0	54.5	-14.6	83.8	-64.5	-60.2	51.6
170.0	100.0	49.6	-9.4	76.1	-48.5	-132.7	87.9
220.0	120.0	62.8	-11.8	101.3	-68.1	-104.4	78.8
250.0	140.0	55.5	-9.8	88.8	-60.1	-89.2	71.4
250.0	120.0	54.6	-10.9	87.2	-68.3	-90.9	79.3
250.0	105.0	53.6	-11.8	88.5	-75.1	-90.4	86.4

TABLE A20 Average Resilient Strains for Coarse Graded Aggregate #3 at Optimum Moisture Content

Stress State		Triaxial Compression		Triaxial Shear		Triaxial Extension	
Stress (kPa)		Strain (με)		Strain (με)		Strain (με)	
Axial	Radial	Axial	Radial	Axial	Radial	Axial	Radial
40.0	25.0	25.5	-3.8	135.6	-77.9	-88.0	46.2
50.0	25.0	47.8	-8.0	94.4	-67.0	-118.1	54.3
70.0	40.0	40.5	-7.3	65.2	-40.1	-133.9	80.6
130.0	60.0	54.4	-10.7	97.7	-74.0	-70.4	56.6
150.0	70.0	48.9	-10.0	83.0	-61.8	-58.4	48.3
170.0	100.0	46.4	-7.7	71.1	-45.0	-121.4	82.3
220.0	120.0	58.9	-11.0	92.4	-64.7	-88.5	74.3
250.0	140.0	52.4	-8.9	77.3	-58.2	-76.1	67.9
250.0	120.0	51.4	-9.9	81.3	-65.2	-77.3	74.3
250.0	105.0	51.0	-11.1	83.8	-73.0	-82.2	82.1

TABLE A21 Average Resilient Strains for Well Graded Aggregate #4 at Optimum Moisture Content

Stress State		Triaxial Compression		Triaxial Shear		Triaxial Extension	
Stress (kPa)		Strain (με)		Strain (με)		Strain (με)	
Axial	Radial	Axial	Radial	Axial	Radial	Axial	Radial
40.0	25.0	18.0	-3.4	80.6	-42.9	-56.4	34.6
50.0	25.0	40.6	-4.0	67.1	-41.6	-85.4	39.9
70.0	40.0	36.0	-6.6	53.1	-30.4	-90.5	57.2
130.0	60.0	52.4	-10.9	78.6	-56.0	-54.2	46.2
150.0	70.0	45.7	-6.1	68.8	-49.7	-46.7	41.1
170.0	100.0	42.1	-5.0	59.3	-37.6	-94.5	71.4
220.0	120.0	55.5	-6.6	77.9	-52.8	-73.2	62.9
250.0	140.0	49.8	-5.6	69.8	-46.8	-62.9	56.3
250.0	120.0	48.3	-6.8	70.3	-53.0	-64.3	62.5
250.0	105.0	48.1	-6.5	72.0	-57.1	-65.9	67.5

TABLE A22 Average Resilient Strains for Fine Graded Aggregate #4 at Optimum Moisture Content

Stress State		Triaxial Compression		Triaxial Shear		Triaxial Extension	
Stress (kPa)		Strain (με)		Strain (με)		Strain (με)	
Axial	Radial	Axial	Radial	Axial	Radial	Axial	Radial
40.0	25.0	26.5	-4.5	108.0	-66.8	-81.3	53.7
50.0	25.0	56.3	-6.6	91.7	-61.5	-111.6	61.3
70.0	40.0	49.1	-9.4	72.6	-44.3	-124.9	83.5
130.0	60.0	73.3	-16.2	109.4	-78.5	-72.0	62.4
150.0	70.0	63.3	-9.2	93.7	-66.3	-61.6	55.2
170.0	100.0	60.0	-8.2	83.7	-51.6	-129.5	97.1
220.0	120.0	77.4	-11.0	109.5	-71.8	-99.6	85.0
250.0	140.0	70.0	-9.3	98.3	-64.2	-87.3	75.7
250.0	120.0	70.6	-9.9	100.9	-69.6	-89.1	82.7
250.0	105.0	69.6	-10.0	102.0	-76.0	-90.7	88.0

TABLE A23 Average Resilient Strains for Coarse Graded Aggregate #4 at Optimum Moisture Content

Stress State		Triaxial Compression		Triaxial Shear		Triaxial Extension	
Stress (kPa)		Strain (με)		Strain (με)		Strain (με)	
Axial	Radial	Axial	Radial	Axial	Radial	Axial	Radial
40.0	25.0	22.4	-5.6	106.1	-63.5	-83.3	47.2
50.0	25.0	48.9	-5.6	90.4	-65.3	-114.4	55.9
70.0	40.0	41.7	-6.0	67.6	-38.3	-126.8	75.7
130.0	60.0	64.6	-13.0	104.4	-75.4	-71.4	58.0
150.0	70.0	58.7	-11.3	90.3	-64.3	-59.8	51.4
170.0	100.0	53.5	-6.8	77.9	-46.8	-128.9	88.5
220.0	120.0	69.6	-9.7	104.2	-68.5	-99.5	79.1
250.0	140.0	62.5	-8.0	91.5	-58.9	-85.1	68.6
250.0	120.0	61.1	-8.8	93.8	-66.6	-87.6	77.1
250.0	105.0	59.9	-9.1	95.4	-74.9	-89.8	84.0

TABLE A24 Average Resilient Strains for Well Graded Aggregate #5 at Wet of Optimum Moisture Content

Stress State		Triaxial Compression		Triaxial Shear		Triaxial Extension	
Stress (kPa)		Strain (με)		Strain (με)		Strain (με)	
Axial	Radial	Axial	Radial	Axial	Radial	Axial	Radial
40.0	25.0	47.0	-15.1	344.2	-173.2	-155.6	53.9
50.0	25.0	62.3	-19.8	176.4	-128.6	-193.6	76.7
70.0	40.0	43.8	-10.0	79.4	-49.1	-170.8	79.5
130.0	60.0	47.2	-11.4	84.7	-70.5	-57.7	45.7
150.0	70.0	39.3	-8.8	69.0	-52.5	-46.1	37.1
170.0	100.0	42.4	-9.0	61.8	-37.6	-117.4	67.5
220.0	120.0	54.4	-12.1	79.8	-55.3	-80.2	54.2
250.0	140.0	46.2	-8.7	67.8	-44.4	-64.2	46.7
250.0	120.0	44.7	-10.4	68.5	-52.0	-64.1	50.7
250.0	105.0	41.2	-11.4	65.6	-55.3	-66.1	58.5

TABLE A25 Average Resilient Strains for Well Graded Aggregate #5 at Optimum Moisture Content

Stress State		Triaxial Compression		Triaxial Shear		Triaxial Extension	
Stress (kPa)		Strain (με)		Strain (με)		Strain (με)	
Axial	Radial	Axial	Radial	Axial	Radial	Axial	Radial
40.0	25.0	22.7	-6.2	108.8	-69.7	-65.9	36.4
50.0	25.0	43.9	-11.6	78.7	-55.5	-85.5	41.2
70.0	40.0	31.2	-5.0	47.9	-30.1	-90.1	53.2
130.0	60.0	45.7	-7.5	76.1	-53.9	-48.3	36.7
150.0	70.0	40.5	-7.1	65.1	-44.1	-41.3	31.6
170.0	100.0	38.5	-6.2	55.7	-32.3	-88.7	56.5
220.0	120.0	49.2	-8.1	71.9	-45.2	-64.7	47.9
250.0	140.0	43.2	-6.6	60.0	-38.7	-55.9	43.3
250.0	120.0	43.5	-9.0	62.6	-43.1	-55.6	47.9
250.0	105.0	42.4	-7.4	65.4	-47.7	-57.5	51.5

TABLE A26 Average Resilient Strains for Well Graded Aggregate #5 at a Dry of Optimum Moisture Content

Stress State		Triaxial Compression		Triaxial Shear		Triaxial Extension	
Stress (kPa)		Strain (με)		Strain (με)		Strain (με)	
Axial	Radial	Axial	Radial	Axial	Radial	Axial	Radial
40.0	25.0	22.5	-4.0	81.1	-40.3	-51.7	23.6
50.0	25.0	38.8	-6.1	65.8	-38.2	-68.7	28.1
70.0	40.0	28.3	-2.6	46.9	-25.6	-77.8	42.4
130.0	60.0	42.3	-5.5	68.9	-43.0	-43.8	31.7
150.0	70.0	37.1	-4.5	59.0	-36.7	-35.1	27.5
170.0	100.0	36.9	-4.9	51.5	-28.5	-85.1	52.1
220.0	120.0	46.8	-8.1	68.7	-41.1	-63.4	45.2
250.0	140.0	42.4	-5.7	59.8	-37.9	-53.7	41.0
250.0	120.0	41.9	-8.1	61.7	-41.3	-54.4	44.7
250.0	105.0	40.0	-6.2	62.6	-44.1	-57.1	48.5

TABLE A27 Average Resilient Strains for Fine Graded Aggregate #5 at Wet of Optimum Moisture Content

Stress State		Triaxial Compression		Triaxial Shear		Triaxial Extension	
Stress (kPa)		Strain (με)		Strain (με)		Strain (με)	
Axial	Radial	Axial	Radial	Axial	Radial	Axial	Radial
40.0	25.0	52.9	-18.9	542.1	-388.6	-187.9	80.0
50.0	25.0	129.6	-79.0	772.1	-1043.8	-391.0	183.5
70.0	40.0	55.1	-24.4	115.0	-102.9	-246.7	152.4
130.0	60.0	100.1	-34.2	247.1	-214.8	-179.5	115.7
150.0	70.0	79.6	-23.9	159.3	-124.4	-111.0	76.6
170.0	100.0	72.9	-18.7	118.3	-70.2	-222.4	118.3
220.0	120.0	80.6	-20.3	132.6	-89.7	-131.1	88.8
250.0	140.0	71.1	-18.7	105.6	-69.6	-100.1	72.9
250.0	120.0	65.8	-17.7	104.1	-79.3	-98.8	81.0
250.0	105.0	61.3	-15.6	104.8	-90.5	-100.4	89.9

TABLE A28 Average Resilient Strains for Fine Graded Aggregate #5 at Optimum Moisture Content

Stress State		Triaxial Compression		Triaxial Shear		Triaxial Extension	
Stress (kPa)		Strain (με)		Strain (με)		Strain (με)	
Axial	Radial	Axial	Radial	Axial	Radial	Axial	Radial
40.0	25.0	19.5	-2.9	77.5	-39.1	-41.6	23.0
50.0	25.0	39.0	-5.4	61.1	-35.5	-67.2	26.8
70.0	40.0	27.9	-2.5	45.4	-24.8	-71.6	42.8
130.0	60.0	43.0	-5.9	67.3	-43.9	-41.2	30.1
150.0	70.0	38.4	-4.9	59.4	-37.5	-36.7	28.7
170.0	100.0	35.4	-4.6	50.7	-29.7	-78.8	54.8
220.0	120.0	47.8	-9.1	67.0	-43.6	-59.1	48.5
250.0	140.0	42.8	-6.4	59.9	-39.9	-51.8	45.9
250.0	120.0	42.2	-7.4	60.6	-42.9	-52.8	48.4
250.0	105.0	40.5	-8.0	62.3	-48.4	-54.9	52.7

TABLE A29 Average Resilient Strains for Fine Graded Aggregate #5 at Dry of Optimum Moisture Content

Stress State		Triaxial Compression		Triaxial Shear		Triaxial Extension	
Stress (kPa)		Strain (με)		Strain (με)		Strain (με)	
Axial	Radial	Axial	Radial	Axial	Radial	Axial	Radial
40.0	25.0	18.0	-2.6	66.2	-32.7	-36.3	18.8
50.0	25.0	37.4	-4.2	57.4	-29.5	-58.4	22.4
70.0	40.0	29.2	-2.3	41.3	-20.8	-64.6	35.6
130.0	60.0	42.4	-3.8	66.5	-39.4	-40.0	27.8
150.0	70.0	38.3	-3.6	56.3	-33.0	-34.2	25.4
170.0	100.0	36.2	-4.4	49.2	-25.6	-77.3	48.7
220.0	120.0	48.1	-6.8	67.1	-38.7	-61.5	44.5
250.0	140.0	42.5	-6.0	59.9	-35.3	-54.5	41.2
250.0	120.0	42.0	-6.7	60.6	-39.0	-53.4	44.2
250.0	105.0	40.8	-6.2	59.9	-41.4	-54.9	46.9

TABLE A30 Average Resilient Strains for Coarse Graded Aggregate #5 at Optimum Moisture Content

Stress State		Triaxial Compression		Triaxial Shear		Triaxial Extension	
Stress (kPa)		Strain (με)		Strain (με)		Strain (με)	
Axial	Radial	Axial	Radial	Axial	Radial	Axial	Radial
40.0	25.0	28.8	-7.6	131.3	-75.0	-82.3	39.4
50.0	25.0	53.0	-12.6	102.3	-64.9	-111.3	49.5
70.0	40.0	39.1	-7.5	66.8	-39.5	-118.3	64.1
130.0	60.0	51.4	-9.6	89.6	-61.8	-60.5	43.1
150.0	70.0	45.7	-8.0	75.9	-50.7	-49.7	36.7
170.0	100.0	44.2	-7.4	65.9	-38.7	-105.7	66.9
220.0	120.0	57.2	-10.5	84.0	-53.3	-88.8	58.5
250.0	140.0	52.4	-10.5	74.2	-46.4	-72.3	53.1
250.0	120.0	51.5	-9.8	77.4	-52.9	-73.1	57.1
250.0	105.0	48.8	-8.9	76.6	-58.9	-73.6	62.5

TABLE A31 Average Resilient Strains for Well Graded Aggregate #6 at Wet of Optimum Moisture Content

Stress State		Triaxial Compression		Triaxial Shear		Triaxial Extension	
Stress (kPa)		Strain (με)		Strain (με)		Strain (με)	
Axial	Radial	Axial	Radial	Axial	Radial	Axial	Radial
40.0	25.0	13.9	-2.4	61.1	-28.7	-36.3	17.9
50.0	25.0	29.5	-2.3	46.7	-25.1	-52.8	19.6
70.0	40.0	23.3	-2.1	31.7	-14.9	-59.4	30.0
130.0	60.0	37.3	-6.1	52.6	-29.2	-34.1	22.7
150.0	70.0	31.9	-4.6	43.8	-25.2	-27.6	20.6
170.0	100.0	29.3	-3.2	39.3	-21.0	-65.9	39.0
220.0	120.0	37.9	-3.5	52.0	-29.6	-48.5	34.3
250.0	140.0	33.8	-3.1	44.8	-26.7	-41.4	32.4
250.0	120.0	32.9	-2.8	45.4	-28.8	-40.7	33.5
250.0	105.0	32.4	-3.2	46.1	-30.9	-40.2	35.4

TABLE A32 Average Resilient Strains for Well Graded Aggregate #6 at Optimum Moisture Content

Stress State		Triaxial Compression		Triaxial Shear		Triaxial Extension	
Stress (kPa)		Strain (με)		Strain (με)		Strain (με)	
Axial	Radial	Axial	Radial	Axial	Radial	Axial	Radial
40.0	25.0	15.8	-3.2	67.7	-34.3	-49.8	22.1
50.0	25.0	29.2	-3.9	49.4	-29.1	-62.7	25.5
70.0	40.0	22.3	-3.1	36.1	-18.7	-76.4	36.0
130.0	60.0	33.4	-5.7	55.4	-34.7	-38.9	26.3
150.0	70.0	30.7	-6.7	47.0	-28.8	-32.5	23.5
170.0	100.0	28.8	-4.3	40.7	-22.9	-69.8	42.7
220.0	120.0	35.8	-5.0	51.8	-33.1	-51.1	37.9
250.0	140.0	31.6	-4.3	44.6	-28.7	-43.2	34.3
250.0	120.0	30.3	-4.4	45.3	-32.6	-43.2	37.1
250.0	105.0	30.0	-5.0	46.3	-35.7	-43.3	39.4

TABLE A33 Average Resilient Strains for Well Graded Aggregate #6 at a Dry of Optimum Moisture Content

Stress State		Triaxial Compression		Triaxial Shear		Triaxial Extension	
Stress (kPa)		Strain (με)		Strain (με)		Strain (με)	
Axial	Radial	Axial	Radial	Axial	Radial	Axial	Radial
40.0	25.0	32.7	-17.7	296.8	-194.6	-162.4	65.9
50.0	25.0	50.0	-14.9	109.3	-83.8	-158.0	71.5
70.0	40.0	40.4	-13.3	57.8	-31.4	-133.1	59.9
130.0	60.0	44.5	-11.6	75.5	-51.5	-53.5	34.9
150.0	70.0	36.1	-7.3	58.6	-37.7	-41.1	28.3
170.0	100.0	32.6	-6.2	48.8	-27.1	-91.9	49.7
220.0	120.0	39.2	-7.0	60.6	-37.9	-60.0	41.9
250.0	140.0	34.7	-5.3	50.6	-32.1	-48.6	36.4
250.0	120.0	33.3	-5.4	51.9	-35.4	-49.0	39.6
250.0	105.0	32.1	-6.3	54.1	-39.9	-50.4	43.3

TABLE A34 Average Resilient Strains for Fine Graded Aggregate #6 at Optimum Moisture Content

Stress State		Triaxial Compression		Triaxial Shear		Triaxial Extension	
Stress (kPa)		Strain (με)		Strain (με)		Strain (με)	
Axial	Radial	Axial	Radial	Axial	Radial	Axial	Radial
40.0	25.0	36.5	-12.9	287.7	-204.9	-199.9	90.8
50.0	25.0	74.7	-33.3	202.7	-196.3	-306.6	169.3
70.0	40.0	45.0	-13.2	86.3	-60.3	-236.7	127.9
130.0	60.0	54.6	-20.8	110.5	-103.1	-80.2	64.3
150.0	70.0	49.3	-19.5	84.9	-73.4	-60.3	50.0
170.0	100.0	46.3	-14.3	72.4	-49.8	-158.3	93.8
220.0	120.0	56.0	-17.2	93.9	-71.2	-101.0	72.2
250.0	140.0	48.4	-13.7	76.2	-55.6	-79.6	59.4
250.0	120.0	44.9	-13.8	76.9	-64.1	-78.3	66.0
250.0	105.0	41.9	-13.8	76.9	-73.4	-78.0	74.2

TABLE A35 Average Resilient Strains for Coarse Graded Aggregate #6 at Dry of Optimum Moisture Content

Stress State		Triaxial Compression		Triaxial Shear		Triaxial Extension	
Stress (kPa)		Strain (με)		Strain (με)		Strain (με)	
Axial	Radial	Axial	Radial	Axial	Radial	Axial	Radial
40.0	25.0	14.9	-3.2	69.4	-36.7	-49.2	26.3
50.0	25.0	31.8	-4.0	53.4	-33.3	-70.1	31.6
70.0	40.0	28.4	-7.3	39.4	-22.2	-72.0	40.8
130.0	60.0	37.0	-6.0	57.3	-40.4	-38.6	30.3
150.0	70.0	32.0	-5.7	48.2	-33.4	-32.4	27.0
170.0	100.0	30.8	-4.3	42.4	-25.0	-73.6	48.9
220.0	120.0	40.3	-5.4	56.0	-37.1	-53.6	43.0
250.0	140.0	35.7	-4.2	48.7	-32.3	-45.2	38.6
250.0	120.0	34.7	-4.7	49.6	-36.8	-44.7	41.4
250.0	105.0	33.8	-5.1	50.4	-40.3	-46.0	46.8

APPENDIX B

TABLES OF ANISOTROPIC RESILIENT MODULI

TABLE B1 Moduli and Modular Ratio for Well Graded Aggregate #1 at Wet of Optimum Moisture Content

Stress (kPa)		Moduli (kPa)		
Axial	Radial	Horizontal	Vertical	Shear
40	25	114,783	84,532	18,243
50	25	64,584	71,245	24,014
70	40	189,289	150,782	72,161
130	60	237,826	348,814	117,089
150	70	315,614	458,562	155,671
170	100	419,604	508,853	203,547
220	120	475,327	663,085	227,395
250	140	537,118	854,603	288,753
250	120	531,045	754,256	265,139
250	105	475,191	720,299	246,962

TABLE B2 Moduli and Modular Ratio for Well Graded Aggregate #1 at Optimum Moisture Content

Stress (kPa)		Moduli (kPa)		
Axial	Radial	Horizontal	Vertical	Shear
40	25	118,888	148,904	42,184
50	25	119,135	197,700	57,361
70	40	217,327	284,693	117,391
130	60	270,294	502,614	153,476
150	70	328,876	569,496	184,531
170	100	413,877	593,559	232,923
220	120	458,964	735,262	261,995
250	140	509,759	853,742	304,652
250	120	450,256	862,752	280,687
250	105	428,428	818,828	260,920

TABLE B3 Moduli and Modular Ratio for Well Graded Aggregate #1 at Dry of Optimum Moisture Content

Stress (kPa)		Moduli (kPa)		
Axial	Radial	Horizontal	Vertical	Shear
40	25	255,249	220,508	77,902
50	25	235,573	232,657	85,114
70	40	307,129	286,927	126,150
130	60	347,684	451,771	164,377
150	70	423,429	514,569	196,579
170	100	477,831	562,883	244,274
220	120	496,130	678,478	262,897
250	140	548,935	781,747	309,436
250	120	509,685	787,903	288,641
250	105	477,004	758,983	260,941

TABLE B4 Moduli and Modular Ratio for Fine Graded Aggregate #1 at Wet of Optimum Moisture Content

Stress (kPa)		Moduli (kPa)		
Axial	Radial	Horizontal	Vertical	Shear
40	25	47,320	80,000	6,178
50	25	9,989	90,000	3,113
70	40	61,533	100,000	22,952
130	60	72,951	180,538	42,968
150	70	122,724	261,681	71,202
170	100	201,979	258,414	109,426
220	120	240,380	379,214	133,210
250	140	298,067	459,198	162,621
250	120	258,879	507,453	159,145
250	105	235,354	502,794	147,081

TABLE B5 Moduli and Modular Ratio for Fine Graded Aggregate #1 at Optimum Moisture Content

Stress (kPa)		Moduli (kPa)		
Axial	Radial	Horizontal	Vertical	Shear
40	25	279,640	200,000	108,897
50	25	286,201	250,000	126,370
70	40	350,044	300,000	165,237
130	60	411,872	496,167	191,298
150	70	451,925	560,312	214,776
170	100	492,201	550,196	246,460
220	120	589,410	672,855	271,616
250	140	604,095	810,730	322,887
250	120	594,326	785,297	298,084
250	105	546,101	748,694	280,093

TABLE B6 Moduli and Modular Ratio for Coarse Graded Aggregate #1 at Optimum Moisture Content

Stress (kPa)		Moduli (kPa)		
Axial	Radial	Horizontal	Vertical	Shear
40	25	142,459	163,539	53,205
50	25	140,614	192,265	65,884
70	40	225,981	247,298	111,780
130	60	276,119	406,401	140,510
150	70	315,713	463,870	162,392
170	100	385,236	494,304	201,585
220	120	429,538	578,404	220,421
250	140	463,891	671,259	255,705
250	120	407,540	659,378	231,942
250	105	371,193	645,678	217,615

TABLE B7 Moduli and Modular Ratio for Coarse Graded Aggregate #1 at Dry of Optimum Moisture Content

Stress (kPa)		Moduli (kPa)		
Axial	Radial	Horizontal	Vertical	Shear
40	25	149,119	152,322	50,603
50	25	125,824	176,472	57,705
70	40	207,659	218,467	91,169
130	60	255,564	364,151	126,787
150	70	306,960	410,034	149,782
170	100	393,689	425,495	186,946
220	120	430,723	527,566	207,268
250	140	452,726	628,884	244,339
250	120	435,094	596,905	221,390
250	105	392,131	566,010	205,809

TABLE B8 Moduli and Modular Ratio for Well Graded Aggregate #2 at Optimum Moisture Content

Stress (kPa)		Moduli (kPa)		
Axial	Radial	Horizontal	Vertical	Shear
40	25	283,141	391,304	137,843
50	25	288,939	405,278	141,983
70	40	415,126	494,561	228,215
130	60	405,010	737,007	236,314
150	70	449,889	820,109	278,736
170	100	510,595	861,690	315,929
220	120	533,119	1,017,807	343,235
250	140	592,330	1,072,091	374,871
250	120	559,220	1,111,712	364,126
250	105	537,811	1,140,720	361,697

TABLE B9 Moduli and Modular Ratio for Well Graded Aggregate #2 at Dry of Optimum Moisture Content

Stress (kPa)		Moduli (kPa)		
Axial	Radial	Horizontal	Vertical	Shear
40	25	164,776	243,274	111,958
50	25	339,827	379,105	151,584
70	40	389,625	449,169	198,218
130	60	380,362	645,896	212,354
150	70	433,188	734,705	255,370
170	100	507,303	729,300	290,224
220	120	543,554	913,817	317,642
250	140	573,907	1,022,878	359,418
250	120	567,149	1,006,053	335,873
250	105	542,408	967,050	317,386

TABLE B10 Moduli and Modular Ratio for Fine Graded Aggregate #2 at Wet of Optimum Moisture Content

Stress (kPa)		Moduli (kPa)		
Axial	Radial	Horizontal	Vertical	Shear
40	25	6,413	44,680	2,151
50	25	1,494	8,857	732
70	40	18,878	38,180	7,041
130	60	10,239	99,114	6,685
150	70	36,984	157,471	25,273
170	100	126,984	201,334	72,949
220	120	156,579	325,043	91,564
250	140	221,666	411,620	128,574
250	120	192,137	426,894	118,152
250	105	160,005	431,700	104,688

TABLE B11 Moduli and Modular Ratio for Fine Graded Aggregate #2 at Optimum Moisture Content

Stress (kPa)		Moduli (kPa)		
Axial	Radial	Horizontal	Vertical	Shear
40	25	309,932	404,827	138,516
50	25	352,634	408,871	167,265
70	40	423,465	459,331	206,259
130	60	394,224	588,975	214,549
150	70	448,560	671,751	242,264
170	100	482,145	686,054	271,119
220	120	510,121	835,806	303,642
250	140	537,708	905,703	326,019
250	120	531,968	943,496	327,227
250	105	521,099	911,721	299,901

TABLE B12 Moduli and Modular Ratio for Coarse Graded Aggregate #2 at Optimum Moisture Content

Stress (kPa)		Moduli (kPa)		
Axial	Radial	Horizontal	Vertical	Shear
40	25	223,072	254,365	88,022
50	25	218,621	278,099	97,270
70	40	330,424	330,610	161,078
130	60	295,684	542,925	170,012
150	70	340,189	623,603	199,362
170	100	425,433	584,101	236,137
220	120	438,945	705,210	253,037
250	140	491,027	805,713	288,959
250	120	451,752	800,105	270,550
250	105	408,824	816,299	250,858

TABLE B13 Moduli and Modular Ratio for Well Graded Aggregate #3 at Wet of Optimum Moisture Content

Stress (kPa)		Moduli (kPa)		
Axial	Radial	Horizontal	Vertical	Shear
40	25	79,930	67,636	25,068
50	25	59,166	86,534	29,256
70	40	99,911	118,295	47,965
130	60	133,373	207,297	69,450
150	70	188,481	230,589	88,946
170	100	283,175	258,989	120,397
220	120	281,178	348,956	136,021
250	140	335,500	418,703	164,949
250	120	292,470	412,850	151,629
250	105	261,471	401,830	139,397

TABLE B14 Moduli and Modular Ratio for Well Graded Aggregate #3 at Optimum Moisture Content

Stress (kPa)		Moduli (kPa)		
Axial	Radial	Horizontal	Vertical	Shear
40	25	72,004	72,163	23,277
50	25	76,602	97,388	34,401
70	40	147,898	116,257	60,256
130	60	149,159	202,450	72,782
150	70	187,808	241,747	90,343
170	100	251,092	250,910	114,478
220	120	279,958	314,831	131,328
250	140	324,625	364,749	154,308
250	120	292,022	367,085	145,333
250	105	262,663	365,266	136,143

TABLE B15 Moduli and Modular Ratio for Well Graded Aggregate #3 at Dry of Optimum Moisture Content

Stress (kPa)		Moduli (kPa)		
Axial	Radial	Horizontal	Vertical	Shear
40	25	141,175	129,731	51,786
50	25	114,538	153,597	55,295
70	40	190,842	177,519	88,245
130	60	180,728	284,776	96,983
150	70	213,580	329,738	114,333
170	100	265,627	330,947	139,024
220	120	281,481	400,274	150,829
250	140	314,486	459,546	173,480
250	120	282,624	464,927	163,084
250	105	253,698	470,556	153,708

TABLE B16 Moduli and Modular Ratio for Fine Graded Aggregate #3 at Wet of Optimum Moisture Content

Stress (kPa)		Moduli (kPa)		
Axial	Radial	Horizontal	Vertical	Shear
40	25	34,712	50,620	11,576
50	25	40,411	70,718	19,545
70	40	111,306	118,519	54,720
130	60	129,734	222,900	70,098
150	70	165,085	269,279	89,117
170	100	229,420	260,981	113,852
220	120	244,426	325,121	127,785
250	140	293,365	367,103	147,629
250	120	270,070	381,239	142,829
250	105	260,563	388,402	139,075

TABLE B17 Moduli and Modular Ratio for Fine Graded Aggregate #3 at Optimum Moisture Content

Stress (kPa)		Moduli (kPa)		
Axial	Radial	Horizontal	Vertical	Shear
40	25	34,767	80,000	12,322
50	25	38,964	90,000	20,672
70	40	96,492	110,399	44,644
130	60	128,463	223,346	70,217
150	70	159,825	273,500	88,398
170	100	239,509	281,727	117,097
220	120	256,899	352,002	133,794
250	140	297,129	403,637	154,650
250	120	267,173	401,632	145,547
250	105	250,421	403,776	137,634

TABLE B18 Moduli and Modular Ratio for Fine Graded Aggregate #3 at Dry of Optimum Moisture Content

Stress (kPa)		Moduli (kPa)		
Axial	Radial	Horizontal	Vertical	Shear
40	25	200,976	165,931	70,046
50	25	140,000	180,000	85,000
70	40	245,011	196,649	100,335
130	60	241,596	292,941	114,294
150	70	261,911	341,473	131,360
170	100	333,613	332,059	153,077
220	120	351,070	398,562	167,108
250	140	381,290	448,526	185,183
250	120	352,771	442,948	175,396
250	105	319,478	442,309	167,469

TABLE B19 Moduli and Modular Ratio for Coarse Graded Aggregate #3 at Optimum Moisture Content

Stress (kPa)		Moduli (kPa)		
Axial	Radial	Horizontal	Vertical	Shear
40	25	95,891	86,506	32,157
50	25	83,830	118,406	38,195
70	40	145,100	151,464	71,248
130	60	154,620	252,288	84,608
150	70	171,441	303,877	101,168
170	100	235,495	283,882	120,434
220	120	259,735	340,449	132,787
250	140	294,826	387,506	151,071
250	120	254,917	397,531	144,716
250	105	232,150	405,953	137,510

TABLE B20 Moduli and Modular Ratio for Coarse Graded Aggregate #3 at Dry of Optimum Moisture Content

Stress (kPa)		Moduli (kPa)		
Axial	Radial	Horizontal	Vertical	Shear
40	25	109,782	95,412	35,128
50	25	104,297	127,009	46,467
70	40	145,100	151,464	71,248
130	60	168,133	249,374	87,364
150	70	195,268	296,061	103,585
170	100	258,835	298,699	129,238
220	120	270,249	383,091	143,216
250	140	295,236	439,368	166,029
250	120	268,361	439,660	153,615
250	105	239,565	435,067	143,422

TABLE B21 Moduli and Modular Ratio for Well Graded Aggregate #4 at Optimum Moisture Content

Stress (kPa)		Moduli (kPa)		
Axial	Radial	Horizontal	Vertical	Shear
40	25	177,395	156,285	60,729
50	25	164,008	164,921	68,997
70	40	184,753	202,573	89,820
130	60	201,926	309,311	111,441
150	70	242,318	330,211	126,582
170	100	308,900	346,563	154,799
220	120	332,231	418,092	172,150
250	140	376,984	471,527	192,967
250	120	330,514	482,510	182,482
250	105	312,833	470,648	174,284

TABLE B22 Moduli and Modular Ratio for Fine Graded Aggregate #4 at Optimum Moisture Content

Stress (kPa)		Moduli (kPa)		
Axial	Radial	Horizontal	Vertical	Shear
40	25	102,979	109,259	42,906
50	25	106,012	123,968	48,956
70	40	125,737	149,043	64,157
130	60	143,049	228,954	80,000
150	70	178,112	247,680	93,750
170	100	219,807	252,980	110,865
220	120	239,214	309,756	124,447
250	140	269,739	344,032	138,462
250	120	249,334	339,398	131,887
250	105	231,185	337,921	126,404

TABLE B23 Moduli and Modular Ratio for Coarse Graded Aggregate #4 at Optimum Moisture Content

Stress (kPa)		Moduli (kPa)		
Axial	Radial	Horizontal	Vertical	Shear
40	25	112,161	121,516	44,248
50	25	107,819	126,635	48,170
70	40	159,644	147,047	70,822
130	60	156,957	235,841	83,612
150	70	180,767	270,734	97,025
170	100	250,560	262,953	120,289
220	120	259,738	321,366	130,435
250	140	302,367	363,801	149,601
250	120	269,535	363,298	140,274
250	105	242,566	361,731	132,120

TABLE B24 Moduli and Modular Ratio for Well Graded Aggregate #5 at Wet of Optimum Moisture Content

Stress (kPa)		Moduli (kPa)		
Axial	Radial	Horizontal	Vertical	Shear
40	25	62,591	61,286	14,497
50	25	59,616	82,941	24,592
70	40	123,900	130,826	58,347
130	60	173,609	309,352	96,682
150	70	232,333	373,982	123,390
170	100	290,580	341,767	150,920
220	120	303,851	446,046	166,450
250	140	385,436	519,194	200,477
250	120	328,348	544,917	186,653
250	105	302,640	581,695	186,142

TABLE B25 Moduli and Modular Ratio for Well Graded Aggregate #5 at Optimum Moisture Content

Stress (kPa)		Moduli (kPa)		
Axial	Radial	Horizontal	Vertical	Shear
40	25	102,238	137,337	42,019
50	25	113,490	170,024	55,900
70	40	194,748	210,022	96,114
130	60	232,679	322,658	115,342
150	70	276,613	379,068	137,423
170	100	353,800	388,283	170,503
220	120	385,535	487,066	192,228
250	140	439,928	562,986	228,051
250	120	386,303	583,156	212,984
250	105	370,686	551,669	198,941

TABLE B26 Moduli and Modular Ratio for Well Graded Aggregate #5 at Dry of Optimum Moisture Content

Stress (kPa)		Moduli (kPa)		
Axial	Radial	Horizontal	Vertical	Shear
40	25	170557	155960	61783
50	25	177920	190833	72106
70	40	263920	214695	103509
130	60	296543	343190	134044
150	70	346548	405407	156691
170	100	401443	398228	187518
220	120	419694	510167	205027
250	140	461885	565139	230194
250	120	412175	589166	218422
250	105	408561	558423	210873

TABLE B27 Moduli and Modular Ratio for Fine Graded Aggregate #5 at Wet of Optimum Moisture Content

Stress (kPa)		Moduli (kPa)		
Axial	Radial	Horizontal	Vertical	Shear
40	25	22,233	56,899	8,058
50	25	10,370	40,398	4,130
70	40	54,278	124,471	34,426
130	60	60,768	122,814	32,472
150	70	99,770	176,674	52,862
170	100	161,178	191,865	79,595
220	120	193,736	284,915	101,212
250	140	235,469	359,070	128,433
250	120	212,567	371,269	122,663
250	105	194,635	367,769	115,251

TABLE B28 Moduli and Modular Ratio for Fine Graded Aggregate #5 at Optimum Moisture Content

Stress (kPa)		Moduli (kPa)		
Axial	Radial	Horizontal	Vertical	Shear
40	25	193,880	172,553	64,342
50	25	184,047	195,622	77,671
70	40	268,101	226,859	106,858
130	60	284,807	356,092	134,911
150	70	331,245	397,454	154,704
170	100	390,613	416,814	186,448
220	120	380,373	535,752	203,416
250	140	428,003	579,916	225,448
250	120	395,377	589,837	217,214
250	105	357,925	592,398	203,330

TABLE B29 Moduli and Modular Ratio for Fine Graded Aggregate #5 at Dry of Optimum Moisture Content

Stress (kPa)		Moduli (kPa)		
Axial	Radial	Horizontal	Vertical	Shear
40	25	221,362	196,290	75,778
50	25	229,476	210,230	86,351
70	40	301,483	240,617	120,840
130	60	335,873	346,863	141,637
150	70	382,117	403,836	168,099
170	100	443,837	418,548	200,545
220	120	443,262	501,258	212,720
250	140	487,462	564,494	236,357
250	120	441,821	578,370	225,870
250	105	422,930	573,272	222,043

TABLE B30 Moduli and Modular Ratio for Coarse Graded Aggregate #5 at Optimum Moisture Content

Stress (kPa)		Moduli (kPa)		
Axial	Radial	Horizontal	Vertical	Shear
40	25	96,699	110,790	36,365
50	25	104,363	130,121	44,849
70	40	154,928	163,806	70,546
130	60	202,927	275,840	99,092
150	70	244,008	322,601	118,527
170	100	299,347	331,082	143,470
220	120	319,726	398,334	163,906
250	140	355,199	471,004	186,681
250	120	325,482	457,935	172,577
250	105	300,550	459,386	166,016

TABLE B31 Moduli and Modular Ratio for Well Graded Aggregate #6 at Wet of Optimum Moisture Content

Stress (kPa)		Moduli (kPa)		
Axial	Radial	Horizontal	Vertical	Shear
40	25	293,540	218,365	83,536
50	25	286,074	243,676	104,416
70	40	394,690	287,649	160,712
130	60	392,548	446,509	183,393
150	70	452,796	529,701	217,454
170	100	545,021	501,278	248,892
220	120	606,872	608,294	275,722
250	140	657,543	701,804	314,600
250	120	632,056	704,315	303,232
250	105	589,973	715,999	292,255

TABLE B32 Moduli and Modular Ratio for Well Graded Aggregate #6 at Optimum Moisture Content

Stress (kPa)		Moduli (kPa)		
Axial	Radial	Horizontal	Vertical	Shear
40	25	218,869	184,772	73,532
50	25	232,813	230,240	95,490
70	40	332,604	256,347	137,025
130	60	356,815	428,142	166,565
150	70	394,969	524,409	198,102
170	100	493,625	504,437	235,586
220	120	528,566	633,257	265,001
250	140	601,123	733,858	306,837
250	120	543,003	744,402	288,789
250	105	497,845	752,483	274,385

TABLE B33 Moduli and Modular Ratio for Well Graded Aggregate #6 at Dry of Optimum Moisture Content

Stress (kPa)		Moduli (kPa)		
Axial	Radial	Horizontal	Vertical	Shear
40	25	40,264	101,248	15,262
50	25	78,946	111,825	38,847
70	40	157,029	189,639	84,146
130	60	229,200	345,169	118,059
150	70	316,579	416,431	155,740
170	100	416,311	424,975	197,804
220	120	465,067	568,859	228,500
250	140	542,036	666,319	272,201
250	120	503,466	669,004	257,839
250	105	452,272	676,309	239,284

TABLE B34 Moduli and Modular Ratio for Fine Graded Aggregate #6 at Optimum Moisture Content

Stress (kPa)		Moduli (kPa)		
Axial	Radial	Horizontal	Vertical	Shear
40	25	36,642	73,194	15,213
50	25	33,028	66,159	18,797
70	40	93,750	115,393	51,160
130	60	115,678	271,777	70,093
150	70	151,177	346,707	94,757
170	100	210,710	308,710	122,750
220	120	236,876	412,563	136,281
250	140	297,752	495,293	170,713
250	120	265,437	516,316	159,574
250	105	235,900	535,083	149,701

TABLE B35 Moduli and Modular Ratio for Coarse Graded Aggregate #6 at Dry of Optimum Moisture Content

Stress (kPa)		Moduli (kPa)		
Axial	Radial	Horizontal	Vertical	Shear
40	25	210,854	186,547	70,688
50	25	200,875	208,104	86,505
70	40	231,654	284,320	121,753
130	60	297,593	411,884	153,531
150	70	347,628	495,355	183,824
170	100	446,311	474,297	222,552
220	120	465,139	584,056	241,676
250	140	535,886	667,007	277,778
250	120	477,699	681,342	260,417
250	105	436,848	683,619	248,071

VITA

The author, Sung-Hee Kim, was born on February 6, 1974 in Seoul, Korea. He entered Inha University in 1992 and obtained his Bachelor of Science degree in civil engineering in February 1999.

In August 1999, he started his graduate studies at Georgia Institute of Technology, Atlanta, GA where he received his Master of Science degree in civil engineering in 2000. During his master's program at Georgia Tech., he worked as a graduate research assistant in the School of Civil and Environmental Engineering supervised by Dr. James S. Lai in the geotechnical engineering division.

In 2000, Sung-Hee Kim started his Ph.D. studies at Texas A&M University at College Station, TX. He worked as a graduate research assistant in the Texas Transportation Institute and was involved with modeling of nonlinear cross-anisotropic behavior of granular materials under the guidance of Dr. Dallas N. Little.

Department of Civil Engineering
Texas A&M University
CE/TTI Building 601A
College Station, TX 77843